Monolithically Integrated Gain Shifted Mach-Zehnder Interferometer for All-Optical Demultiplexing

vorgelegt von
Diplom-Ingenieur
Tolga Tekin

von der Fakultät IV für Elektrotechnik und Informatik
der Technischen Universität Berlin
zur Erlangung des akademischen Grades

Doktor der Ingenieurwissenschaften

genehmigte Dissertation

Promotionsausschuss:

Vorsitzender:	Prof. Dr.-Ing. H. Henke
Berichter:	Prof. Dr.-Ing. K. Petermann
Berichter:	Prof. Dr. rer. nat H. G. Weber

Tag der wissenschaftlichen Aussprache: 04.06.2004

Berlin 2004
D 83

To my daughter, Ada

Abstract

Optical time division multiplexing (OTDM) is one of the fundamental techniques to increase the transmission capacity on a fiber. At the receiver side the base rate data signals must be extracted from the OTDM data stream by using an optical switch with a demultiplexing function.
Different approaches have been proposed and used for optical switching. The possible approaches can be categorized as follows: electro-optical demultiplexer and all-optical demultiplexer. The electro-optical demultiplexers rely on the electrical control of the switching function. The general principle of the all-optical switches relies on the control of light by light. Some of the basic requirements for such a switch can be defined as follows: The switching time should be much less than the bit period of the OTDM data signal; it has to have high switching contrast of more than 10 dB; it should be stable to provide a good system performance.
This thesis presents an all-optical demultiplexer based on semiconductor optical amplifiers (SOA) monolithically integrated in a 'gain shifted' (GS) Mach-Zehnder interferometer (MZI). The switch operates all-optically and can handle data rates up to160 Gbit/s. It has a high contrast ratio and the monolithic integration provides the required stability.
The GS switching scheme investigated here intends to find a compromise between the advantages and disadvantages of the existing 'conventional' and 'gain transparent' (GT) switching schemes. Moreover, as a switch based on the GT-switching scheme was never realized as monolithically integrated device, this work presents the first monolithically integrated interferometric switch in a non-conventional switching scheme.
The GS-switching scheme provides reduced amplified spontaneous emission noise, reduced pattern effects, better linearity and low insertion loss.
A polarization insensitive design of the monolithically integrated GS-MZI was developed, which enables process tolerant technological realization of devices with reduced internal losses, reduced internal reflections and improved fiber-chip coupling.
Static and dynamic switching performances of the GS-MZI have been analyzed and compared with existing solutions.
Error-free all-optical demultiplexing from 160 Gbit/s to 10 Gbit/s has been successfully performed with the monolithically integrated MZI comprising GS-SOAs for all OTDM channels.

Zusammenfassung

Das optische Zeitmultiplex-Verfahren (optical time division multiplexing, OTDM) ist eines der gebräuchlichsten Verfahren, um die Datenübertragungskapazität einzelner Glasfaser zu erhöhen. Auf der Empfängerseite sind die Signale der Basisdatenrate durch einen optischen Schalter mit einer Demultiplexer Funktion wieder zurückzugewinnen.
Die verschiedene Möglichkeiten zur Realisierung schneller optischer Demultiplexer unterscheiden sich im wesentlichen durch ihre Ansteuerung: Elektro-optische und rein-optische Demultiplexer. Der rein-optische Schalter basiert auf dem Prinzip Licht durch Licht zu steuern. Die wichtigsten Anforderungen an schnelle Schalter sind: Die Öffnungszeiten der Schalter müssen kürzer als die Bitperiode des OTDM Datensignals sein; der Schalter muss ein hohes Unterdrückungsverhältnis von grösser als 10 dB besitzen und stabil sein um ein gutes Systemperformance zu gewährleisten.
Diese Arbeit präsentiert einen rein-optischen Demultiplexer basierend auf Halbleiterlaserverstärkern (semiconductor optical amplifier, SOA) in einem Mach-Zehnder Interferometer (MZI) als monolithisch integriertes Bauelement, das sogenannte monolithisch integrierte ‘gewinn-verschobene’ (gain shifted, GS) MZI. Das Operationsprinzip des Schalters ist rein-optisch und kann bei einer Übertragungsrate bis zu 160 Gbit/s eingesetzt werden. Der Schalter hat ein hohes Unterdrückungsverhältnis und die monolithische Integration ermöglicht die benötigte Stabilität.
Mit dem hier untersuchten GS Schaltschema wurde ein Kompromiss zwischen den Vor- und Nachteilen der konventionellen und ‘gewinn-transparenten’ (gain transparent, GT) Schaltschemen angestrebt. Ausserdem präsentiert diese Arbeit den ersten monolithisch integrierten Schalter in einem unkonventionellen Schaltschema, da der GT-Schalter noch nicht als ein monolithisch integriertes Bauelement realisiert wurde.
Das GS Schaltschema reduziert das Rauschen, die Patterneffekte und die Einfügedämpfung und ermöglicht eine breite Linearität.
Ein polarisationsunempfindliches Design für monolithisch integrierte MZI wurde entwickelt. Hierdurch wurde eine prozesstolerante Herstellung von Bauelementen mit reduzierter Einfügedämpfung, reduzierten internen Reflektionen und einer verbesserten Faser-Chip Kopplung realisiert.
Statisches und dynamisches Schaltverhalten des monolithisch integrierten GS-MZIs wurden analysiert.
Fehlerfreies rein-optisches Schalten von 160 Gbit/s auf 10 Gbit/s konnte mit dem neuen monolithisch integrierten auf GS-SOA basierenden MZI für alle OTDM-Kanäle erfolgreich gezeigt werden.

Contents

1 Introduction

The vision of the information age is that information can be located anywhere but is accessible from everywhere as if it were located locally. To realize this, networks of enormous capacity will be required to provide the infrastructure. Optical networking is one key technology to fulfill the demands for bandwidth and to deploy new services.

1.1 Optical Networks

In the first generation of optical networks (e.g. SONET and SDH [1]), the optical fiber is used purely as a transmission medium, serving as a replacement for copper cable, and all switching and processing of the bits are handled by electronics. They are widely deployed today in all kinds of telecommunication networks, except access networks.
Optical fiber transmission has played a key role in increasing the bandwidth of telecommunications networks. To increase the transmission capacity on a fiber there are fundamentally two techniques [1]:

- Wavelength division multiplexing (WDM)
- Optical time division multiplexing (OTDM)

The principle of both techniques are illustrated in the Figure 1.1.

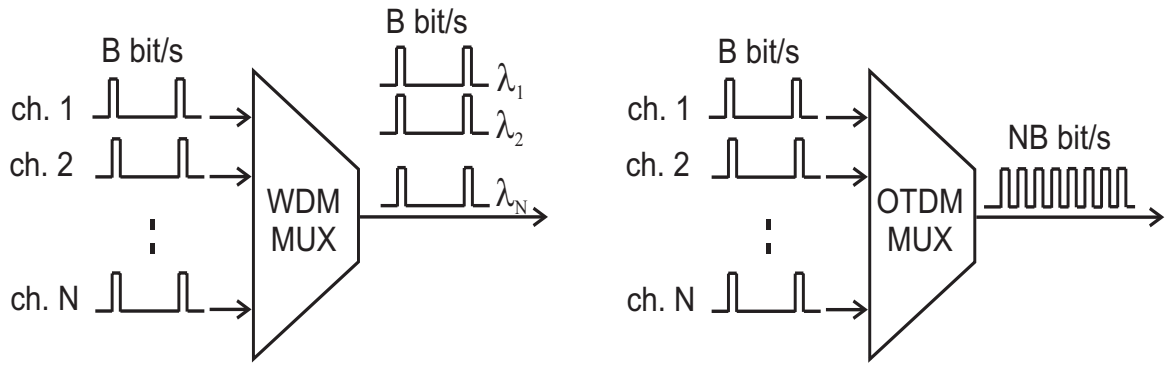

Figure 1.1 Both optical multiplexing techniques to increase the transmission capacity on an optical fiber; WDM and OTDM after [1].

The idea of WDM is to transmit data simultaneously at multiple carrier wavelengths over a fiber and by this to increase the capacity of a fiber. This technique is essentially the same as in the radio systems used frequency division multiplexing technique.
Many (N) lower speed data streams (B bit/s) are multiplexed into a higher speed stream (NB bit/s) at the transmission bit rate by means of time division multiplexing. This requires higher speed electronics. Beyond the data rates of 40 Gbit/s, the optical time division multiplexing is well suited, since the commercial available electronic systems are limited. The OTDM technique allows increasing the bit rate.
The optical networks are capable of providing more functions than just point-to-point transmission. In the second generation of networks some of the switching and routing functions that were performed by electronics are incorporated into the optical part of the network.

1.2 Optical Demultiplexing

The general layout of an optical time division multiplexing system is illustrated in the Figure 1.2.

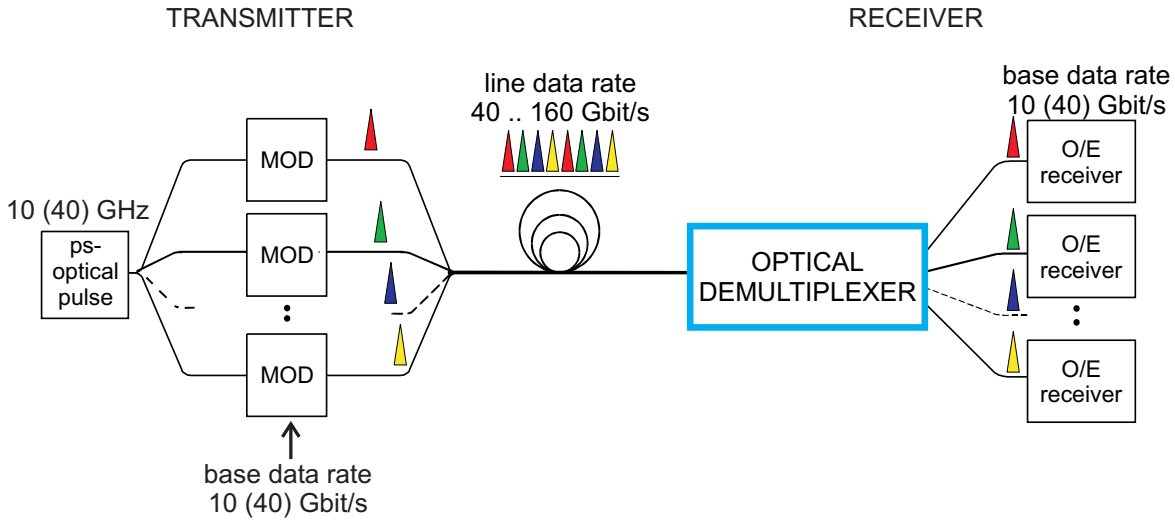

Figure 1.2 The general layout of an OTDM system with an optical demultiplexer at the receiver node.

At the transmitter side of the system picosecond optical pulses (10 - 40 GHz) are modulated in several optical branches at the base data rate (10 - 40 Gbit/s) and multiplexed in the time domain into a TDM data signal-stream (40 - 160 Gbit/s). At the receiver side the base rate data signals must be extracted

from the TDM-data stream. An optical switch with a demultiplexing function is essential to obtain the extraction of the base rate data signals.
Different approaches have been proposed and used for optical switching as will be discussed in Chapter 2. The possible approaches can be categorized as follows:

- Electro-optical demultiplexer
- All-optical demultiplexer

The electro-optical demultiplexers rely on the electrical control of the switching function. The control input signal is an electrical signal. The electro-optical demultiplexers are partly commercialized. The applicability of these switches with recent technologies for ultrahigh-speed optical signal processing in future optical networks is restricted to less than 100 Gbit/s [1].
The general principle of the all-optical switches relies on the control of light by light. The all-optical demultiplexer has been one of the most investigated components in OTDM communication networks [2]. Starting from the hybrid interferometric structure based on the nonlinear Kerr effect in fibers up to the semiconductor optical amplifier based monolithically integrated nonlinear interferometer structures using the nonlinearity in semiconductor material, various approaches have been proposed and used for all-optical demultiplexing [3].

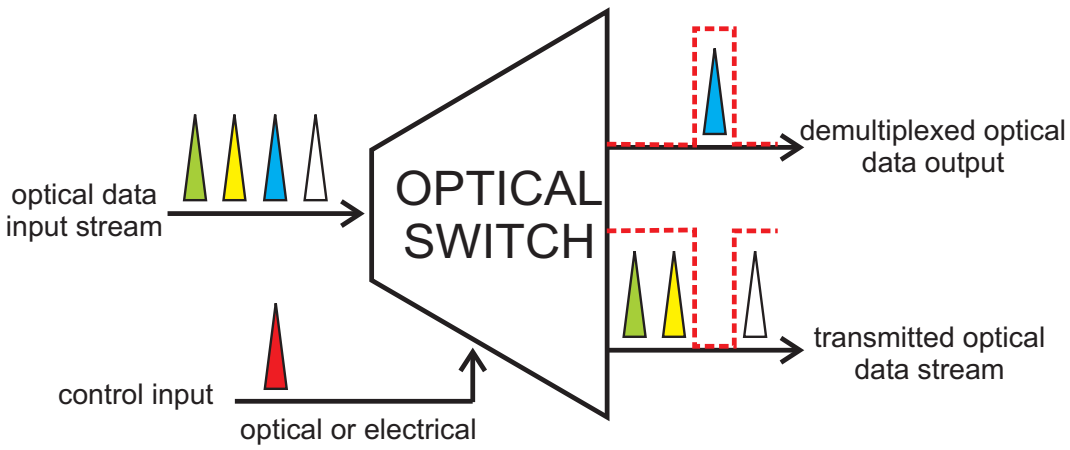

Figure 1.3 Optical switch as a black box with its inputs and outputs.

1.3 Scope of the Thesis

As emphasized, the optical demultiplexer is one of the key components of the OTDM system. Some of the basic requirements for such a switch can be defined as follows:

- The switching window should be much less than the bit period of the TDM-data signal, i.e. about 6 ps for a TDM-data rate of 160 Gbit/s
- It has to have high switching contrast of more than 10 dB
- It should be stable to provide a good system performance

This thesis presents an all-optical demultiplexer based on semiconductor optical amplifiers (SOA) in a Mach-Zehnder interferometer as monolithically integrated device. The device is called monolithically integrated 'gain shifted' (or 'band gap shifted') Mach-Zehnder interferometer. The switch operates all-optically and can handle data rates up to 160 Gbit/s. It has a high contrast ratio. And the monolithic integration provides the required stability.

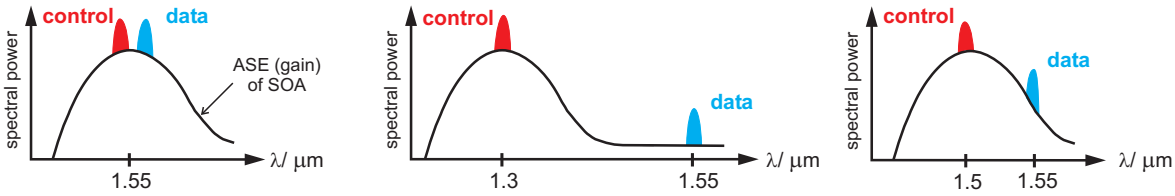

a) Conventional b) GT c) GS

Figure 1.4 The all-optical switching schemes, regarding the material and operating wavelength.

The expression 'gain shifted' (or 'band gap shifted') (GS) Mach-Zehnder interferometer is explained in Figure 1.4. This figure shows three times an ASE (or gain) spectrum of an SOA. In all figures the wavelength of the data signal is the same. The three figures differ by the choice of the wavelength of the maximum of the ASE or gain spectrum, which is the same wavelength as the wavelength of the control signal. In the conventional mode of operation of an SOA-based interferometric switch (a) data signal and control signal have a wavelength near the maximum of the gain spectrum of the SOA. This arrangement has the disadvantages that the data signal affects the switching operation by itself. Therefore the 'gain transparent' (GT) operation (b) was introduced, where the data signal does not affect the gain. This arrangement has the disadvantages that the transmittance of the switch is rather small. The 'gain shifted' (GS) switching scheme (c) investigated here intends to find a

compromise between the advantages and disadvantages of the 'conventional' and 'GT' switching scheme. Moreover, as a switch based on the GT switching scheme was never realized as monolithically integrated device, this work presents the first monolithically integrated interferometric switch in a non-conventional switching scheme.

1.4 Outline of the Thesis

The chapters of this thesis are based on the previous publications and studies (section 13) by the author. The thesis is divided into seven chapters.

Chapter 2 reviews briefly the existing optical switches, especially optical demultiplexer. The merits and shortcomings of significant optical demultiplexing components and their principle of operation are summarized.

Chapter 3 discusses the all-optical switching architecture. Furthermore, the new 'gain shifted' switching scheme, which has been developed, will be introduced and compared with other existing solutions.

Chapter 4 analyzes different types of basic optical components of the monolithically integrated Mach-Zehnder interferometer. Furthermore, the polarization insensitive Mach-Zehnder interferometer design is discussed, which leads to a process tolerant realization of Mach-Zehnder devices with improved specifications such as low insertion losses, reduced internal reflections and optimized fiber-chip coupling.

Chapter 5 describes the characterization of monolithically integrated Mach-Zehnder interferometer in view of the ultrafast demultiplexing operation. Furthermore, switching dynamics of 'gain shifted' Mach-Zehnder interferometer and dynamic response of its semiconductor optical amplifier are evaluated.

Chapter 6 summarizes the results of all-optical demultiplexing system experiments by using the monolithically integrated Mach-Zehnder interferometer. The first error-free 160 Gbit/s all-optical demultiplexing experiments using a monolithically integrated 'gain shifted' MZI are presented.

Finally, Chapter 7 presents conclusions and discusses outlook for further applications.

1.5 Major Results

In the author's opinion, the major results of this research work are as follows:

- A new switching scheme for monolithically integrated Mach-Zehnder interferometer have been developed, the so-called 'gain shifted' switching scheme. The new switching scheme is a compromise between the 'conventional' and 'GT' switching scheme, which provides reduced amplified spontaneous emission noise, reduced pattern effects, linearity and low insertion loss.

- A polarization insensitive design of the monolithically integrated 'gain shifted' Mach-Zehnder interferometer was developed, which enables process tolerant technological realization of devices with reduced internal losses, reduced internal reflections and improved fiber-chip coupling.

- Static and dynamic switching performances of the monolithically integrated 'gain shifted' Mach-Zehnder interferometer have been analyzed.

- Error-free all-optical demultiplexing from 160 Gbit/s to 10 Gbit/s has been successfully performed with the monolithically integrated Mach-Zehnder interferometer comprising 'gain shifted' semiconductor optical amplifiers.

2 Brief Review of Existing Solutions for Optical Demultiplexing

In this chapter, a brief review of the existing solutions for optical time division demultiplexing will be presented according to the categorization, which was introduced in the section 1.2 (Figure 2.1).

OPTICAL DEMULTIPLEXER											
Electro-Optical		**ALL-OPTICAL**									
		Hybrid							**INTEGRATED**		
				Nonlinear Interferometer						**MZI**	
				SI							
EAM	MZI	FWM	MLL	NOLM	NALM	SLALOM /TOAD	UNI	MZI	SI	Asymmetric MZI	**Symmetric MZI**
Section 2.1	Section 2.1	Section 2.2	Section 2.3	Section 9.1	Section 9.1	Section 2.4	Section 2.5	Section 2.6	Section 2.4	Section 2.7	Section 2.7

Figure 2.1 The optical demultiplexer categories.

The basic approaches for optical demultiplexers are: electro-absorption modulator (EAM), electro-optical MZI, four-wave mixing (FWM), mode-locked laser (MLL), hybrid nonlinear interferometers (NLI) such as nonlinear optical loop mirror (NOLM), nonlinear amplifying loop mirror (NALM), semiconductor laser amplifier in a loop mirror (SLALOM), ultrafast nonlinear interferometer (UNI), Mach-Zehnder interferometer (MZI), integrated nonlinear interferometer such as Sagnac interferometer (SI), asymmetric and symmetric Mach-Zehnder interferometer.
During recent years, nonlinear interferometer based switches have become promising components for optical communication systems. These are namely, Sagnac interferometer, ultrafast nonlinear interferometer and Mach-Zehnder interferometer.

2.1 Electro-Optical Demultiplexer

Electro-optical demultiplexers are based on either amplitude modulation (AM) or phase modulation (PM) through the quantum confined Stark effect (QCSE) in semiconductors [4].
The electro-absorption modulators (EAM) are high-speed commercialized devices finding applications in a number of areas besides demultiplexing.
The absorption spectrum in multiple quantum well (MQW) devices can be changed by applying a negative bias and modulation voltage. The transmission through the device is modulated according to the absorption spectrum. Due to the nonlinearity of the QCSE a sinusoidal modulation can result in a switching window, which is narrow enough for demultiplexing. The state of the art applications of EAM as an optical demultiplexer can be found in [5].
By replacing the MQW active material in a Mach-Zehnder interferometer the refractive index can be changed accompanied by a change in the absorption spectrum, details can be found in [4].

2.2 Four Wave Mixing

The four wave mixing (FWM) method relies on the third-order nonlinear susceptibility of the material [6] and it can be used for all-optical demultiplexing. A probe pulse stream is added synchronously with, and closely spaced in wavelength to the multiplexed data, the waves interact in a dispersion shifted single mode fiber (DSF) by FWM due to the third-order nonlinear susceptibility when probe and signal pulses overlap [7]. One of the two generated mixing terms is filtered out and used to extract the data.

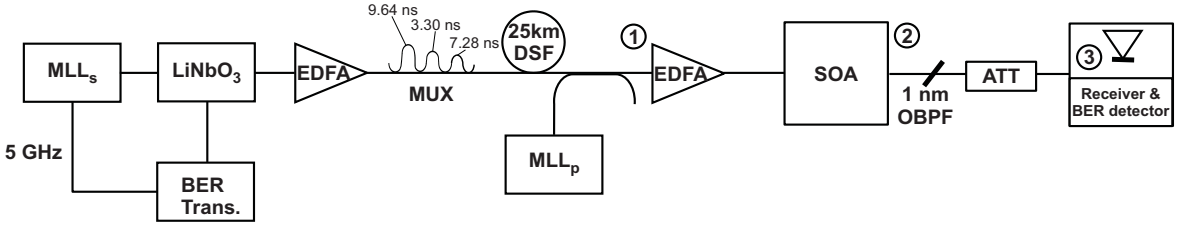

Figure 2.2 Experimental setup of FWM with SOA after [8].

To avoid the walk-off problem in the fibers, due to the required long length of fiber (~10 km), the nonlinearity of a semiconductor laser amplifier (SOA) is used in a FWM based all-optical demultiplexer [8]. Here the first error-free demultiplexing at 20 Gbit/s using FWM was demonstrated (Figure 2.2). Further, by using traveling wave laser diode amplifiers (TW-LDA) all-optical

demultiplexing based on FWM was shown error-free at 100 Gbit/s [9] and in a 200 km polarization insensitive optical transmission experiment respectively [10]. Polarization independent all-optical demultiplexing has been demonstrated up to 200 Gbit/s based on FWM in semiconductor optical amplifiers [11]. The main disadvantage of a FWM based demultiplexer is the low signal-to-noise ratio of this process [6]. Regarding the last publications, the polarization sensitivity problem of the FWM scheme is solved by using two orthogonal polarized pump signals [12]. The main advantage of a FWM based demultiplexer is its high speed (> 100 Gbit/s) potential.

2.3 Mode-Locked Laser Diode

The mode-locked laser diode (MLLD) can also be used for all-optical demultiplexing [13]. This was demonstrated by using a MLLD for 40 to 10 Gbit/s demultiplexing. The device under test had both sides anti-reflection (AR) coated and comprises two sections: a 200 µm long saturable absorber (SA) section and a 2000 µm long gain section [14]. To switch the MLLD-gate a second MLLD was used as clock recovery. The MLLD-clock extracted the 10 GHz sub-harmonic. This signal was used to control the MLLD-gate (Figure 2.3).

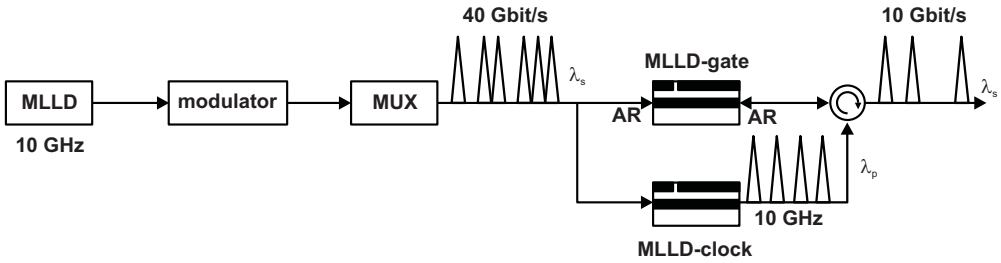

Figure 2.3 All-optical demultiplexer using MLLD after [14].

The optical clock pulses are amplified in the gain section of the device and readily induce absorption saturation in the SA section to open the SA optical gate. The data pulse energy has to be set below the saturation energy of the SA. After passage of each clock pulse, the SA recovers to a high-absorption state with its absorption recovery time constant. Therefore, only an optical data pulse, which adequately overlap with an optical clock pulse pass the SA, while the rest of the optical data pulses, are absorbed. The extinction ratio can be improved with the length of the SA section. The length of the SA, the ratio of the gain and SA lengths, the central wavelength of the optical gain, the AR-coating and the optical confinement factor are playing important roles in the behavior of the MLLD.

2.4 Semiconductor Laser Amplifier in a Loop Mirror

Nonlinear interferometric (NLI) structures for all-optical demultiplexing were primarily assembled as a nonlinear Sagnac interferometer (SI) [15] by using an optical fiber loop (section 9.1) and a discrete semiconductor optical amplifier component incorporated within the fiber loop.
The 'semiconductor laser amplifier in a loop mirror' (SLALOM) and the 'terahertz optical asymmetric demultiplexer' (TOAD), which were reported by Eiselt [16] and by Sokoloff et al. [17], incorporate an off-center placed SOA in a loop mirror.
In the SLALOM due to the asymmetrically positioned SOA (Figure 2.4), the clockwise propagating pulse that arrives at the SOA earlier, is amplified and saturates the SOA. The counter-clockwise propagating pulse experiences the saturated gains as well as an additional phase shift, which is related to the gain saturation by the linewidth enhancement factor α [16].

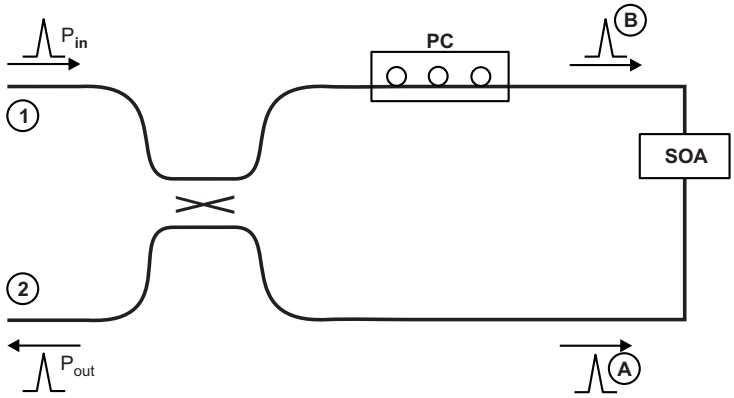

Figure 2.4 Principle of operation of SLALOM after [16].

In this geometry the high-energy control pulses are injected from one of the two input ports. Thus, the two parts of the control pulse travel both clockwise and counter-clockwise through the loop resulting in two SOA saturation events per control pulse [16]. By using a time delay between the control and data pulses, the desired data channel is transmitted (or demultiplexed) to the second port, whereas the other channels are reflected back to the input port. In principle, there is no need for control pulses traveling in both directions through the loop. In fact two saturation events per pulse reduce the usable phase shift and also distort the switching window in the SLALOM.
The TOAD allows the injection of control pulses directly into the loop and only one SOA saturation event per control pulse (Figure 2.5).

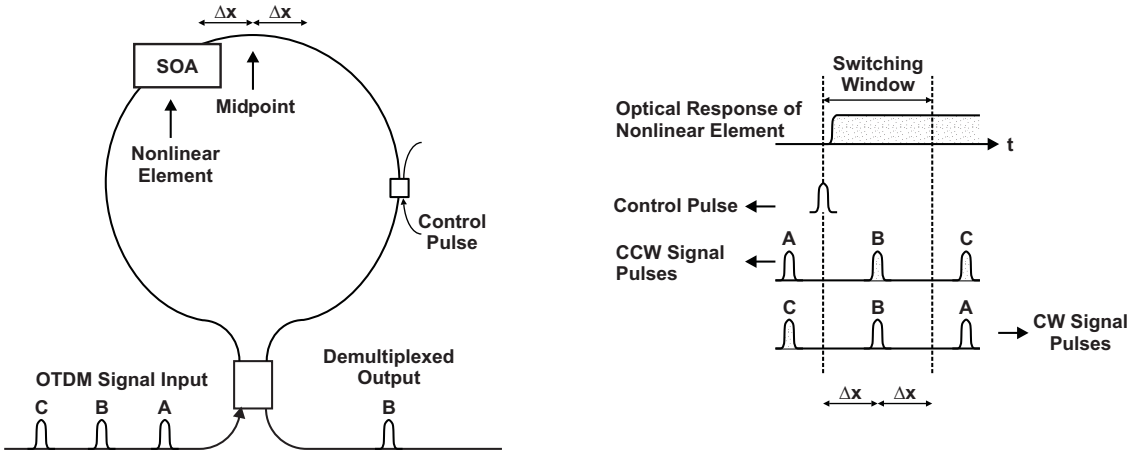

Figure 2.5 Illustration of operation of the TOAD after [17].

Demultiplexing of high-speed pulse trains (> 40 Gbit/s) down to a rate of about 1 Gbit/s was reported by Ellis and Spirit [18]. The operations of SLALOM and TOAD are analyzed by Eiselt [19] and Kane et al. [20], respectively. Further investigations are reported: demultiplexing at 250 Gbit/s [21], 160 to 10 Gbit/s demultiplexing [22], 8x80 to 8x10 Gbit/s demultiplexing using the 'gain transparent' (GT-SOA) switch [23].
Sagnac interferometers consisting of an off-center positioned SOA as a nonlinear element offer significant advantages over its fiber based counter parts. However, in such hybrid SOA/fiber devices it is usually necessary to employ the Sagnac configuration in combination with a polarization controller in order to handle the instability of path length and polarization due to thermal and/or acoustic fluctuations. They are small enough to be integrated within a chip.

Monolithically integrated nonlinear Sagnac interferometer

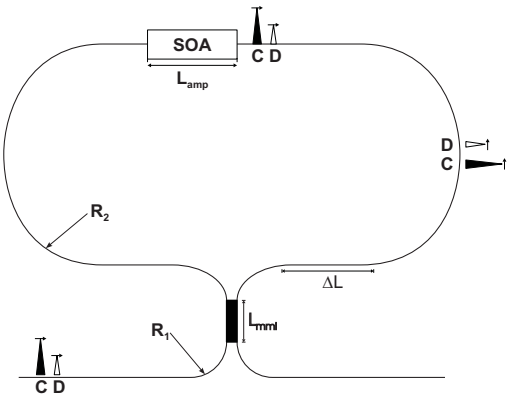

Figure 2.6 Schematic of monolithically integrated Sagnac interferometer for all-optical demultiplexing after [24]

The first monolithically integrated nonlinear Sagnac interferometer and its application as a 20 Gbit/s all-optical demultiplexer was reported by Jahn et al. (Figure 2.6) [24]. In the reported device, the amplifying section is 750 µm long and asymmetrically placed in the loop with ΔL=1.5 mm, such that the time delay between both counter-propagating pulses is about 30 ps.

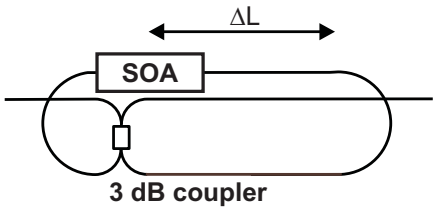

Figure 2.7 Illustration of 40% area saving in a monolithically integrated Sagnac interferometer after [24].

A 40 % saving of chip area is achieved by inverting the coupler and input/output waveguides so that they are inside the loop (Figure 2.7) [24].
The potential of the photonic integrated circuits (PICs) in high capacity OTDM systems have been demonstrated with these compact devices.

2.5 Ultrafast Nonlinear Interferometer

The ultrafast nonlinear interferometer (UNI) is another type of interferometric switch, which can be used for all-optical demultiplexing. The UNI is a balanced, single arm interferometer that does not require any external stabilization of the interferometer arms [25]. A schematic of the UNI gate is shown in Figure 2.8.

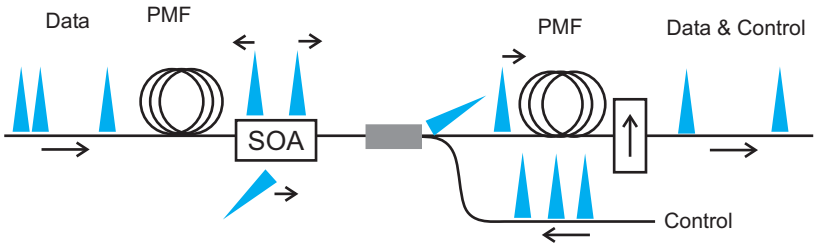

Figure 2.8 Schematic of the UNI gate after [26].

The signal pulse that is to be switched is split into two orthogonal polarization components with a time delay by passing it through highly birefringent fiber (polarization maintaining fiber, PMF). The two orthogonal pulses then pass through a SOA and are temporally recombined after passing through a second

birefringent fiber. The state of polarization of the signal pulse after recombining is determined by the relative phase difference between the split signal pulses. The phase changes induced from the time dependent refractive index changes in the presence of a control pulse (which could be co-propagating or counter-propagating) that is aligned temporally between the orthogonal pulses in the SOA lead to change of the relative phase difference and therefore to a different polarization state. The signal pulse then passes through a fiber polarizer that is adjusted such that the signal pulse is orthogonal to the polarizer in the absence of the control pulse and parallel to the polarizer when the control pulse is present. 100 Gbit/s bit wise switching has been demonstrated using the UNI gate. The UNI is suited for high-speed all-optical demultiplexing. However, it is polarization dependent. Recent system applications have been studied in [27].

2.6 Mach-Zehnder Interferometer

The Mach-Zehnder interferometer (MZI) as an all-optical switch has been proposed by Tajima et al. [28], which uses the band filling effect in the fiber (Figure 2.9) [29]. High-speed operation is possible because of its unique switching mechanism. Here, both arms have nonlinear portions, where the control pulses induce nonlinear refractive index changes. When the first control pulse is absorbed in the nonlinear portion 1 and the band filling nonlinearity induces the refractive index change, the signal output is switched from one port to the other port. If shortly after the first control pulse, the second control pulse is absorbed in the nonlinear portion 2, the effect of the first control pulse is cancelled. Thus, the signal switches back. Nearly square modulation is possible in case of short control pulse widths and a sufficiently short time interval between the control pulses compared to the nonlinear relaxation time.

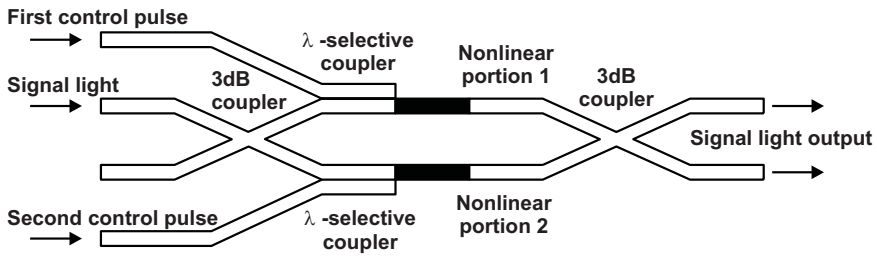

Figure 2.9 Fiber based symmetric MZI all-optical switch after [29].

Also, asymmetric MZIs have been used for all-optical switching. MZI comprising two asymmetrically placed SOAs and two 3 dB coupler was used for demultiplexing [30]. The asymmetry and the length of the SOAs determine

the switching window comparable to the SLALOM based on counter-propagating clock and data pulses. The length of each arm and the asymmetric location of the SOAs are realized by an adjustable time delay in each arm [30]. By detecting the clock signal output and actively adjusting the piezoelectric translator one can compensate the instability of a fiber based MZI.
An 80 Gbit/s error free all-optical demultiplexing experiment was reported by using a hybrid symmetric MZI consisting of polarization insensitive gain clamped-SOAs [31]. Hybrid interferometers base on Mach-Zehnder structure exploit the nonlinearity in passive waveguides and SOAs [30], [31]. Due to the instability of the hybrid arrangements the development of these nonlinear interferometers as monolithically integrated devices is indispensable for their use in real system applications.

2.7 Monolithically Integrated Mach-Zehnder Interferometer

Until recently, nonlinear interferometer structures for demultiplexing were primarily assembled as nonlinear Sagnac interferometers by using discrete semiconductor optical amplifier (SOA) components incorporated within an optical fiber loop [32], [16], [18], [22]. In such hybrid SOA/fiber devices it is usually necessary to employ the Sagnac configuration in combination with a polarization controller in order to handle the instability of path length and polarization due to thermal/acoustic fluctuations. Other hybrid interferometer arrangements like Mach-Zehnder interferometers, which exploit nonlinearity in passive waveguides, and SOAs have also been reported [29], [30]. Due to the instability of the hybrid arrangements the development of these nonlinear interferometers as monolithically integrated devices is indispensable for their use in real system applications.
The first all-optical demultiplexing experiment by using a monolithically integrated asymmetric MZI was demonstrated at data rates up to 40 Gbit/s by Jahn et al. [33]. The 500 µm long SOAs were displaced longitudinally by 300 µm, corresponding to a time delay of 3 ps (Figure 2.10).

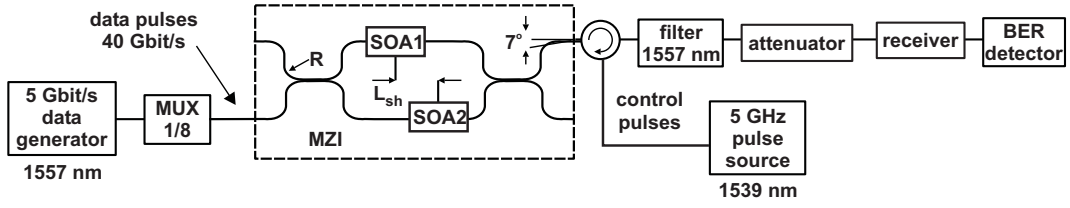

Figure 2.10 Experimental setup, a monolithically integrated asymmetrical MZI for demultiplexing after [33].

Using this asymmetrical MZI arrangement, add/drop multiplexing at 20 Gbit/s was also shown [34]. The first application of an all-optical switch in a computer network was demonstrated by using the monolithically integrated MZI as a channel selector in a 40 Gbit/s optical TDMA LAN [35].
A symmetric Mach-Zehnder interferometer structure, which was developed for wavelength conversion in WDM applications, can be used for all-optical demultiplexing [36]. With this structure 80 to 10 Gbit/s all-optical demultiplexing has been reported (Figure 2.11) [37]. Two additional arms allow saturating the SOAs separately. By varying the delay between the control pulses the switching window can be chosen flexible. The improved version of this symmetric MZI reported recently [38] has a better extinction ratio and avoids the use of external filter.

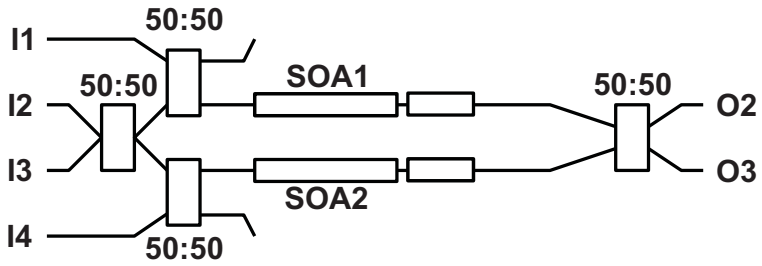

Figure 2.11 A monolithically integrated symmetric MZI structure after [37].

2.8 Brief Summary of Optical Demultiplexer

System requirements	Hybrid NLI	FWM	PIC-NLI
Operating power dependence	+	+	+
Speed of response (SOA as NLE)	+	+	++
Optical loss	-	+	-
Device size	-	-	++
Spectral range and sensitivity	+	-	+
Polarization sensitivity	-	-	+
Walk-off	-	+	+
Spectral purity	+	+	+
Latency	+	+	++
Stability	--	+	++

Table 2.1 The summarized comparison of hybrid and integrated NLI, FWM. The sign ‘+’means appropriate, the sign ‘-’ means non appropriate.

The realization of optical demultiplexers for OTDM applications started in the early nineties. In this short time period various structures have been investigated. In this chapter the milestones in the development of optical demultiplexing have been summarized and different OTDM demultiplexer structures have been presented, respectively: EAM, SLALOM, TOAD, UNI, MZI, FWM, MLLD, monolithically integrated SI and monolithically integrated MZI. The comparison of the three basic concepts for demultiplexing is summarized in the Table 2.1 regarding the system requirements [39].
The advanced hybrid NLI structures like SLALOM/TOADs cannot fulfill all the system requirements. Compared to the integrated counterparts, they are larger in size, relatively thermal sensitive and instable. The FWM method is unpractical for demultiplexing system applications because of the wavelength-shifted output, the required high power for operating and its low signal-noise ratio. The photonic integrated nonlinear interferometric devices based on SOAs are compact and stable compared to their hybrid counterparts. Different interferometer structures are applicable: SI, asymmetric- and symmetric MZI (Table 2.2).
The switching window of SI is defined by the position of off-center placed SOA in the waveguide loop. External filter and circulator are needed. The asymmetric MZI can be used only for counter-propagating control- and data-signals, which on the other hand avoids the need of external filters. The switching window is determined by the longitudinal displacement of the SOA. The symmetric MZI with two additional arms for the control inputs allows bit-rate flexibility. The external delay between both control inputs determines the switching window. The data and control pulses can propagate co- and contra-directional. The cascadeablity and add/drop function of the symmetric Mach-Zehnder structure increase its attractiveness to be used in network nodes as a compact device.

	SI	Asymmetric MZI	Symmetric MZI
Number of 3 dB couplers	2	2	4
Number of SOAs	1	2	2
Co-propagating	No	No	Yes
Counter-propagating	Yes	Yes	Yes
External filter	1	0	1
Min. number of ports	3	3	4
Bit-rate	Fixed	Fixed	Flexible

Table 2.2 Comparison of different integrated interferometric arrangements.

3 Novel ‘Gain Shifted’ All-Optical Switching Scheme

In this chapter the all-optical switching architecture will be discussed. Furthermore, a novel switching scheme will be introduced and compared with other existing solutions.

3.1 All-Optical Switching Architecture

As introduced in the previous chapters, the all-optical switches are essential components in high-speed OTDM systems, whenever the data rate exceeds the speed of electronics. The general principle of the all-optical switches relies on the control of light by light (Figure 3.1). For this purpose, an optical control signal is used to change the optical properties of a nonlinear medium. The device then switches the data signal, which experiences the changed transmission properties when it covers the medium. Fibers, crystals, and semiconductors can be employed as nonlinear media in various configurations. As described in Chapter 2, the semiconductor optical amplifier as a nonlinear media is of particular interest, since it provides low switching powers, short interaction lengths, high compactness, as well as the possibility for monolithic integration.

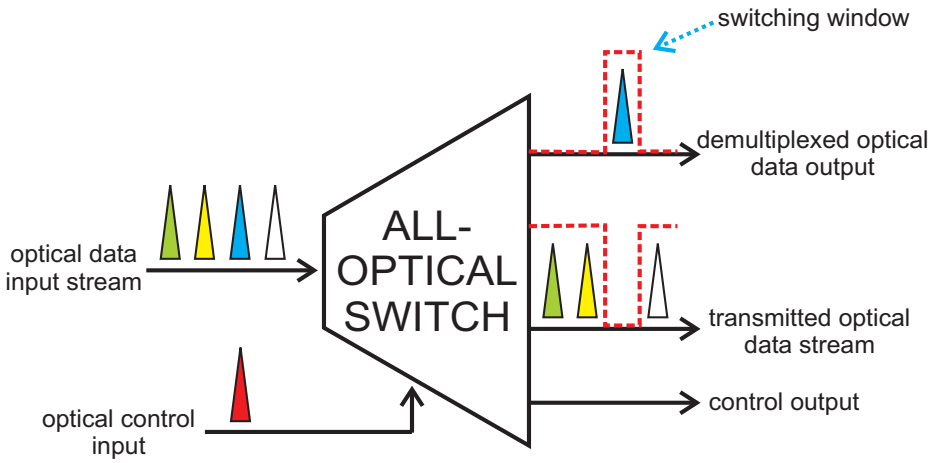

Figure 3.1 All-optical switch as a black box with its inputs and outputs.

As illustrated in the Figure 3.1 an all-optical switch has two inputs, one for the data signal and a second for the control signal. For different switching applications special requirements are needed. Demultiplexing, add/drop multiplexing, sampling are some of these special applications in the all-optical signal processing. In case of all-optical demultiplexing the switches should have high contrast ratios, for all-optical add/drop multiplexing additionally they should have low distortion and high contrast for the transmitted data and in case of all-optical sampling high linearity is essential.
The requirements for demultiplexing cover the fundamental ones for optical switching and exemplary on this type of switch the development of all-optical switches will be realized, which is the topic of this thesis. The approaches to realize the optical demultiplexing application have been summarized in the Chapter 2.
In the development of the switch for all-optical signal processing the following aspects have to be taken into account:

- The geometry of the switch
- The switching scheme

Also the geometries for all-optical demultiplexing have been discussed in detail in the realization approaches (section 2.8), in terms of the given system specifications. The nonlinear interferometric switches are attractive to fulfill the requirements of communication systems. Due to the advantages of monolithically integrated symmetric Mach-Zehnder interferometers as an all-optical switch (section 2.8), the investigations within this research work are focused on the development of the monolithically integrated symmetric Mach-Zehnder interferometer based on the semiconductor optical amplifiers (Figure 3.2).

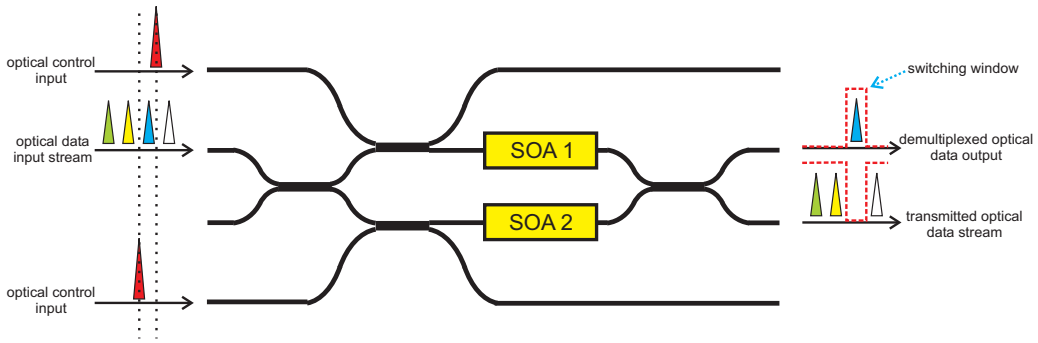

Figure 3.2 Schematic of monolithically integrated symmetric Mach-Zehnder interferometer structures based on semiconductor optical amplifiers.

The combination of operating wavelengths and the material band gap (or gain maximum) of the semiconductor optical amplifier within the symmetric Mach-Zehnder interferometer defines its switching scheme. During the last years, three different switching schemes have been persuaded the investigations on the all-optical switching:

- Conventional switching scheme [33]
- 'Gain transparent' (GT) switching scheme [23]
- 'Gain shifted' (or 'band gap shifted') (GS) switching scheme [40]

The operating principles of these three all-optical switching schemes are illustrated in the Figure 3.3 or Figure 1.4.

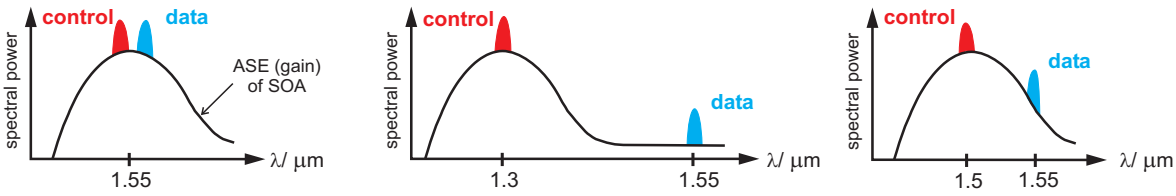

a) Conventional b) GT c) GS

Figure 3.3 The all-optical switching schemes, regarding the material and operating wavelength.

3.2 Conventional Switching Scheme

The conventional operation principle of a semiconductor optical amplifier is depicted in Figure 3.3a. Here, a schematic spectrum of the amplified spontaneous emission (ASE) or the gain of the SOA with the spectra of the control and the data signal are shown. The gain maximum of the conventional SOA is at 1550 nm, in the center of the C-band. Both of the signals, for the optical data and the optical control, are also in the C-band. They are close to each other and placed near the gain maimum of the conventional SOA. The optical control signal saturates the SOA with its high power and the data signal experiences the gain, the refractive index and the phase change. The phase modulation is used for interferometric switching within the Mach-Zehnder interferometer. In the conventional switching scheme both of the optical signals are close to each other and they are placed on the top of the gain curve of the SOA.

The Figure 3.4 illustrates a typical gain recovery curve of a SOA in the conventional switching scheme and the transmitted data. The transmitted data shows a high variation in the amplitude.
Present SOA based all-optical switches, using the conventional scheme, have the following disadvantage: the optical control signal causes a phase and an amplitude change of the data signal. The phase change is used for switching, while the unwanted amplitude change causes a degradation of the contrast ratio of the switch and an amplitude modulation of the transmitted data signal. Additionally, there is a strong contribution of ASE noise to the transmitted signal and also the amplification of the transmitted signal.

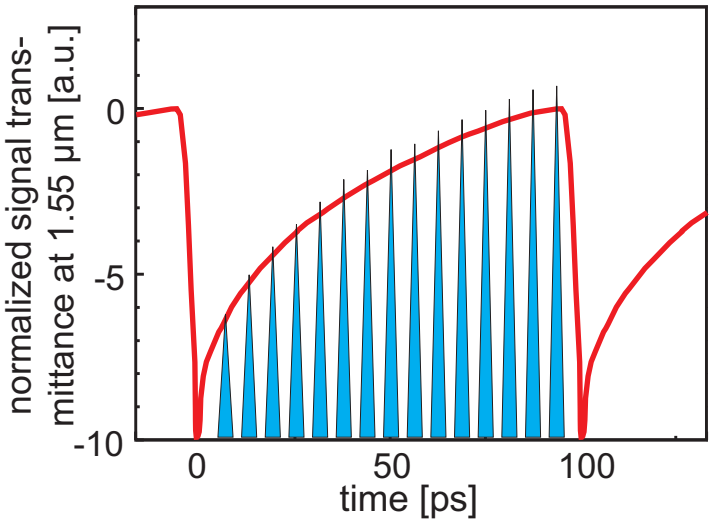

Figure 3.4 Illustration of gain recovery curve of a SOA in the conventional switching scheme and the transmitted data at 160 Gbit/s.

3.3 Gain Transparent Switching Scheme

Recently, the ‘gain transparent’ (GT) switching scheme had been reported using a hybrid interferometer arrangement [23]. The GT operation principle of an SOA is depicted in Figure 3.3b. A schematic spectrum of the ASE or the gain of the SOA with the spectra of the control and the data signal are shown. Key element in the GT switching configuration is the SOA with its gain maximum at 1300 nm. An optical data signal at the wavelength of 1550 nm and an optical control signal at the wavelength of 1300 nm are coupled into the GT switch. The optical data signal is far outside of the SOA gain curve while the optical control signal is placed on the top of the SOA gain curve. Please notice that these wavelengths had been chosen due to the availability of the commercial SOAs and from this reason they are not optimized.

The Figure 3.5 illustrates the typical gain recovery curve of a SOA in the GT switching scheme and the transmitted data. In this switching scheme the transmitted data experiences no significant amplitude variation, because it is far from the gain curve of the SOA.

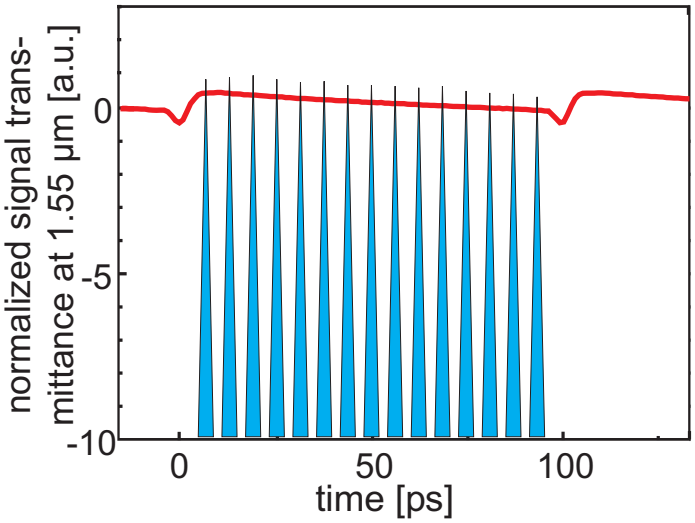

Figure 3.5 Illustration of gain recovery curve of a SOA in the gain transparent switching scheme and the transmitted data at 160 Gbit/s.

In contrast to a conventional nonlinear interferometric switch, the data signal is far from the gain- and ASE maximum of the SOA. Thus, the data experiences a negligible amplitude change and only extremely low noise is added. This is due to the fact, that the photonic energy of the data pulses is significantly lower than the band gap energy of the semiconductor material. However, still a significant phase change of the data signal can be observed around the data wavelength of 1550 nm induced by the optical control signal at 1300 nm due to carrier depletion in the amplifier [41].
The GT switch is superior to the conventional switches and combines superior linearity, low noise, wide bandwidth, high switching contrast and low cross-talk with an expected potential to be monolithically integrated [42]. System experiments at 160 Gbit/s have been reported **Fehler! Verweisquelle konnte nicht gefunden werden.**.
The advantages of the gain transparent switching scheme compared to the conventional switching scheme are:

- No ASE noise
- No pattern effects
- Linearity
- Wide bandwidth

- High switching contrast
- Low cross-talk
- High optical signal to noise ratio

The disadvantages of the transparent switching scheme are:

- Incompatible with other all-optical devices
- High insertion loss
- Reduced phase change

3.4 The Novel ‘Gain Shifted’ Switching Scheme

To avoid the disadvantages of the described switching schemes, a new scheme has been developed for monolithically integrated Mach-Zehnder switches. The novel scheme is the so-called ‘gain shifted’ (or ‘gain shifted’) (GS) switching scheme [40]. Hereto, the SOAs with their gain maximum at 1500 nm are integrated within the symmetric MZI. The gain maximum of the SOAs is shifted by ~50 nm towards shorter wavelengths compared to the wavelength of the data signal.

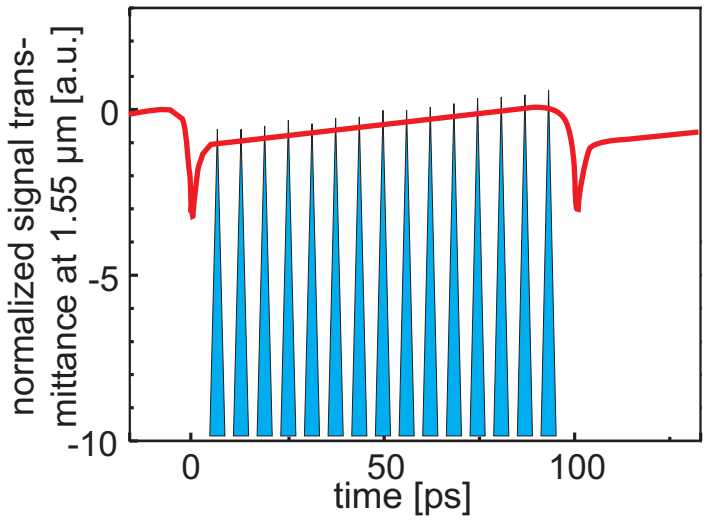

Figure 3.6 Illustration of gain recovery curve of the SOA in the GS switching scheme and the transmitted data at 160 Gbit/s.

In Figure 3.3c, a schematic spectrum of the ASE or the gain of the SOA with the spectra of the control and the data signal are depicted for the GS switching scheme. The optical data signal is at 1550 nm as usual; the optical control signal is relative far from the data at the gain peak of the SOA, respectively.

In this scheme in contrast to a conventional switch scheme (Figure 3.3a) the data signal is far from the gain- and ASE maximum of the SOA.
The Figure 3.6 illustrates the gain recovery curve of a SOA in GS switching scheme and the transmitted data. While the data signal still experiences the phase shift introduced by the control signal, gain and ASE at the data wavelength are strongly reduced. This leads to an enhanced noise reduction, better linearity and so to a reduced pattern effect compared to a conventional scheme. The transmitted data signal experiences a negligible amplitude change and only extreme low noise is added.

3.5 Expected Advantages of the Novel GS Switching Scheme

The demonstration of the GT switching scheme opened new frontiers with its advantages compared to the conventional switching scheme [41]. The induced phase change is essential for all-optical interferometric switches, but the amplitude modulation is unwanted, because it reduces the contrast ratio of the switch and causes an amplitude modulation of the transmitted data signal. Compared to the conventional scheme, the GT switch provides no ASE noise, no pattern effects, linearity, wide bandwidth, high contrast ratio and low cross-talk.
However, the GT switching scheme has also its drawbacks: it is not compatible with other all-optical devices, since an all-optical wavelength conversion from 1550 nm wavelength range to 1300 nm is not available. This will reduce the practical application because a control signal at 1300 nm is essential for the GT scheme. Additionally, the data signal experiences no gain; it will be only attenuated, which brings practical limitations regarding the cascadeability and low signal output power.
The novel GS switching scheme should overcome these limitations and provide comparable advantages as the GT switching scheme. The expected advantages of the GS scheme compared to the conventional switching scheme are [40]:

- Reduction of the ASE noise
- Reduction of the pattern effect
- Better linearity
- High switching contrast
- Low cross-talk
- Enhanced phase change

The expected advantages of the GS scheme compared to the GT switching scheme are:

- Compatibility with other all-optical devices
- Low insertion loss

The characteristics of these three switching schemes can be summarized in Table 3.1.

	Conventional	GT	GS
Gain maximum of SOA	1550 nm	1300 nm	1500 nm
λ_{data}	C-band		
$\lambda_{control}$	At the gain maximum of the SOA		
Pattern effects	High	No	Low (expected)
ASE noise	High	No	Low (expected)
Linearity	Low	High	High (expected)
Contrast	Low	High	High (expected)
Compatibility	High	Low	High (expected)
Insertion loss	Low	High	Low (expected)
Phase shift	High	Low	Low (expected)
Cross-talk	High	Low	Low (expected)
OSNR	High	High	High (expected)

Table 3.1 Typical characteristics of the switching schemes.

Additionally the GS switching scheme is compatible with the all-optical clock recovery proposed within the all-optical signal regeneration concept. This is a prerequisite for advanced applications of the MZI switches e.g. in a complete true all-optical 3R regeneration scheme.
Since data- and control-signal wavelengths are within the C-band, GS scheme allows a wavelength translation by using the all-optical wavelength converter.
Despite these clear advantages the GS switching scheme, it is a challenge from the point of view of monolithic integration, as widely separated wavelengths are necessary.

4 Polarization Insensitive Design

In this chapter, the realization approaches and basic optical components of the monolithically integrated symmetric MZIs will be analyzed. Furthermore, the polarization insensitive monolithically integrated GS-MZI design will be presented.

4.1 Buried Hetero Structure Monolithic Integration

A large variety of integration schemes have been reported in the literature for InP material systems [44]. Many of these are applicable to the monolithical integration of SOA based interferometers. For example, very compact all-active wavelength converters were built using multi-section active devices without any separate passive waveguide sections [45]. More complicated solutions have to be utilized in case of active/passive integration [33]. There are two main layer structures for the active components (SOAs) of the monolithically integrated MZI, which instructs the monolithical integration:

- The ridge waveguide (RW) structure
- The buried hetero (BH) structure

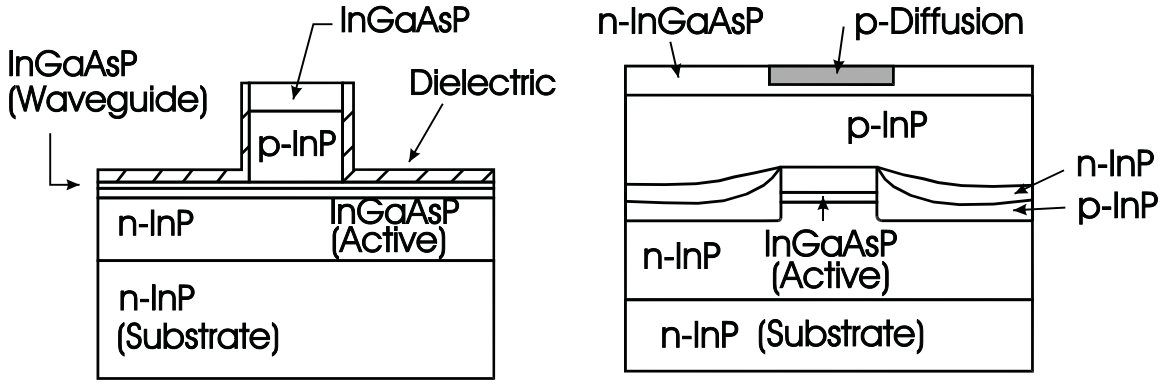

a) RW structure b) BH structure

Figure 4.1 The two basic layer structures for the realization of the monolithically integrated MZI after [46].

In the RW structure (Figure 4.1a), the use of dielectric around the ridge inhibits current spreading in the p-InP layer [46]. RW provides an effective index step of ~10^{-2} for the lateral mode under the ridge, and the mode is essential index guided. Lateral modes can be also controlled in a strongly index guide active region, which is buried in higher band-gap layers (e.g. InP) on all sides. For this reason, these structures are called BH structures (Figure 4.1b)[46]. The gain characteristics are primarily determined by a rectangular waveguide that confines the mode inside the buried active region. BH structures are difficult to fabricate compared to other structures. However, these strongly index guided structures are most suitable for demanding applications [46]. The RW and BH structures have been compared and summarized in the Table 4.1:

Ridge waveguide structure (RW)	Buried waveguide structure (BH)
Simple	Complex
Well known and common technology	Less used technology
Contacting of a ridge necessary	Easy contacting due to nearly planar structure
'Upside down' hybrid integration not possible	Due to nearly planar structure 'upside down' hybrid integration in optical 'back plane' possible
Low confinement of optical waves in waveguides large bending radii large overall device length	High confinement of optical waves in waveguides small bending radii, small overall device length

Table 4.1 Comparison of the two basic layer structures, ridge waveguide and buried hetero structure.

The RW technology is a well-known technology. The buried structures are well suited for contacting and they are also suited for larger integration platforms using flip-chip bonding. The contacting of the ridge eliminates the possibility of hybrid integration for a RW structure. Due to the higher confinement, the BH devices are more compact than the RW ones. Since a high chip gain and compact waveguides are required, the BH structure has been chosen for the integrated MZI devices in this research work. In the Figure 4.2, the schematic of the monolithically integrated Mach-Zehnder interferometer using the buried hetero structure has been depicted with its layer stacks for active and passive sections.

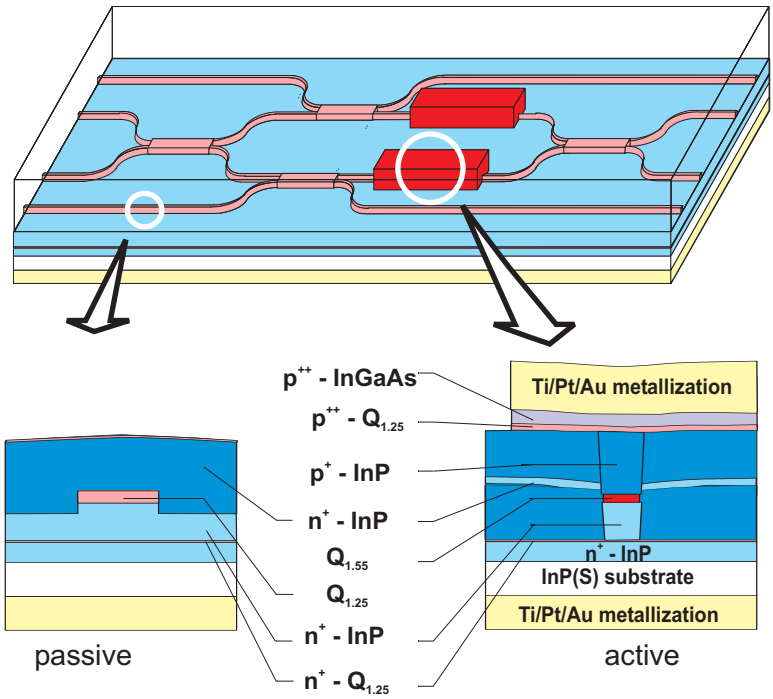

Figure 4.2 Schematic of the monolithically integrated MZI using the BH structure and its layers for passive and active sections.

4.2 Processing Technologies for Monolithically Integrated MZI

The fabrication (section 9.3) of such monolithically integrated Mach-Zehnder interferometer devices (Figure 4.2) can be proceeded using two processing technologies:

- Full-stack technology
- Half-stack technology

Full-Stack Technology

In the 'full-stack' technology, the complete amplifier (SOA) layer stack is grown first in an MOVPE process. Next the amplifier areas are defined, etched and overgrown by the waveguide layers with selective MOVPE. Then the waveguides are defined in the passive and in the amplifier area. The width of the active waveguide has to be reduced afterwards to ~0.8 µm by wet chemical etching to be single mode (Figure 4.3). Additionally with this etching step, the formation of 'ears' (hills alongside the amplifier stripes) occur-

ring in the following selective blocking overgrowth (pn-blocking or Fe-blocking) is reduced. The last steps are contacting and separation of the amplifiers.

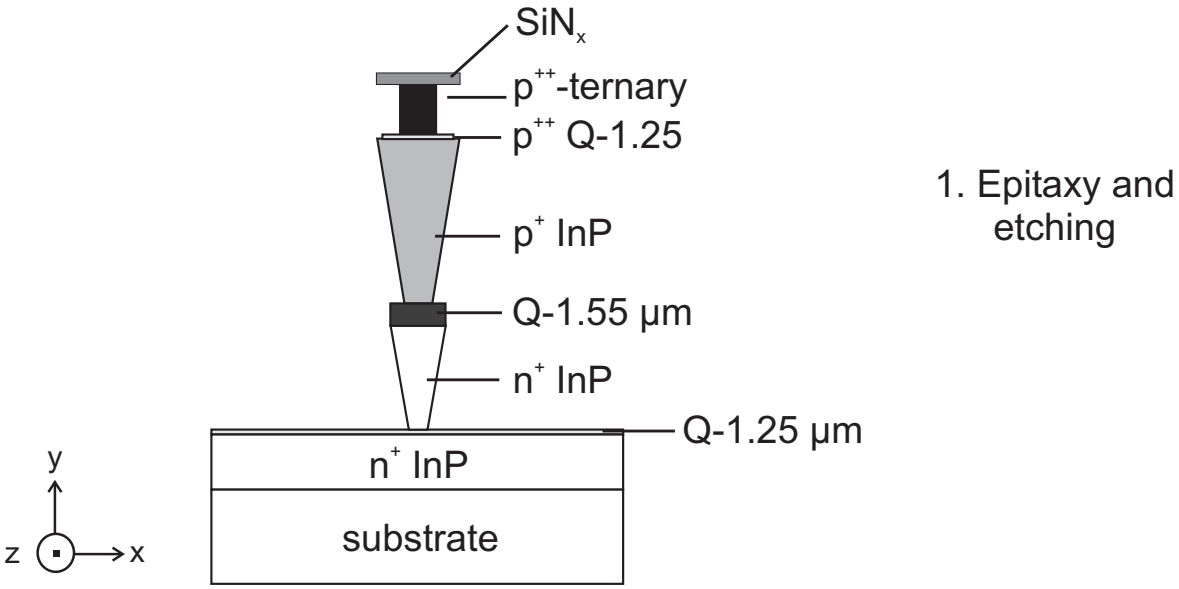

Figure 4.3 Scheme of ‘full-stack’ integration technology.

Investigations using electrical measurements and SEM pictures showed that the most critical point of this processing technique is the under etching step due to poor reproducibility and the possibility of strong under etching of the ternary contact layer This was the reason to establish another processing technology, namely ‘half-stack’ technology, described in the following section.

Half-Stack Technology

Using the ‘half-stack’ technology means that in the first epitaxial step only the basic layers up to the active layer are grown. Then the amplifier areas are defined, etched and selectively overgrown with the waveguide layers. After definition of the waveguides and a short wet chemical etching step to reduce the width of the active layer stripe the structure is overgrown in a second selective MOVPE growth step with the lower blocking layers and after removing the silicon nitride on top of the active layer with the top blocking layers. The width of the ternary contact stripe corresponds directly to the width of the overlying sputtered gold contact and is structured independently from the amplifier stripe (Figure 4.4).
Disadvantage of this technology is the necessary third overgrowth. Nevertheless first SEM pictures of samples cleaved from these wafers show a smoother overgrowth of the amplifier areas compared to the former structure.

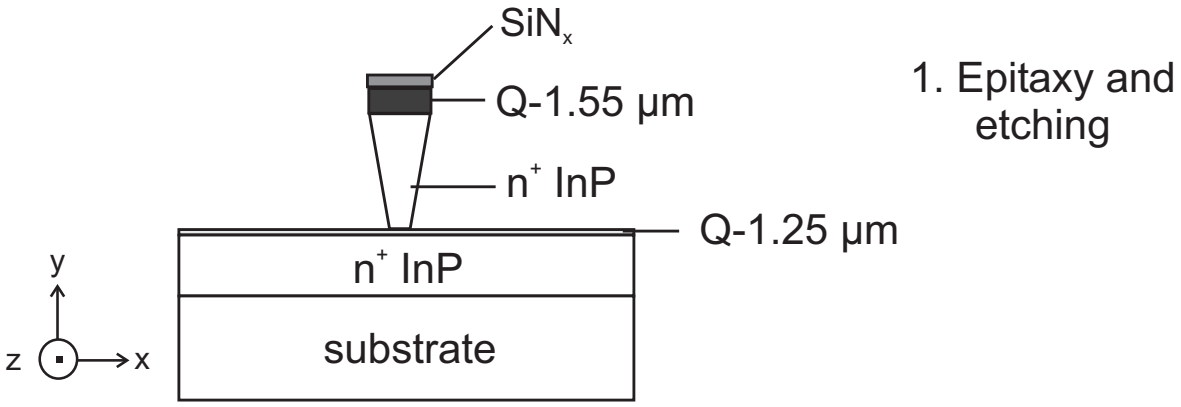

Figure 4.4 Scheme of 'half-stack' integration technology.

The comparison of 'full-stack' and 'half-stack' technologies is summarized in Table 4.2.

Full-stack technology	Half-stack technology
Simple	Complex
2 overgrowth steps	3 overgrowth steps
High overgrowth step (3 µm)	Minor overgrowth heights
Current limited by contact layer width	Current limited by active layer width
High serial resistance	Low serial resistance
	Separate isolation layer against leakage currents
Rough surface	Smooth surface
Poor reproducibility	Better reproducibility

Table 4.2 Comparison of full and half stack integration technologies.

4.3 Basic Components of Monolithically Integrated MZI

The monolithically integrated MZI comprises different types of basic optical components with special functionalities and requirements (Figure 4.5). The monolithically integrated MZI concerns namely the following components:

- Straight waveguides
- Waveguide bends
- 3 dB couplers
- Semiconductor optical amplifiers

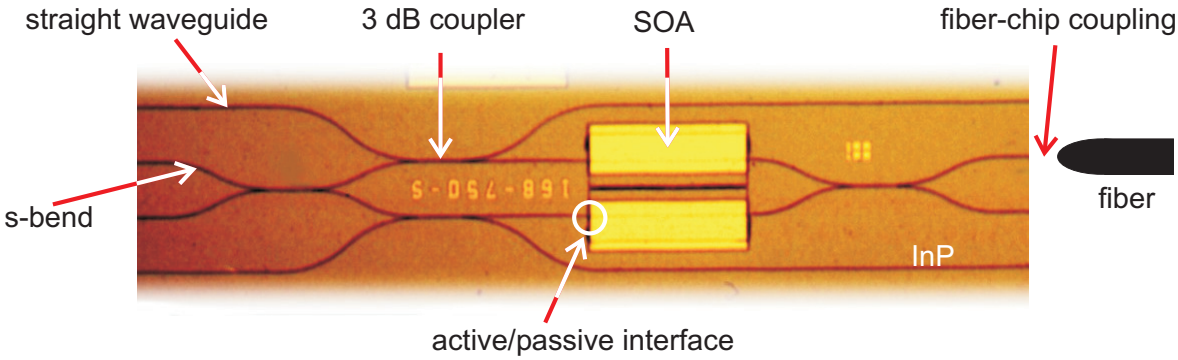

Figure 4.5 Photograph of a monolithically integrated symmetric MZI and its basic components.

Furthermore, the following three aspects determine also the design of a monolithically integrated device:

- Active/passive interface
- Fiber-chip coupling
- Integration scheme

Monolithically integrated interferometer chips require a passive waveguide network, which is at least as difficult to design as the active devices. Passive components (straight waveguides, 3 dB coupler, s-bends) should be transparent at the operating wavelength in order to keep the chip losses small. The waveguide bends should be as compact as possible in order to efficiently utilize the chip area. The fast SOAs with high gain are essential. Active/passive interface and fiber-chip coupling should exhibit low reflections and high efficiency.

4.4 Straight Waveguide

Of high importance are the properties of the passive sections since they bring up nearly 80% of total propagation length in a monolithically integrated MZI device for the optical waves.
The basic characteristics of the buried passive waveguides (Figure 4.6) as designed for the use in the monolithically integrated MZI are summarized in the Table 4.3, with the material parameters of n_1= 3.16 for InP and n_2= 3.37 for InGaAsP ($\lambda_{Passive}$=1.25µm).

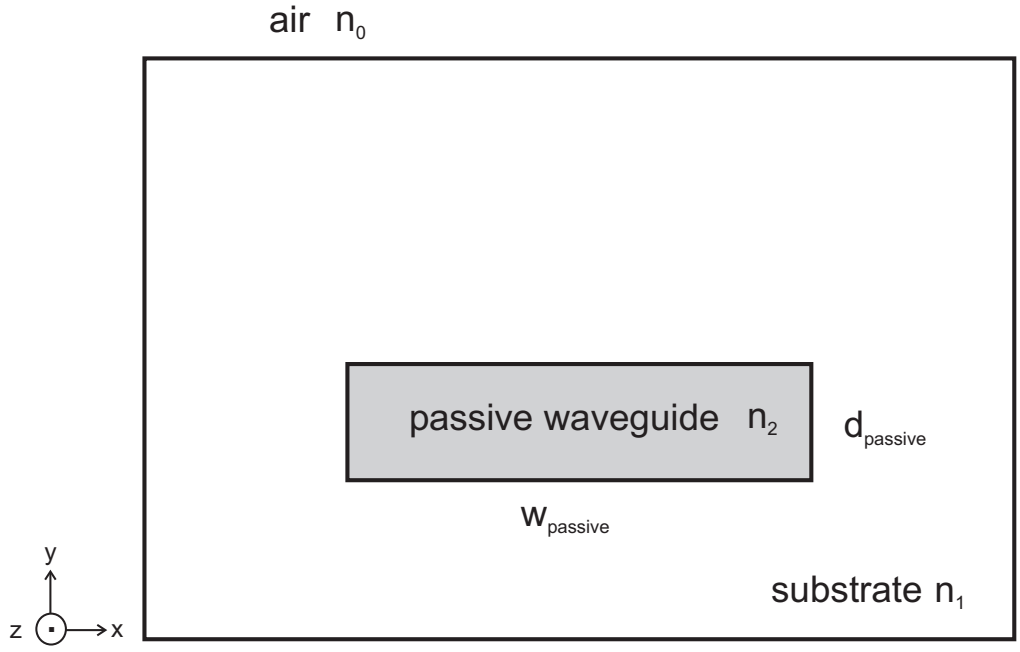

Figure 4.6 Cross section of the buried passive waveguide.

Mode order	Γ_{TE}	Γ_{TM}	$\Gamma_{TE} / \Gamma_{TM}$	n_{eff}(TE)	n_{eff}(TM)
0	0.55	0.51	1.08	3.23	3.22
1	0.44	0.39	1.11	3.19	3.18

Table 4.3 Confinement factors and effective refractive indices of the buried passive waveguide for TE, TM.

Due to the rectangular structure of the passive waveguide shown in Figure 4.6, increased losses of 10% to 20% of the TM polarization mode compared to the TE polarization can be observed. As this is a constant contribution to the overall losses, it can be compensated by careful adjustment of the whole structure.
In the passive sections the waveguide mode(s) should be well confined and transparent at the operating wavelength in order to keep the losses low. However, the waveguide should remain single mode at least within the interferometer arms. Because of the relatively large refractive index step between InGaAsP and InP layers, the thickness ($d_{passive}$) of the single mode waveguide was chosen to be 0.35 µm. For single mode operation in the lateral direction $\leq$ 1.2 µm wide waveguide stripes are required. In order to avoid such small dimensions, a new concept of mode filtering by circular bends was utilized. In this approach, $w_{passive}$=2 µm wide double-mode waveguides are fabricated.

4.5 Waveguide Bends

In the passive sections the waveguide mode(s) should be well confined and transparent at the operating wavelength in order to keep the bend losses low.
In order to reduce complications due to the second order modes within the interferometer branches, at the inputs of the multi-mode interference couplers very small circular bends with a radius of only 250 µm are used as mode filters [47]. All other bends are used with radii of 500 µm to reduce the overall optical losses.
The principle of mode filtering based on small bend radii can be easily understood from bend-loss calculations after Marcuse [48]. Marcuse's model is based on the calculation for a straight slab waveguide of thickness d and refractive index n_2 surrounded by material of the refractive index n_1 and n_3 on both sides, respectively. This slab is bent to form a hollow cylinder of radius R_{Bend}. The fields outside the hollow cylinder are calculated by solving the Bessel form of the wave equation. The amount of power lost into the space outside the cylinder is

$$P_{Loss} = P_{Mode} \{1-\exp(-2a\,\theta\, R_{Bend})\}, \qquad (4.1)$$

where P_{Mode} is the launched power, 2a is the loss coefficient, R_{Bend} is the radius of curvature and θ is the angle subtended by the bend at its center of curvature [47]. The loss coefficient for guided modes with a propagation constant β is given by [47]

$$2a = \frac{2\kappa^2 e^{2\gamma w} \gamma e^{-U}}{\beta(2w + 1/\gamma + 1/\Theta)(n_2^2 - n_1^2)k^2} \qquad (4.2)$$

where

$$U \cong \frac{2}{3}\left(\frac{\gamma}{\beta}\right)^2 \gamma R_{Bend}\ , \qquad (4.3)$$

$-\gamma^2 = n_1^2\, k^2-\beta^2$, $\kappa^2 = n_2^2\, k^2-\beta^2$, $-\theta^2 = n_3^2\, k^2-\beta^2$ and $k = 2\pi/\lambda_0$.

More accurate calculations done by Ch. Schmidt [49] using three-dimensional finite difference simulations result in bending losses for TE fundamental mode shown in the Figure 4.7. Based on these results, the waveguide bends with the radius of the 250 µm are almost lossless.

Due to the fact that the pure bending losses for the TM polarization are always lower than for TE polarization, for both polarization states the waveguide bend can be presumed to be lossless and therefore polarization insensitive for the fundamental modes.

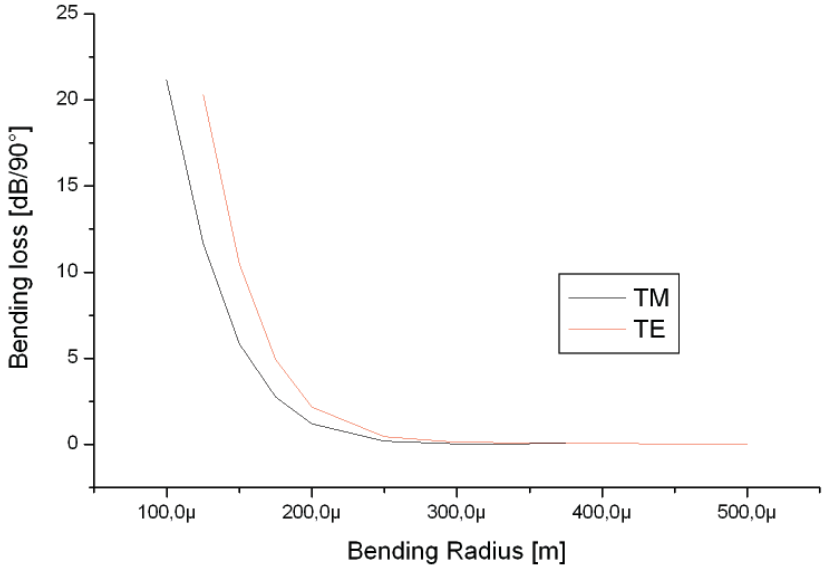

Figure 4.7 Bending losses of TE fundamental mode in the dependence of the bending radii after [49].

For the higher order modes the bending losses are increasing exponentially. This effect is used for mode filtering of the higher order modes, to provide only fundamental mode excitation at the input of the MMI couplers.
Please notice that a polarization rotation cannot be observed since the bending radius is large enough.

4.6 Multi-Mode Interference Coupler

The 3 dB-coupling ratio of the integrated coupler must be accurate to within a few percent. There are two main coupler types, which can be used for monolithical integration: the ‘directional coupler’ and the ‘multi-mode interference (MMI) coupler’. MMI couplers have been chosen for the integrated MZI, because they can be designed within sub-millimeter lengths in contrast to the several millimeter long standard directional couplers [47].
The operational principle of MMI couplers is based on the self-imaging effect in the multi-mode waveguides as suggested by Bryngdahl [50] and studied by Ulrich [51]. When light is launched into a multi-mode waveguide, each mode propagates along the guide with its own characteristic phase velocity. How-

ever, at a certain waveguide length, in so-called image planes, the accumulated phase differences between various excited modes are relatively close to a multiple of 2π.
Assuming a highly multi-mode slab waveguide of effective refractive index n_{eff} and width w_{MMI}, the propagation constant of supported modes are given by [52]

$$\beta_{0m} \approx \frac{2\pi n_{eff}}{\lambda_0} - \frac{\pi\lambda_0 (m+1)^2}{4 n_{eff} w_{MMI}^2} = \frac{2\pi n_{eff}}{\lambda_0} - \frac{\pi (m+1)^2}{3L_\pi} \quad , \qquad (4.4)$$

where λ_0 is the free space wavelength, m is an integer and L_π is the beat length of two lowest order modes. In this respect the length of the MMI section L_{MMI} equals $(p/q)3L_\pi$. If (p/q) is even or odd, this means the coupler works in bar or cross-state, respectively.
By using the three-dimensional finite difference simulations [53], polarization independency of the coupler can be ensured, provided only the fundamental mode is coupled into the MMI coupler [54].
For the 3 dB MMI coupler the calculated dimensions are 212 µm in length L_{MMI} and 6.5 µm in width w_{MMI} (Figure 4.8).

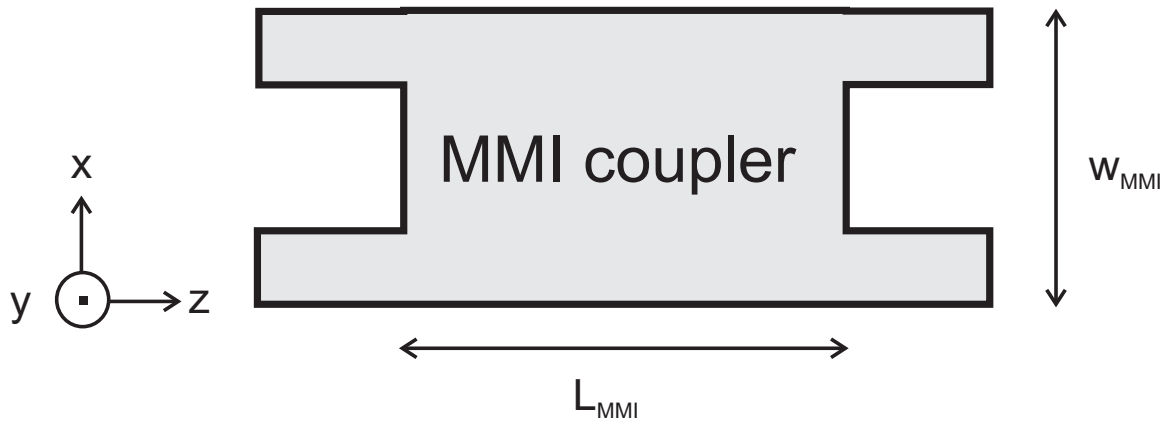

Figure 4.8: Structure of the MMI coupler.

The theoretically expected insertion loss is about 0.07 dB [54], due to mode-mismatch between access waveguide and MMI waveguide. The MMI coupler design shows only negligible polarization sensitivity. In Figure 4.9 the field distribution within a 3 dB MMI coupler is depicted.

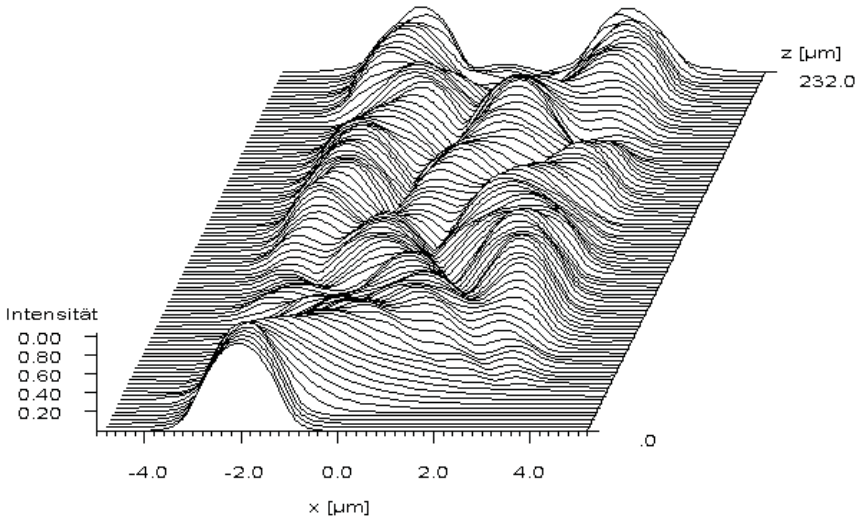

Figure 4.9 Intensity plot of 3dB MMI coupler field distribution.

The polarization sensitivity of the MMI coupler is depicted in the Figure 4.10, which shows ratio of output powers P_{bar} and P_{cross} for the bar and cross output ports of the MMI, in the dependence of its length, for both TE and TM polarizations, respectively. The red lines indicate the given 1 dB polarization sensitivity of the MMI coupler. This results in a coupling length tolerance as shown by the blue lines. With respect to a given polarization sensitivity of 1 dB, the length of the MMI coupler is tolerant within more than 20 µm.

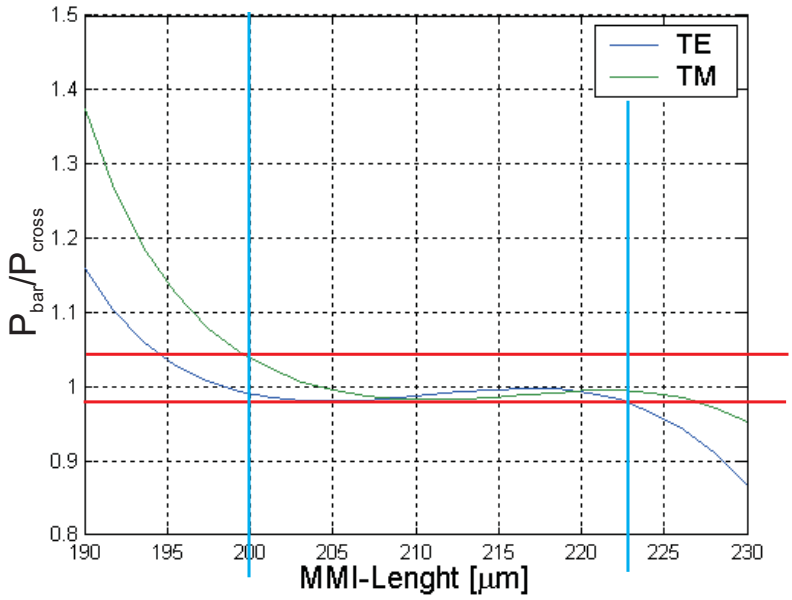

Figure 4.10 Polarization sensitivity of the MMI coupler in the dependence of its length.

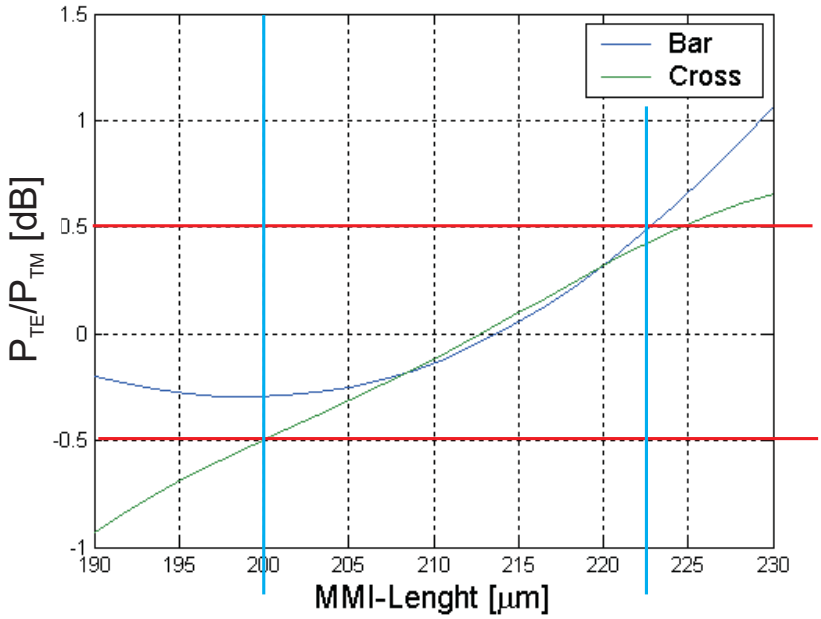

Figure 4.11 The coupling ratio of the MMI output ports (bar, cross) for both TE and TM fundamental mode excitations.

The coupling ratio of the MMI output ports (bar, cross) for both TE and TM fundamental mode excitations is shown in the Figure 4.11. The blue lines indicate the tolerance of the MMI length defined in the Figure 4.10.The red lines indicate the deviation of the MMI coupler from the 3 dB coupling point for this given tolerance. In this given tolerance, the deviation from the ideal 3 dB coupling point is less than ±5%.
For both TE and TM fundamental modes, the excess losses at both output ports (bar, cross) of the MMI coupler are minimized, since 3 dB coupling conditions are required. With respect on the polarization sensitivity the length of the MMI coupler is tolerant.

4.7 Active/Passive Interface

To achieve an optimized active/passive interface it is essential to find a good match between the guided modes in both active and passive waveguides. Since the field distribution in active and passive waveguides is similar for a given polarization state, field matching in the active/passive interface region can be assumed to be equal for both polarization states TE and TM, if aspect ratios and the materials are comparable. Presumed a good field matching is given, the active/passive coupling is polarization insensitive.
There are two basic active/passive coupling schemes, namely leaky-coupling and butt-coupling (Figure 4.12).

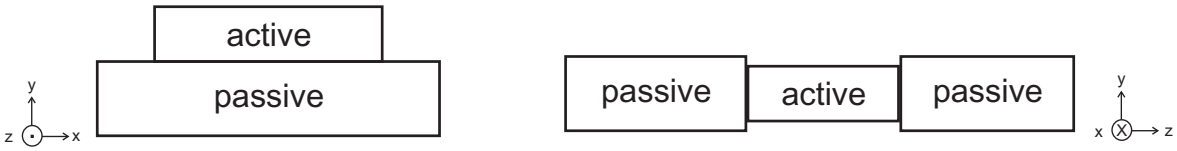

a) Leaky-coupling b) Butt-coupling

Figure 4.12 Principle of coupling schemes for active and passive waveguides.

The calculated losses for the butt-coupling scheme are lower [54]. However, butt-coupling scheme requires an additional epitaxial step. This leads to complex fabrication of such integrated structures.
Due to the small difference of the refractive indices between active and passive waveguides, the reflections at this interface are low ($< 10^{-3}$). For a usage of the SOA (high gain corresponding to large phase change for a given optical control signal) without lasing effects, reflections must be further reduced. The reflections had been reduced by using a shallow etching of the SOA mesa before the selective overgrowth for the passive waveguide layers, which lead to a vertical angled interface (Figure 4.13).

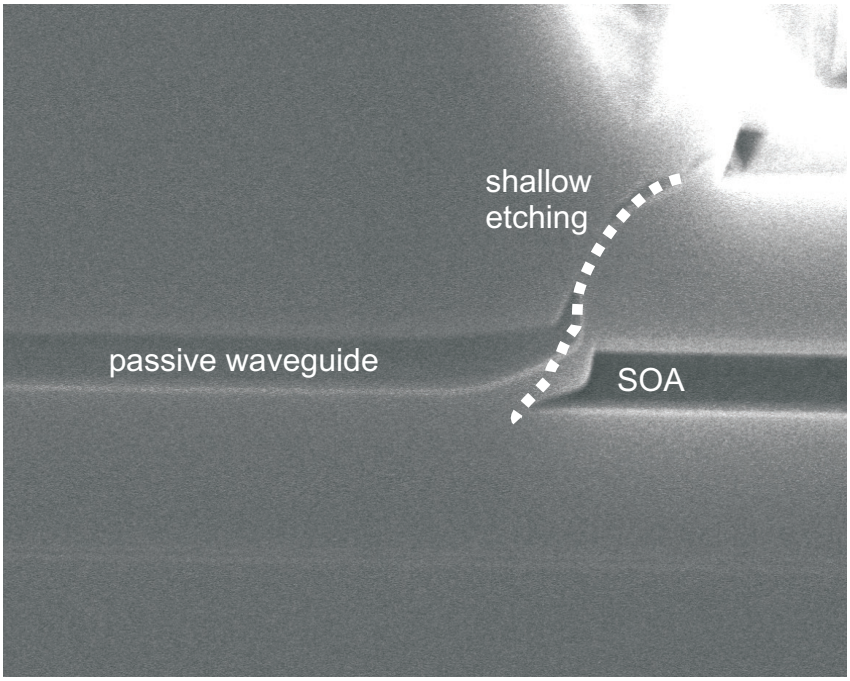

Figure 4.13 SEM picture of a shallow etched active/passive interface.

However, this method had only a poor reproducibility, as the shape of the shallow etching step is hard to control. Therefore a lateral antireflection design has been introduced by an angled transition between active and passive waveguides (Figure 4.14). With this measure, a well controllable vertical mesa etching step can be used, without loosing the antireflection behavior of

the butt interface. It has to be admitted that with the new design the adjustment tolerances for the masks in the waveguide direction are reduced, but are still well manageable within the tolerances of the photolithography.

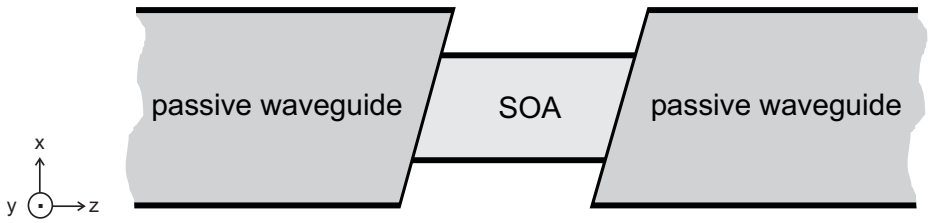

Figure 4.14 Scheme of angled interface between active (SOA) and passive waveguides.

4.8 Fiber-Chip Coupling

The fiber-chip coupling is one of the most critical points regarding their direct effects on the overall chip losses and reflections caused distortions. Because of the reflections at the chip facets the gain over the whole chip can written as (for negligible waveguide losses) [55]:

$$G_{FP} = \frac{(1-R_1)G_S(1-R_2)}{(1-G_S\sqrt{R_1R_2})^2 + 4G_S\sqrt{R_1R_2}\sin^2\varphi} \qquad (4.5)$$

with

$$\varphi \approx \frac{\lambda - \lambda_m}{\Delta\lambda_r} \qquad (4.6)$$

where R_1 and R_2 are the power reflection factors in the cavity length L, G_S is the single pass gain of the SOA, λ_m are the wavelengths of modes in the SOA and $\Delta\lambda_r$ is the distance between the mode maxima.
To suppress the end facet reflectivity different approaches can be used. These are anti-reflection coating, angled facets, spot size converter and window region.

Anti-Reflection Coating

In order to reduce the end facet reflectivity, commonly an anti-reflection (AR) coating is used.

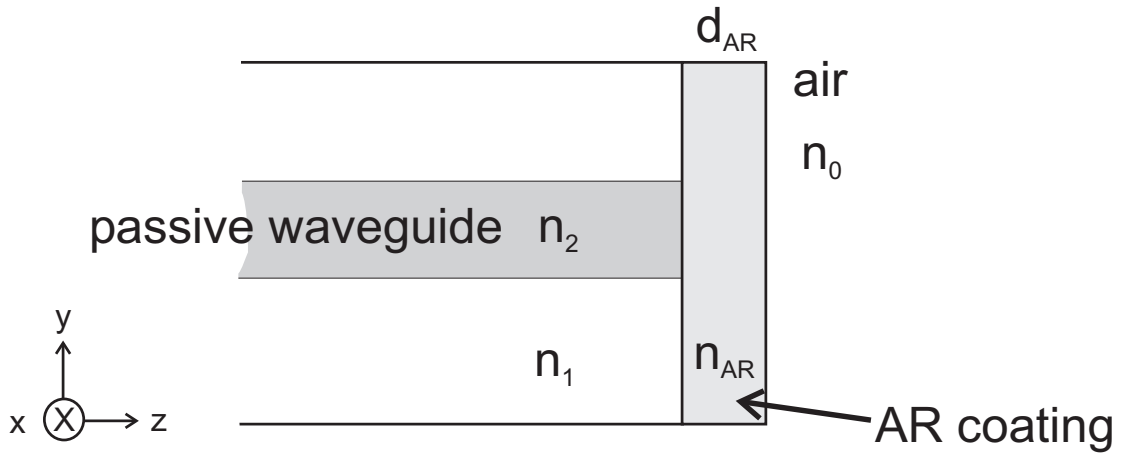

Figure 4.15 Passive waveguide with anti-reflection coating.

The thickness d_{AR} for a single layer AR-coating, for a plane wave with a wavelength of λ, which is normally incident from air to a homogeneous isotropic medium with a refractive index n_{AR} (Figure 4.15), can be written as [55]:

$$d_{AR} = \frac{\lambda}{4n_{AR}} \qquad (4.7)$$

Antireflection coating conditions for TE and TM modes are different as the facet reflectivity depends on the polarization direction. This difference becomes very noticeable for a waveguide thickness equal to $1 / n_2$. To satisfy the conditions for both polarizations multi layer AR-coating can be used, both the refractive index and the thickness of the coating films must be controlled in this case.

In case of the monolithically integrated MZI devices facet reflections leading to laser action of the integrated SOAs have to be avoided. Using a double layer AR-coating comprising a high index TiO_2 layer and low index SiO_2 layer are used for this purpose [55]. This method leads to a reflectance down to $< 10^{-4}$. The thickness of the AR-coating layers is depending on the desired spectral minimum of the reflection curve, on the effective index of reflection of the coated waveguide structure and on the angle of the waveguide to the facet [56].

The polarization dependence of the AR-coating depends on the combination of the AR-coating layer thickness and its refractive index [57]. It should be always feasible to achieve a polarization independent AR-coating by proper choice of the AR-coating parameters.

Angled Facet

To prevent the integrated SOAs from lasing at high control currents the reflectance of the facets has to be further reduced (< 10^{-5}). This can be done by introducing angled facets (Figure 4.16), were the waveguides are penetrating the facet with an off-axis angle. An angle of 7° is mostly chosen [55] and is leading to a further reduction of the reflectance.
By slanting the waveguide from the cleavage plane the effective reflectivity, the coupling between the guided field and the reflected field from the cleaved facet, can be reduced.

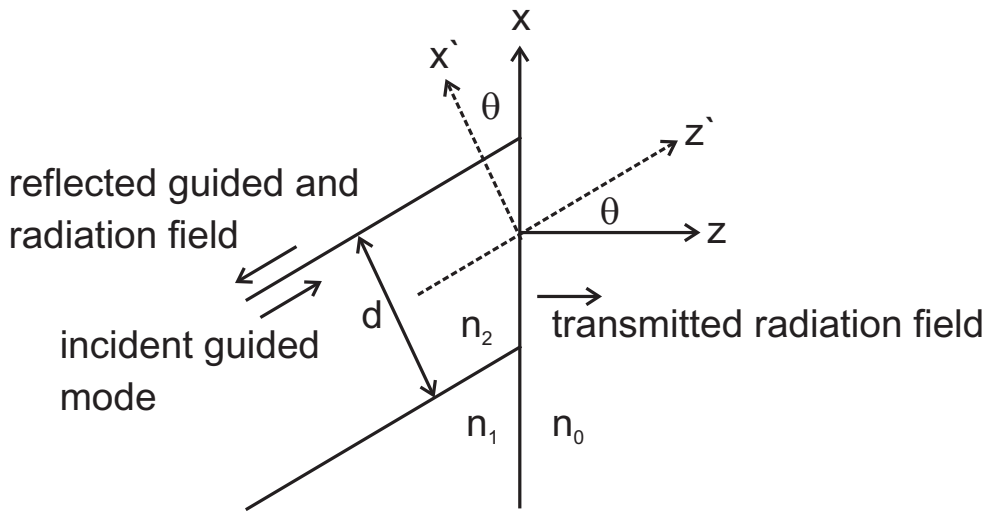

Figure 4.16 Angled slab waveguide showing core index n_2, cladding index n_1 and the simple 1D facet in air of index $n_0 = 1$ after [57].

The average reflectivity decreases with an increase at the facet angle θ. However the coupling efficiency between chip and an optical fiber degrades for large facet angles due to the asymmetry of the far field pattern.
For facet angles larger than 12° the coupling of the fiber gets impracticable since the coupling angles become larger than 45° due to the high refractive index of the passive waveguide (e.g. n_2 in section 4.4).
The effective reflectivity also decreases by increasing the waveguide width, because the angular spectrum of the reflected wave is narrowed.
It is obvious that the minimum of the reflectance is shifted to shorter wavelengths and, may be even more important, is split into a TE and TM part with different minima in heights and wavelength. Additionally the minimum of the average reflectance is reduced to ca. $7 \cdot 10^{-4}$. This has to be taken into account in optimizing a given structure. The width and the depth of the minima of the reflectivity for the angled facet changes with the facet angle θ.

Window Facet Region

Introducing a window region (Figure 4.17), which is supposed to be a transparent region between the end of the waveguide and the cleaved end of the chip, can also reduce the effective reflectivity [55]. However this cannot be ensured easily and causes additional losses for the guided field in the monolithically integrated device. The disadvantage of the window region is its additional loss which is not suitable for photonic integrated circuits. Therefore this is only used if AR-coating and angled facets do not lead to a sufficient reduction of facet reflectivity.

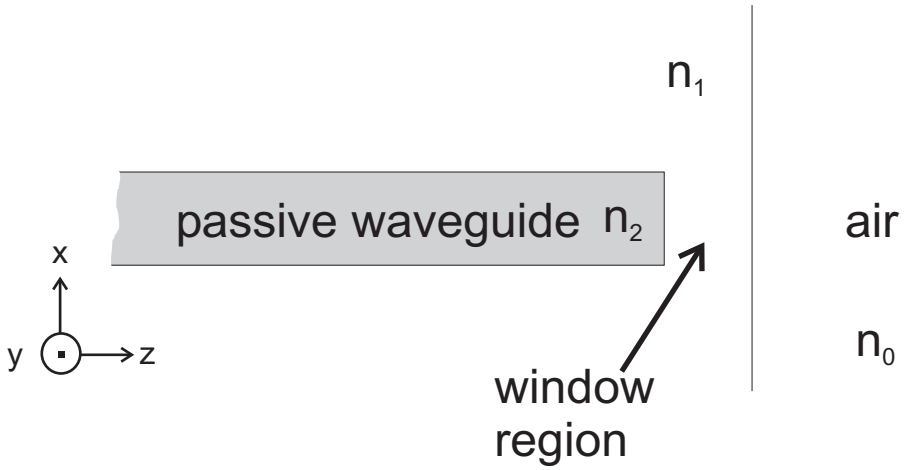

Figure 4.17 Window facet region for a buried passive waveguide.

Spot Size Converter

The kind of fiber-chip coupling has a direct effect on the overall chip losses. Low loss coupling demands a butt joint with a field distribution matched to the fiber. Since the field distributions of the fiber and waveguide are different, a matching of the fields is essential. In this respect, a spot size converter has to be designed with a nearly square profile of the waveguides at the edges of the chip by reducing the width of the buried waveguide. This results in nearly identical far-field properties of the waveguide tapers for TE and TM modes in the x- and y-directions (Figure 4.18). In this way not only coupling losses are decreased, but also the tolerances for the fiber-chip coupling are enhanced. This is indispensable for a reproducible packaging of the devices.
By increasing the aspect ratio of the waveguide, the polarization dependence of the waveguide reflectivity increases. In case of a square cross section (aspect ratio = 1) the reflectivity of both TE and TM fundamental modes are equal, a waveguide tapered to this geometry shows polarization independent coupling behavior, at least for perpendicular coupling. In other words by ta-

pering the waveguide the polarization sensitivity at a fiber chip coupling can be eliminated.

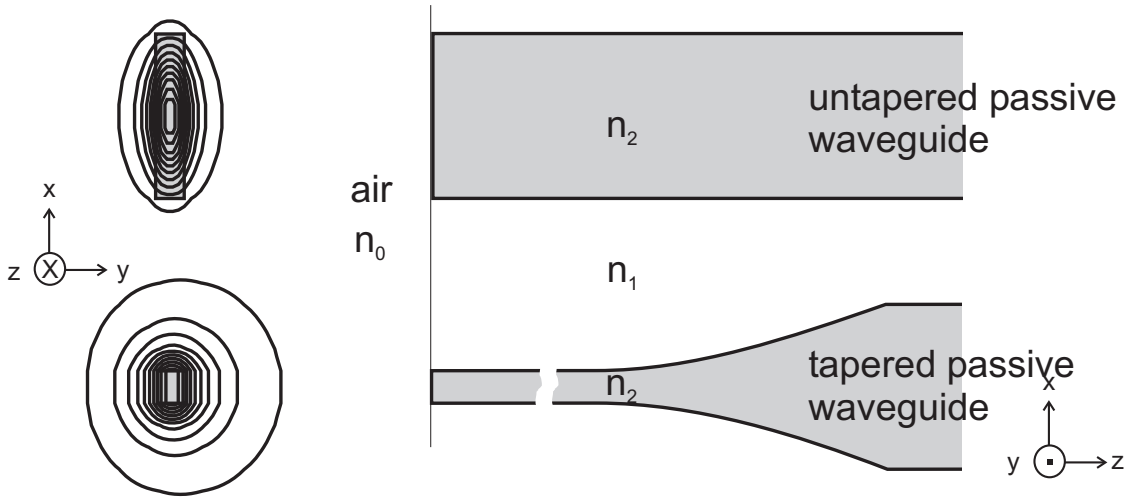

Figure 4.18 Comparison of far fields for tapered waveguide and untapered waveguide.

Combination of Anti-Reflection Coating, Angled Facet and Spot Size Converter for the Realization of Monolithically Integrated Mach-Zehnder Interferometer

Based on these basic approaches a combination of anti-reflection coating, angled facet and spot size converter is used in the realization of monolithically integrated Mach-Zehnder interferometer (Figure 4.19), to provide a low loss fiber-chip interface.

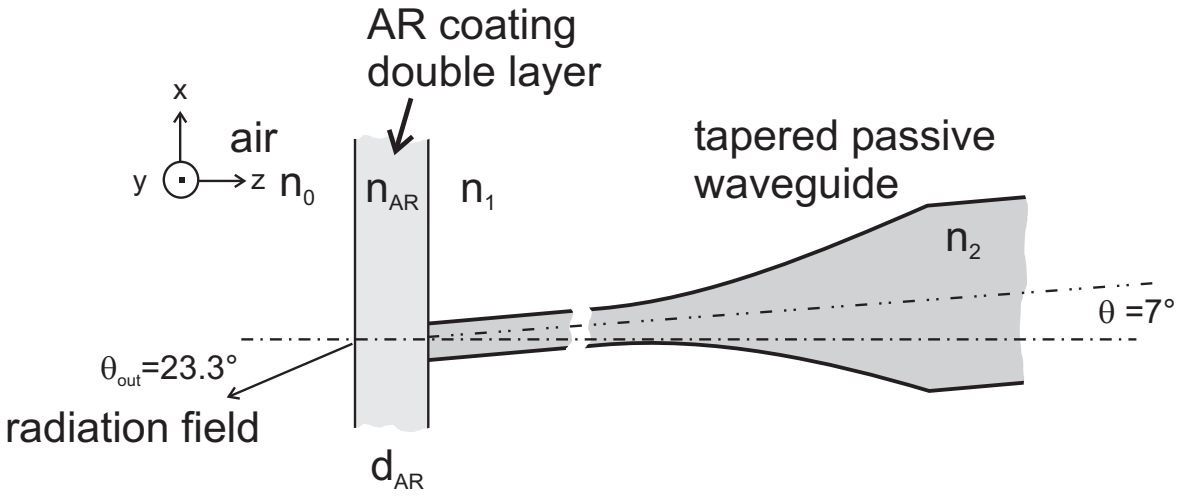

Figure 4.19 Designed fiber/chip coupling with angled facet, AR-coating and spot-size converter for monolithically integrated MZI.

The Figure 4.20 shows such an optimized reflectance curve calculated for an effective index $n_{eff} = 3.24$ and perpendicular waveguides, resulting in layer thickness of 115.6 nm (TiO_2) and 188.6 nm (SiO_2), respectively [58]. There is no polarization dependence of the residual reflections in this case of perpendicular facets.

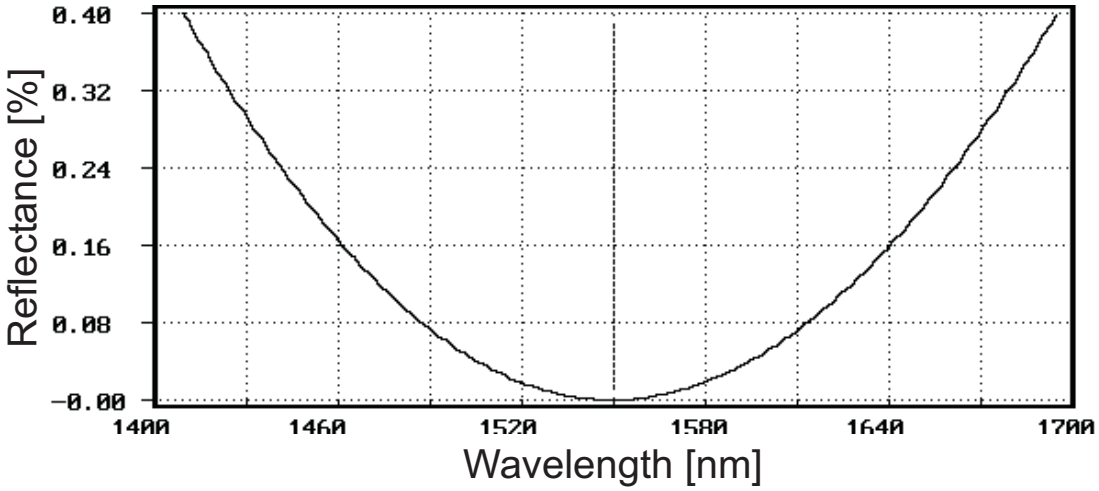

Figure 4.20 Reflectance (in %) as a function of wavelength for perpendicular facets $R_{av} = 0$ (ideal!) at $\lambda_0 = 1550$ nm after [58].

In Figure 4.21 the influence of the off-axis angle of the waveguide (Figure 4.19) is shown. For the calculations [58] the same basic parameters as in Figure 4.20 have been used. The off-axis angle θ_{out} for the fiber is calculated to 23.3° according to the equation 4.8

$$\theta_{out} = \arcsin (n_{eff} \cdot \sin(\theta)) \quad , \qquad (4.8)$$

with θ is off-axis angle waveguide; n_{eff} is effective refraction index of waveguide structure; θ_{out} is off-axis angle fiber (surrounding medium is air).
As described the AR-coating has to be adapted to the fabricated structure. As shown in the Figure 4.21, the usage of angled facets leads to a shift of the reflectance minimum to the shorter wavelengths compared to the depicted spectrum in the Figure 4.20 and also to a splitting of the reflectance for TE and TM modes.

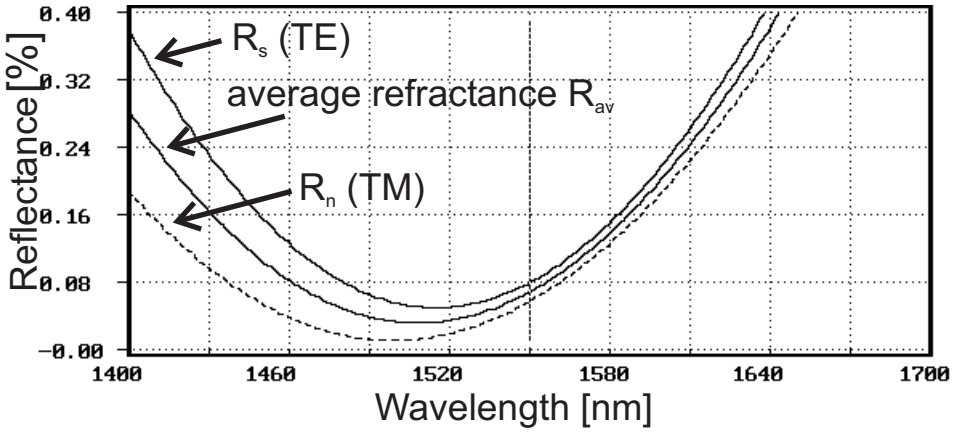

Figure 4.21 Reflectance (in %) as a function of wavelength for facets tilted by 7°, $R_{av} = 6{,}8 \cdot 10^{-4}$ at $\lambda_0 = 1550$ nm after [58].

In order to apply a polarization independent AR coating the thickness of the coating layers have to be corrected. This is depicted in the Figure 4.22. The off-axis angle in air is set to $\theta_{out} = 23.3°$ according to the equation 4.8. The reflectance can not be tuned to 'zero' ($< 10^{-4}$) because for angled facets the TE and the TM reflection cannot be set to 'zero' at the same time. Nevertheless, the combination of the angled facet and AR-coating can be sufficient for an effective suppression of the reflections from the facets. For a deeper understanding of the challenges concerning the AR-coating, the angled facets and their polarization dependence can be found in [59].

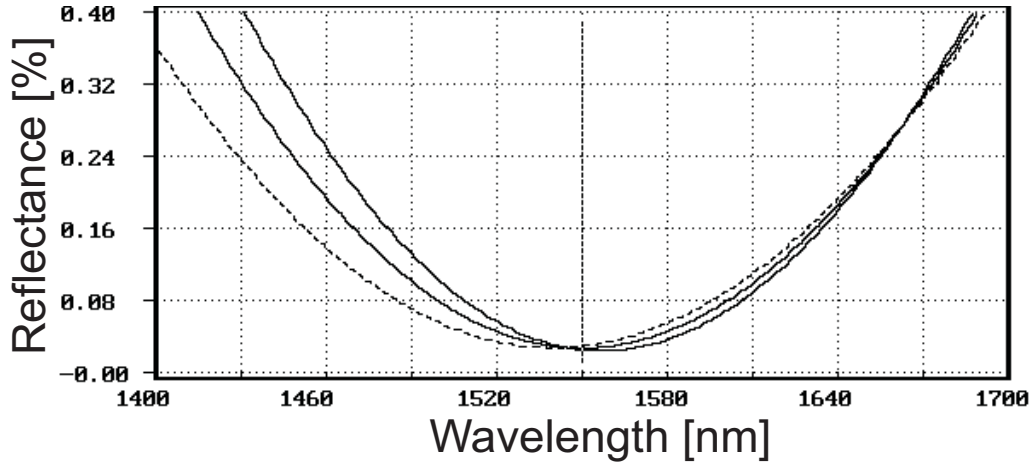

Figure 4.22 AR-design for 7° angled facet and $\lambda_0 = 1550$ nm, resulting to a reflectance of $R_{av} = 2.7 \cdot 10^{-4}$ layer thickness: $TiO_2 = 117.2$ nm, $SiO_2 = 196.3$ nm after [58].

As depicted in the previous sections the near square dimensions of the passive waveguides at the fiber-chip coupling are necessary for an effective low loss coupling. Therefore the width of the passive waveguides has to be tapered down to 0.4 µm-0.6 µm. The reproducibility of the traditional processing methods for long small structures with a width < 0.5 µm is quite poor. Such a dimension is necessary for the described passive waveguide tapers. Therefore, for the structures of this geometry the expensive and time intensive E-beam direct writing method is used. For the monolithically integrated Mach-Zehnder interferometer, an alternative process the devices has been developed [60].
Regarding the reproducibility and the polarization sensitivity, the spot size converters are realized with nearly square cross section (Figure 4.23). The nearly square cross section dimensions of the spot size converter (400 nm x 350 nm) is reproducible and has only low polarization sensitivity. For the conversion from the normal passive waveguide widths to the small dimensions, an exponential shape has been designed as shown in the Figure 4.18, leading to a good adiabatic behavior with no radiation.

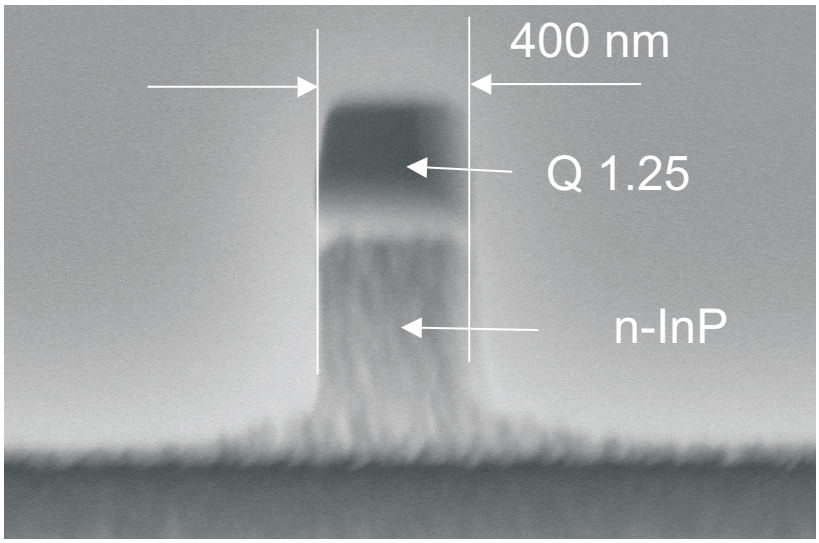

Figure 4.23 SEM picture of a passive waveguide with its spot size converter.

However there is a trade off between low coupling losses due to the small taper dimensions and losses due to the enhanced free carrier absorption in the p-doped cladding layers, which can not be omitted because of the integration concept. Here, a combination of the waveguide tapers with slightly larger dimension (~0.6 µm in width) and of fiber tapers leads to the coupling losses of ~4 dB and with moderate coupling tolerances of ~1 µm.

4.9 Integrated Semiconductor Optical Amplifier

The semiconductor optical amplifier is the most important element for the functionality of the monolithically integrated MZI. SOAs have been studied in great detail by several authors. The mechanism responsible for providing gain in SOAs is the same as in lasers. The optically active medium of an SOA is electrically pumped with carriers, which results in population inversion [61]. A light signal entering such an active medium is amplified by stimulated emission of radiation. In a monolithically integrated MZI the nonlinear effects in the active medium are used for switching. Here, primarily the gain and phase dynamics of SOAs are of interest, since its nonlinearity changes by an injected control signal.
The gain G of the SOA at a given wavelength is generally described by the following equation [62]:

$$G = \exp(\Gamma\, g\, L) \qquad (4.9)$$

where Γ is the confinement factor, g is the material gain and L is the cavity length of the SOA.
The transmitted waves in an SOA cavity experience different amplifications regarding their polarization states, depending on the confinement factor of the guided mode and on the material parameters of the SOA. Based on this model the polarization sensitivity of the SOA can be written as a gain difference between both polarizations [62]:

$$\Delta G_{TE/TM} = G_{TE}\left(1 - \frac{\Gamma_{TM}\, g_{TM}}{\Gamma_{TE}\, g_{TE}}\right) \qquad (4.10)$$

To achieve polarization independency, an identical modal gain for TE and TM is required; the gain difference $\Delta G_{TE/TM}$ should be zero.
It is easier to achieve low polarization sensitivity by increasing the confinement factors in the structure. As shown in the Figure 4.24 and Figure 4.25 to achieve a given polarization sensitivity of 3 dB and 1 dB the tolerance or the difference between both confinement factors ($\Gamma_{TE} - \Gamma_{TM}$) increases with increase of the value of the mode confinement factor. Here, G_{TE} assumed to be equal to 100 (20 dB) and $gL=\log(G_{TE})/\Gamma_{TE}$.
The same approximation can also be done for the material gains. By increasing the material gain the system shows an increased tolerance for a given polarization sensitivity. Different approaches are used to obtain polarization independent SOAs.

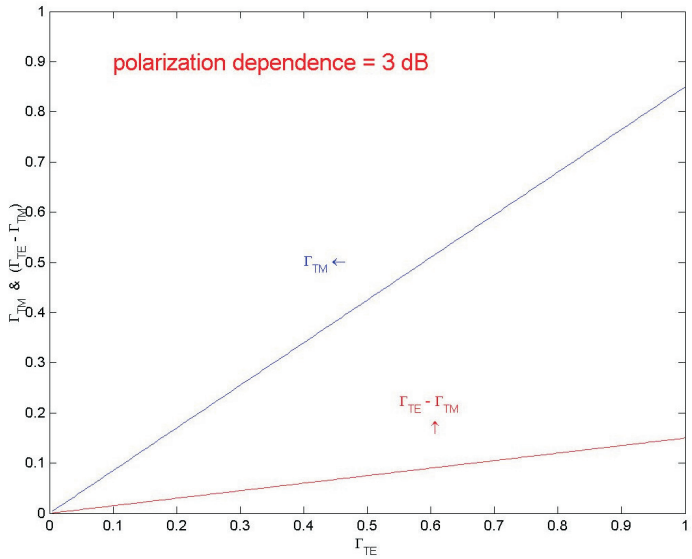

Figure 4.24 Difference between both confinement factors (Γ_{TE} - Γ_{TM}) for a polarization dependence of 3 dB.

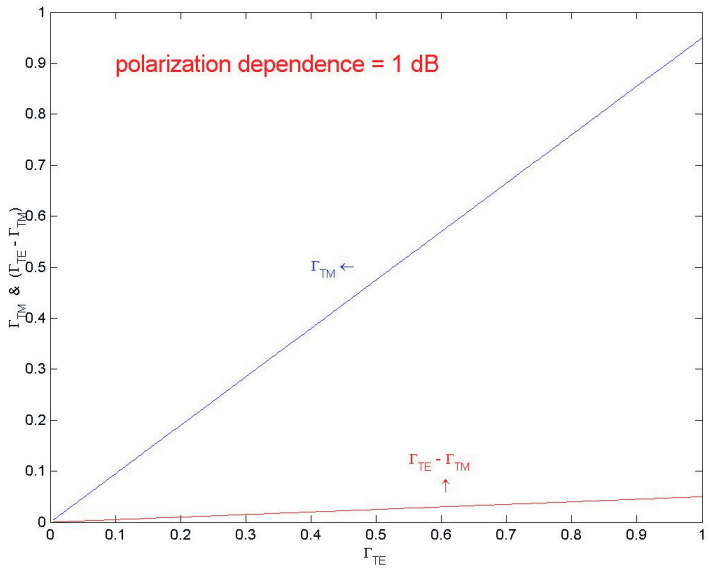

Figure 4.25 Difference between both confinement factors (Γ_{TE} - Γ_{TM}) for a polarization dependence of 1 dB.

Polarization Diversity

The polarization diversity [55] approach provides a SOA for each polarization, TE and TM separately. The gains of the SOA should to be equal for their corresponding polarization.
This can be realized by splitting the optical field in two equal parts. Both parts are amplified by SOAs in different paths. The SOAs should be similar and

their active regions should be rotated relative to each other by 90°. This provides the following polarization insensitivity condition for the gain of the first (G_{1TE}, G_{1TM}) and the second SOA (G_{2TE}, G_{2TM}):

$$G_{1TE} + G_{2TE} = G_{1TM} + G_{2TM} \qquad (4.11)$$

where

$$G_{1TE} = G_{2TM} \text{ and } G_{1TM} = G_{2TE} .$$

The realization of this approach is difficult because of the typical aspect ratios of the SOAs.

Separate Confinement Layer

The separate confinement layer approach follows from equation (4.10). From this equation it becomes clear that a zero gain difference can only be achieved if the terms $\Gamma_{TE}\, g_{TE}$ and $\Gamma_{TM}\, g_{TM}$ are equal. Conventional SOAs are isotropic in gain but have different confinement factors for both polarizations. One approach to adjust the modal gains of the SOA is to adjust the confinement factors for the two different polarizations. For this adjustment it is necessary to stretch the effective height of the active region to enlarge the confinement factor for the TM polarization. This can be realized with separate confinement layers placed directly below and above the active region (Figure 4.26).

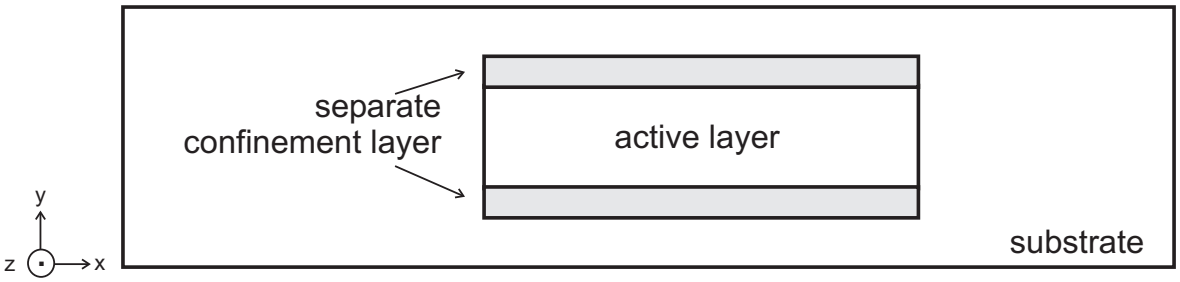

Figure 4.26 Cross section of semiconductor optical amplifier with separate confinement layers.

Tensile Strain

As stated in the previous section, the modal gains of the SOA have to be adjusted for both polarizations to obtain polarization insensitivity. The separate confinement layers realize the matching of the confinement factors. As an alternative to matching the confinement factor, it is feasible to match the mate-

rial gains of the SOA for both polarization states TE and TM. For the realization of this approach an anisotropic material gain is necessary. For this a tensile strained active region can be used. Based on the fine-tuning of the strain, the material gains can be matched and a polarization independent SOA can be realized. Even if the fine-tuning process is very complicated, this is today's most favored approach for polarization independent semiconductor optical amplifiers [62].

Combination of Separate Confinement Layers and Tensile Strain for the Realization of Monolithically Integrated Mach-Zehnder Interferometer

The basic characteristics of the active waveguides (Figure 4.27) as used in the monolithically integrated MZI are summarized in the Table 4.4, with n_1=3.16 for InP and n_3=3.57 for InGaAsP (λ_{active}=1.53 µm). Due to the rectangular cross section, the integrated SOAs show different optical gain for the TE and the TM modes, respectively. Based on the theoretical statements in this section, there are two basic schemes, which have been used to reduce the polarization sensitivity of the semiconductor optical amplifier.

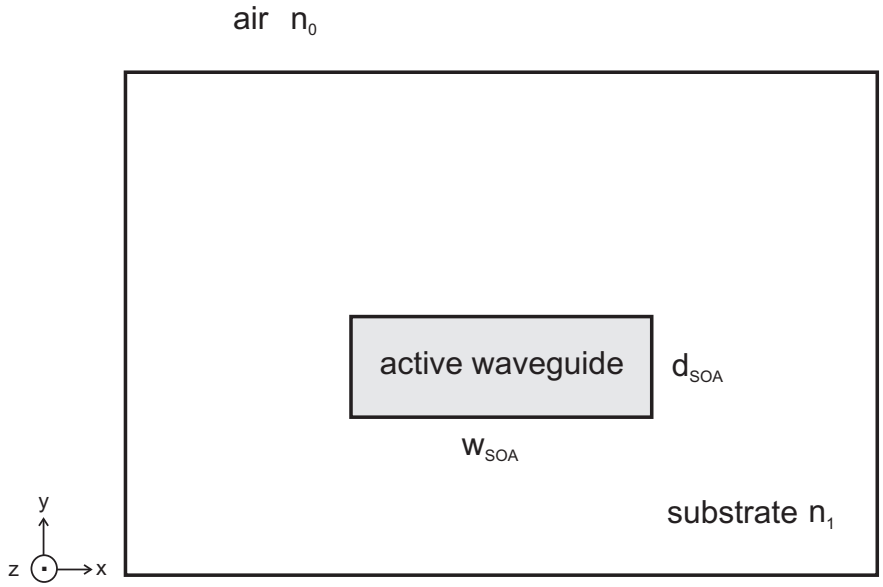

Figure 4.27 Cross section of a buried semiconductor optical amplifier.

Mode order	Γ_{TE}	Γ_{TM}	Γ_{TE} / Γ_{TM}	n_{eff}(TE)	n_{eff}(TM)
0	0.43	0.34	1.26	3.25	3.23

Table 4.4 Confinement factors and effective refractive indices of the active waveguide (SOA).

By using a tensile strained lattice, the band structure for the SOA can be changed differently in the lateral and in the vertical direction. The change leads to an enhanced gain in the vertical (TM) direction compared to the lateral direction (TE). Therefore, through a careful adjustment of the strain, not only the influence of the waveguide geometry but also the whole waveguide network can be compensated.
In Figure 4.28 and in Figure 4.29 the gain spectrum of with lattice matched and tensile strained active structure are depicted, respectively.

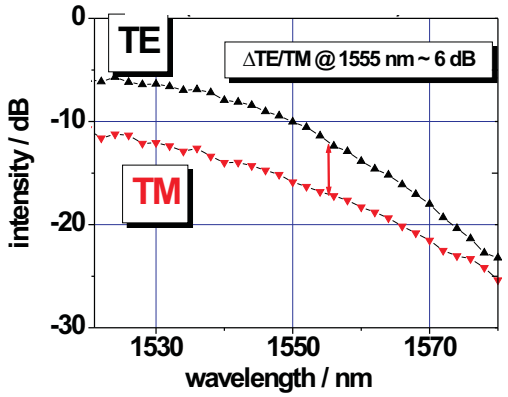

Figure 4.28 Gain spectrum of an integrated SOA with lattice matched active layer. Resulting polarization dependence at G_{max} about 6 dB.

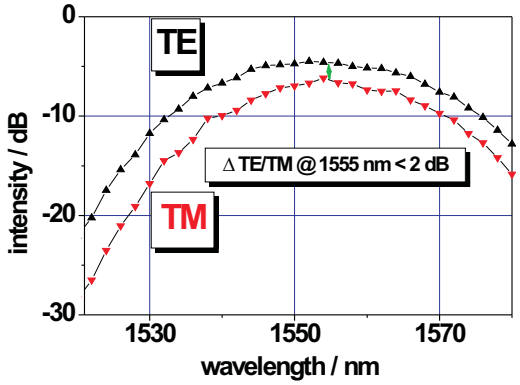

Figure 4.29 Gain spectrum of an integrated SOA with ca. 0.15% tensile strained active layer. Resulting polarization dependence at G_{max} < 2 dB.

Additionally, the data signal experiences the full gain of the SOAs compared to the GS-scheme as the gain maximum of the SOAs and of the data signal is within the same wavelength region.

4.10 Brief Summary of Polarization Insensitive Design of MZI

Photonic integration technology provides a wide range of basic components and possibilities. The main challenge is to combine this broad spectrum to functional devices regarding the requirements for system applications.
In this chapter the state of art of technology has been summarized which enabled the design of further optimized monolithically integrated Mach-Zehnder interferometer switch as for error-free 160 Gbit/s all-optical demultiplexing. The requested specifications for such a switch are as follows:

- Compactness
- Low loss
- Polarization insensitivity
- Compatibility within the communication system
- High speed

In the development of a polarization independent monolithically integrated Mach-Zehnder interferometer, there are at least three critical elements:

- The integrated SOAs are, in dependence of their structure, the most polarization sensitive elements in the MZI. Nevertheless, with careful adjustment of width and thickness of the layer stack and of the crystallographic strain within the active layer the polarization sensitivity can be reduced to or even less than the measurement limits around 0.4 dB, comprising a good reproducibility. Additionally the SOA can be dimensioned in such a way that a residual polarization sensitivity of the MZI could be compensated. Admittedly this can only be done for a given bias point of the interferometer.

- The fiber-chip coupling including anti reflection coating is polarization independent as long as the light is coupled perpendicular into/ out of the InP device. When angled facets are introduced for a further reduction of facet reflections, the AR coating layers have to be carefully adapted to the introduced off angle. As both polarizations show different behaviors of their reflection curves concerning depth and spectral location of the reflection minimum, a compromise for the coating parameters has to be found. Additionally, the reflection curves differ from each other for growing angles with increasing size. As a consequence the process tolerances for a polarization independent AR coating are

dramatically reduced for large off angles. For the monolithically integrated MZI an off angle around 7° on the chip (corresponding to ca. 23° in air) has been found to be sufficient for the reduction of facet reflections on one hand and a good technological reproducibility on the other hand.

- Concerning polarization dependence the MMI couplers seem to be the critical parts in the technology of the MZI. In principle, these devices are polarization independent, provided that the designed parameters can be reproduced exactly and only injection of the fundamental mode from the supplying waveguide can be assumed. Any deviation from these requirements leads to a non calculable behavior of the coupler concerning polarization and optical losses. The finite reproducibility of the technological processes will lead to small - not predictable - variations of the MZI behavior. On the other hand, the risk of coupling higher order modes into the MMI coupler can be minimized by the introduction of mode filters (bends with adequate radius) in front of the MMI coupler as done in the waveguide structure of the MZI.

Summarizing it can be said, that with the MZI structure and technology as used in this thesis there is a good feasibility of fabricating low loss, low polarization sensitive monolithically integrated interferometers.

5 Characterization of Mach-Zehnder Interferometer

In this chapter, the characterization in view of the ultrafast demultiplexing operation will be described. The evaluated results lead to revised designs and realizations of these devices with improved performance to obtain the first error-free 160 Gbit/s all-optical demultiplexer based on monolithically integrated MZI.
To demonstrate the reliable operation of an all-optical switch for demultiplexing application, a number of test measurements can be performed in the laboratory. Here, the basic features of the monolithically integrated MZI can be analyzed. This analysis is based predominantly on the static measurements of the MZI switch for the preselection issues.
The results are used to redesign the basic structure of the next generation of devices. With respect to the limited time, which can be used for the evaluation of each device generation and to the number of devices on each wafer, the following procedures are followed for the basic characterization, which are partially discussed in this chapter:

- After cleaving the wafer into bars, current (I) dependent voltage- (V/I) and power- (P/I) curves are measured on randomly chosen samples. With these measurements differences between the waveguide branches can be estimated (e.g. coupling ratio of MMI-couplers, symmetry of SOAs).

- Amplified spontaneous emission spectra are checked with an optical spectrum analyzer to obtain information on qualitative reflection effects as a function of the driving current of the SOAs.

- Transfer functions of the monolithically MZI are measured at the output ports of the MZI using a continuous wave (cw) signal and varying the current of SOAs. The switching contrast is obtained by coupling an additional cw control signal into the MZI.

5.1 Measurement Setup

Depending on the design of the mask set, more than 100 monolithically integrated MZI devices can be fabricated on a 2-inch InP wafer. To find those devices, which could be used in the demultiplexing experiments, various tests are needed. It is always a time- and material consuming process to separate the devices and mount them on sub-carriers to perform the preliminary tests. Therefore, a measurement setup as shown in Figure 5.1 has been used to realize a simple and rapid characterization of unmounted monolithically integrated MZI chips.

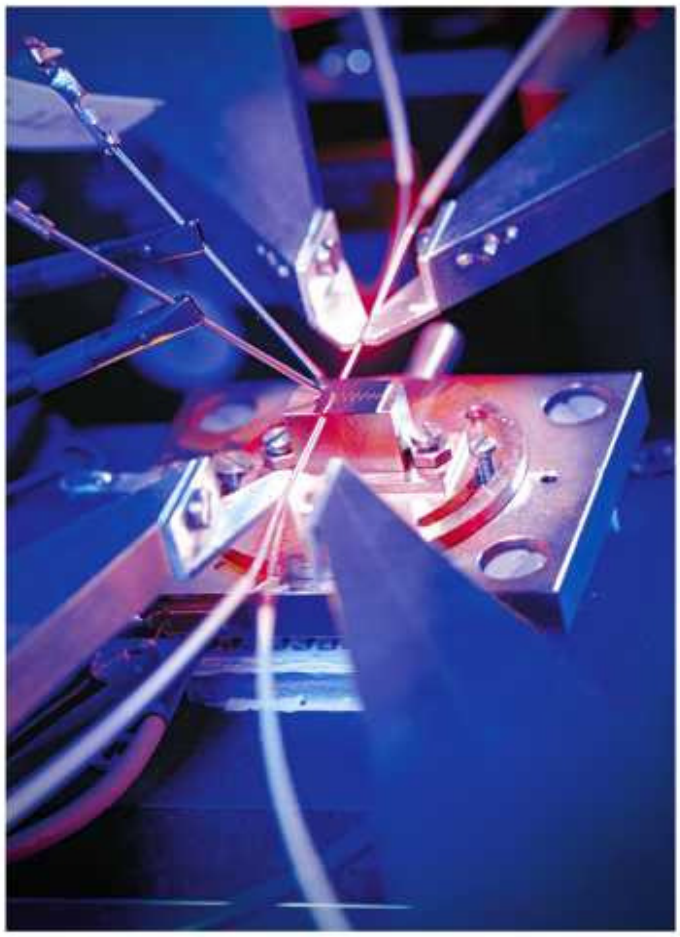

Figure 5.1 Photograph of the measurement setup for device testing [63].

Each of the four rotatable fiber holder arms is fixed on a separate xyz-micropositioner, which are placed twice on the left and on the right side of the sample holder, respectively. Thus, two input and two output tapered fibers can be adjusted independently in order to achieve a maximum of fiber-chip coupling

efficiency via piezoelectric controls. The device under test (DUT) itself is placed on a gold-coated copper block, which is mounted on a Peltier element. In combination with a temperature controller this allows stable chip temperatures in the range of 10°C to 30°C. The active elements of the monolithically integrated MZI, the SOAs, are biased through needles positioned on the metallized top p-contact. The n-contact is grounded via the sample holder. This mechanical measurement setup has the flexibility to be used for any new chip structure with up to four coupling ports (two on each side), and for any chip width. The tapered single mode fibers can be aligned to get the maximum ASE in case of a constant SOA current at the output ports of the MZI chip. The optical power can be measured via an optical power meter. This measurement setup has been used for analyzing the static behavior of the monolithically integrated MZI switch.

5.2 Symmetry Properties of Monolithically Integrated MZI

The all-optical switching by using the MZI relies on the symmetry features within the interferometric arrangement. The symmetry properties of the monolithically integrated switch can be analyzed by using a simple measurement. The measured ASE total power of the SOAs at different output ports can be used to estimate the symmetry properties. Here, the MMI-couplers (k_1, k_2, k_3 and k_4) and SOAs (SOA_1, SOA_2) of the monolithically integrated device can be compared also. Since the ASE propagates through the different paths to the ports of the MZI, significant deviations from the symmetry properties can be detected by comparing the power levels.

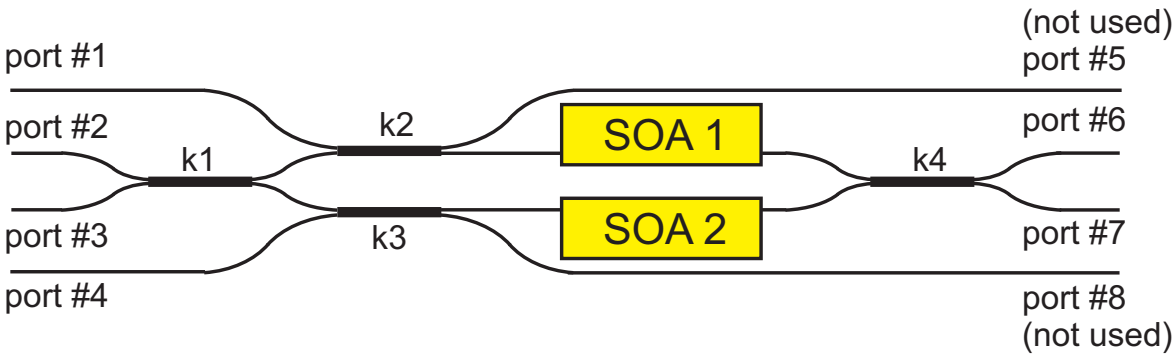

Figure 5.2 Symmetric Mach-Zehnder interferometer.

The total power of ASE (P_{ASE}) at each output port of the MZI can be measured at a constant SOA current. The representative values of MZI#1 (sec-

tion 9.5) are given in Table 5.1 [87], to demonstrate the deviations from the ideal case. It can be assumed, that the coupling efficiencies of the tapered fibers are comparable. In this example the SOAs are not identical, the MMI-couplers are not ideal, which can be tolerated in practice. The propagation paths are similar; please notice that the AR-coatings are done separately for each facet.

	P_{ASE} [dBm] at MZI port					
	port #1	port #2	port #3	port #4	port #6	port #7
I_{SOA1}=150 mA I_{SOA2}=0 mA	-23,4	-29,1	-28,6	-	-24,8	-23,7
I_{SOA1}=0 mA I_{SOA2}=150 mA	-	-27,0	-27,4	-21,4	-21,1	-22,7

Table 5.1 The total ASE power at output ports of the MZI#1 for constant SOA currents.

At the output ports #1 and #4 the ASE power can be measured only of one SOA. However, the ASE of both SOAs is detectable at the ports #2 and #3. By measuring the ASE of SOA1 at the ports #2 and #3, the coupling ratio of the MMI coupler k_1 can be assessed. After this, the coupling ratio is 47:53. The coupling ratio of an ideal 3 dB MMI coupler is 50:50. The deviation from the ideal coupling ratio amounts approximately 6%. This conclusion can be confirmed by measuring the ASE power of the second SOA at the same the output ports #2 and #3. The coupling ratio is not exactly determinable with such measurements, but they can be helpful to explaining the behavior of single components. The same can be examined also for the coupler k_4. The result corresponds to that one of the coupler k_1. Further, coupling behavior of k_2 and k_3 can be examined also.
The ASE of SOA_1 and SOA_2 are not identical, but they are in the same range of value. This result can be approved by comparing the ASE power of SOA_2 at the port #2, with the ASE power of SOA_1 at the port #3. The single components of the chip show some deviations from the ideal case. However, they are within the tolerance limits, since the functionality is given.

5.3 Analysis of ASE Spectrum

The ASE spectrum gives important hints regarding the reflections within the monolithically integrated MZI device. To investigate the spectral behavior of

the chip, the ASE power versus wavelength have been measured at a constant current value via an optical spectrum analyzer at the output ports of the MZI. As an example, the ASE spectra of MZI#10 (section 9.5) are depicted in the Figure 5.3. Here, the ASE spectra of SOA_1 are measured before and after the AR-coating at a constant current of I_{SOA1}=200 mA .
The AR-coated chip shows no lasing effects. Due to the effect of the AR-coating the ASE-peak is also shifted to the wavelength of 1510 nm.

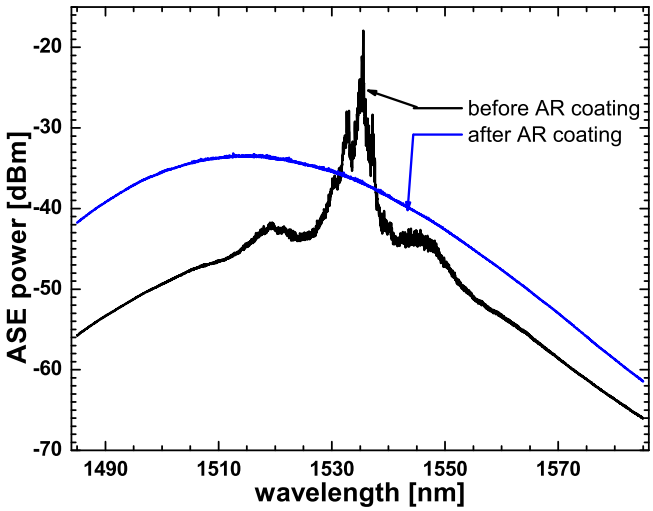

Figure 5.3 ASE spectra of integrated SOA_1 before and after the AR-coating of MZI#10.

5.4 PI-Characteristic of Integrated SOA

For investigation of the behavior of the monolithically integrated MZI in dependence of the SOA currents, the ASE power of the integrated SOAs have been measured at a wavelength of 1550 nm via an optical power meter while the current of each SOA is varied separately from 30 mA to 170 mA. Typical output power versus current curves within the integrated SOAs of MZI#2 (section 9.5) are given as an example in the Figure 5.4.
The optical power curves are parallel. The SOAs are similar. With this approach it is difficult to give a qualitative value of the gain of each SOA.

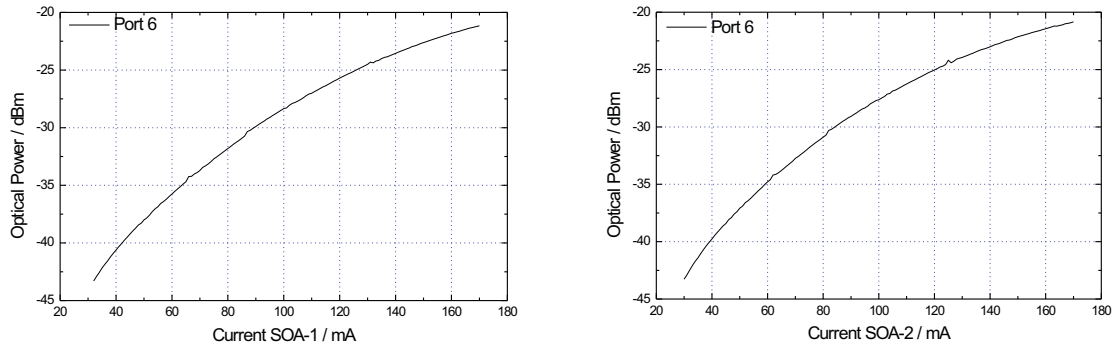

Figure 5.4 PI-characteristics of single integrated SOAs measured at different output ports of MZI#2 .

5.5 Gain Characteristics of Integrated GS-SOA

The optical gain is one of the important properties of the SOA based all-optical switch. The optical gain is provided by the injection of carriers into the active SOA region. The gain is defined by output optical power over optical input power (P_{OUT} / P_{IN}). Also the spectral dependence of the gain becomes important since the GS switching scheme is used.

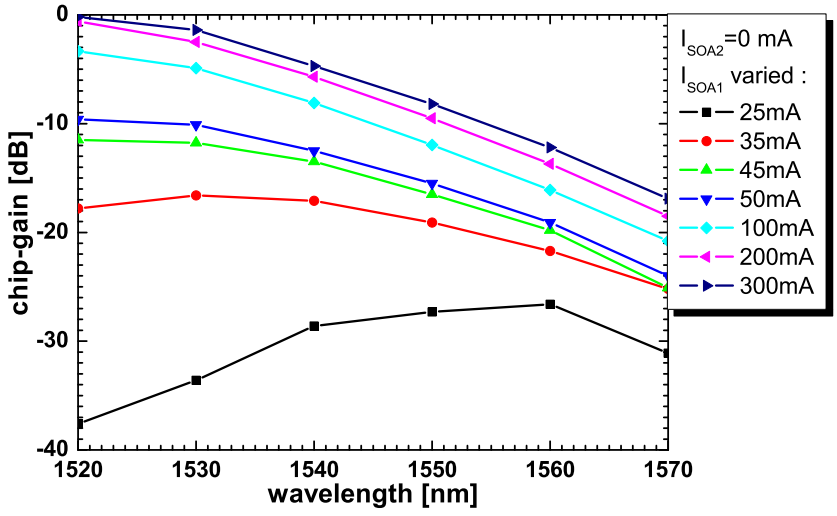

Figure 5.5 Wavelength dependent gain of integrated GS-SOA_1 (MZI#10) for different current values of I_{SOA1}.

As depicted in the Figure 5.5, the chip-gain of the monolithically integrated SOA_1 within MZI#10 (section 9.5) was measured for different values of SOA_1 current I_{SOA1}. Hereto, the wavelength of the injected cw optical input signal at port#6 was varied with a wavelength step of 10 nm between the wavelengths of 1520 nm and 1570 nm to cover the C-band operation. The optical power P_{IN} of the cw signal was kept constant at a power level of -4.4 dBm. The output power P_{OUT} was measured via an optical power meter at port#3.
The gain of the GS-SOA_1 can be also analyzed by varying the optical input power. In Figure 5.6 the chip-gain change on the cw probe input signal at the wavelength of 1550 nm is shown. The gain for the data signal is constant in the GS switching scheme.

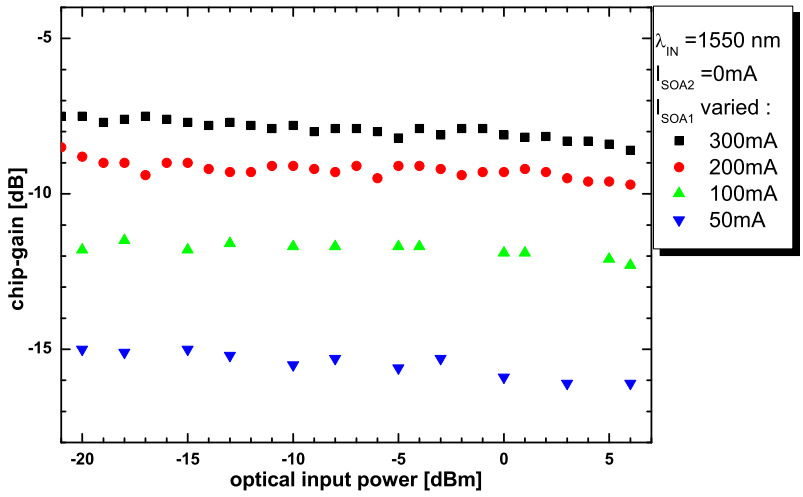

Figure 5.6 Gain curve of the integrated GS-SOA_1 (MZI#10) for different I_{SOA1} currents.

5.6 Polarization Dependence of Integrated GS-SOA

The polarization sensitivity is a criterion for the system performance of high-speed switches. Hereto, a cw probe signal at the wavelength of 1550 nm has been injected into the port #2 of the MZI (MZI#15, section 9.5) and the output power has been measured at the port #5 by scrambling the polarization of the cw input signal with an optical power P_{IN} of 5 dBm. As shown in Figure

5.7, the integrated GS-SOA$_2$ has a polarization dependence of about 1 dB in this operation.

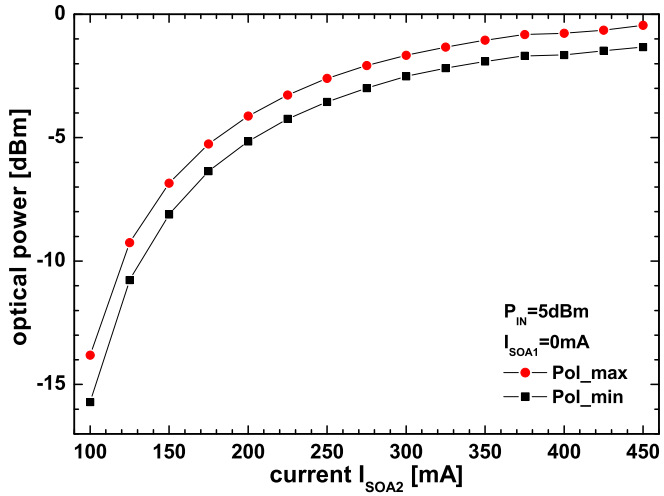

Figure 5.7 Polarization dependence of the integrated GS-SOA$_2$ (MZI#15).

5.7 Characteristics of Passive Waveguide

The characterization of the passive optical waveguide is fundamental for the design of photonic circuits and for the feedback to the processing technology. Therefore the measurements are performed for every processed wafer. Various methods for the measuring of the optical losses are known from the literature. However, the two main methods, which have been used for the characterization of the passive waveguides, are:

- The Fabry-Perot Resonance method [64], where Fabry-Perot resonance's in a chip are measured by varying the temperature by $\Delta T = 5$-$10°C$;
- The Cut-Back method [65] [66], of which the principle is to measure the loss of a waveguide at different chip lengths at a constant temperature.

Fabry-Perot Method

The Fabry-Perot resonance method is frequently used especially for the high refractive index waveguides (e.g. for InGaAsP, n=3.37, λ=1.25 µm) in addition to the conventional cut-back method. For low loss waveguides this

method is preferred over the conventional cutback method. With low intrinsic attenuation the coupling loss becomes more dominant leading to a poor contrast for the length dependent contribution. Also the sensitivity to the coupling conditions may degrade the measured data. The Fabry-Perot method depends on the ratio of the transmission minima and maxima and is therefore less sensitive to the coupling efficiency. If the reflectivity R of the end facets is known, the loss measurement can be performed in a single step. The experimental setup for the Fabry-Perot loss measurement is shown in the Figure 5.8. The DUT is a passive waveguide.

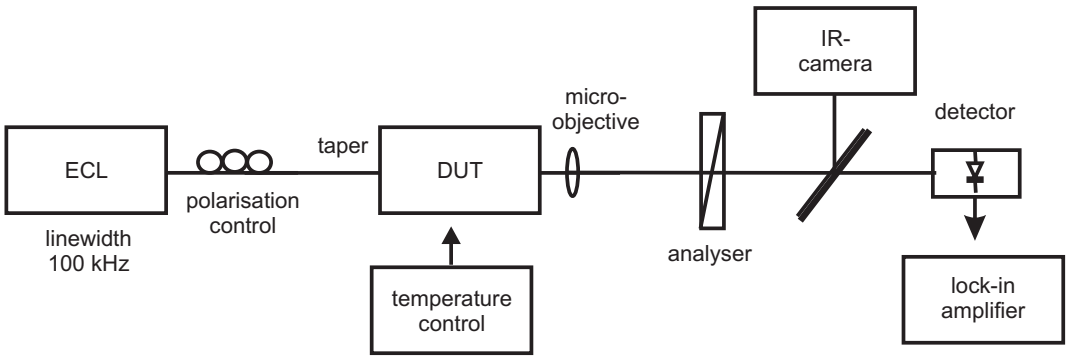

Figure 5.8 The experimental setup for Fabry-Perot loss measurements.

The maximum I_{max} and minimum I_{min} light intensities after the propagation of incident light with intensity I_0 through a waveguide of length L, loss coefficient α_{loss} and R the facet reflectivity for a Fabry-Perot resonator are given by [64]:

$$I_{max} = I_0 \frac{(1-R)^2 \exp(-\alpha_{loss} L)}{\{1-R \exp(-\alpha_{loss} L)\}^2} \qquad (5.1)$$

$$I_{min} = I_0 \frac{(1-R)^2 \exp(-\alpha_{loss} L)}{\{1+R \exp(-\alpha_{loss} L)\}^2} \qquad (5.2)$$

with $u = \frac{I_{min}}{I_{max}}$ the loss coefficient α_{loss} can be derived from

$$\alpha_{loss} = \frac{1}{L} \{\ln \frac{1-\sqrt{u}}{1+\sqrt{u}} + \ln R\} \qquad (5.3)$$

Values in dB/cm are obtained by multiplication $\bar{\alpha} = 4.34\,\alpha$ dB.

For a determination of the loss coefficient α_{loss}, the reflection coefficient R of the end facets has to be known. R can be measured with different sample lengths L by plotting the quantity of

$$\ln \frac{1-\sqrt{u}}{1+\sqrt{u}} \qquad (5.4)$$

over the length L [64]. The interception of the extrapolation with the ordinate axis results in -ln(R).
The Figure 5.9 shows a typical resonance curve obtained with this method. The fiber taper and the microscope objective are adjusted at a sample temperature of 20°C. The temperature scan is longer than necessary to show the defocusing effect due to the thermal walk-off of the sample holder for lower and higher temperatures. Although loss values are quite high for the Fabry-Perot method, the resonances are clearly resolved.

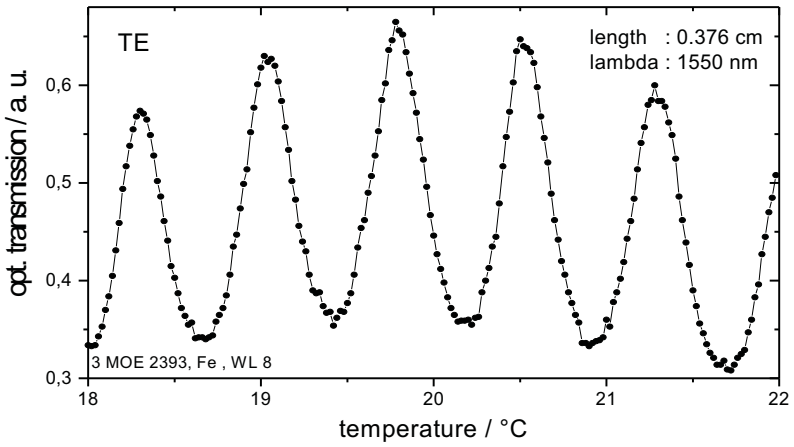

Figure 5.9 Transmitted optical intensity from waveguide resonator in the dependence of temperature.

The Figure 5.10 shows some derived loss values of the passive waveguides. Since a cut-back for determining R has not been performed for these first measurements a standard value of R = 0.3 was assumed. The dashed lines show the effect of ± 10% variations of R.

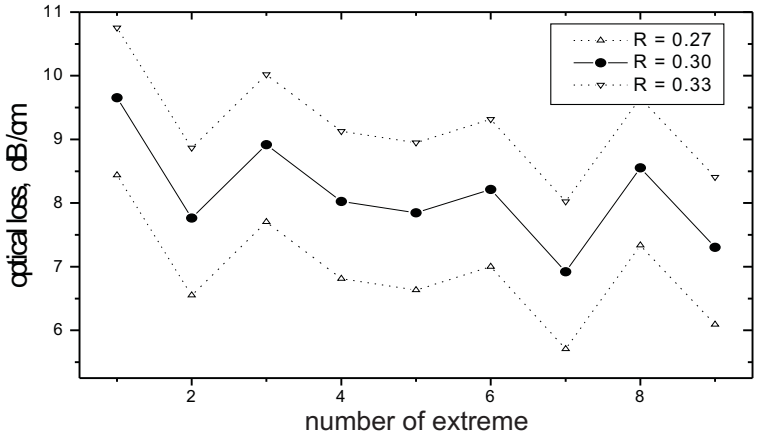

Figure 5.10 Calculated loss for adjacent intensity extremes in Figure 5.9.

Measurements on the waveguides revealed a difference in the loss parameters. The losses for TE and TM polarization states are 12 dB/cm and 15 dB/cm. The waveguides show higher attenuation for the TM-polarization.

Cut-Back Method

The cut-back method can be applied by using a similar experimental setup as described for the Fabry-Perot technique (Figure 5.8). There are only two differences: First, a conventional 1550 nm laser has to be used instead of an external cavity laser or a DFB-laser with narrow linewidth. Second, the device under test has to be kept at constant temperature.

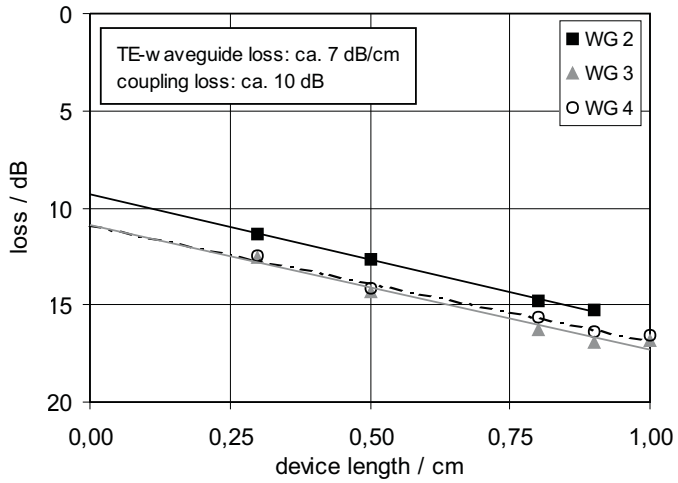

Figure 5.11 Optical losses measured by using the cut-back method.

The loss measurements have to be performed at different lengths of the chip; i.e. the device is cleaved (cut-back) several times in steps of 1 mm. The Figure 5.11 shows an example of the cut-back measurements for three waveguides. The slope of the straight line is a measure for the waveguide loss. The interception of the extrapolation with the y-axis is due to the fiber-chip coupling loss. The results obtained for both methods are comparable.

5.8 Current Induced Switching

To identify the static transfer function of the monolithically integrated MZI, the response to the current variations has been analyzed. Here, a cw light at a wavelength (λ_{cw}) is coupled from an external cavity laser (ECL) source into the port #3 as shown in the Figure 5.12. By assuming that the losses in the waveguides and MMI couplers are negligible, only 25% of the optical input power will arrive at each SOA and will be amplified during its propagation within the SOA. Here, the SOA current effects the amplification.

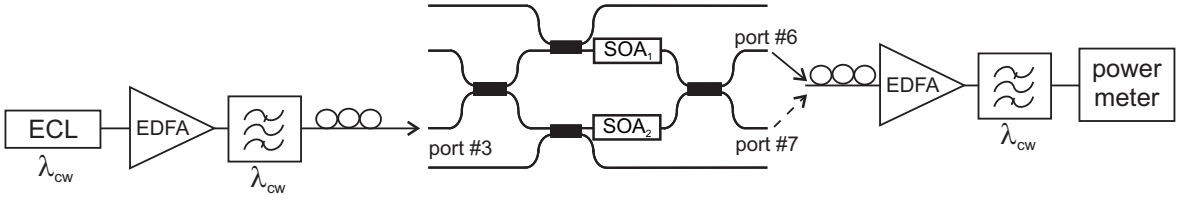

Figure 5.12 Experimental setup for current induced switching.

By varying the current in the SOA_2 (Figure 5.12) for a constant current value in the SOA_1, the steady-state of the interferometer (section 9.2) can be impaired, so that the injected light switches from one port to the other, due to the current induced gain and phase change within the SOA_2.
The output power was measured at ports #6 and #7 versus of the current in SOA_2.
First, the cw signal (10 dBm) at the wavelength of 1510 nm has been injected into the MZI#4 (section 9.5). At this wavelength the gain curve has its maximum (Figure 5.3). This measurement represents the conventional switching scheme. Then the wavelength of the cw light has been shifted to a longer wavelength to 1550 nm, to provide the GS switching scheme. The output signal intensities at bar- and cross output port have been analyzed in the dependence of the SOA_2 current, while the current for the SOA_1 was kept at 85 mA constant. The current induced switching results are depicted in the Figure 5.13 for the conventional switching scheme (λ_{cw}=1510 nm) and in the Figure 5.14 for the GS switching scheme (λ_{cw}=1550 nm).

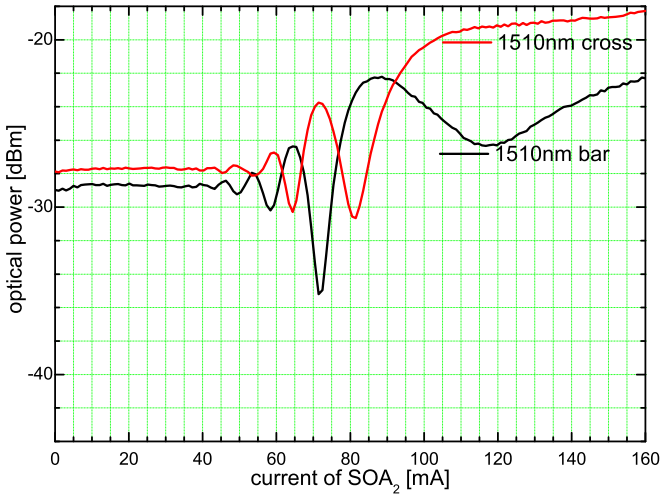

Figure 5.13 Measured transfer function for current induced switching, conventional scheme on a GS-MZI (MZI#4), (λ_{cw}=1510 nm).

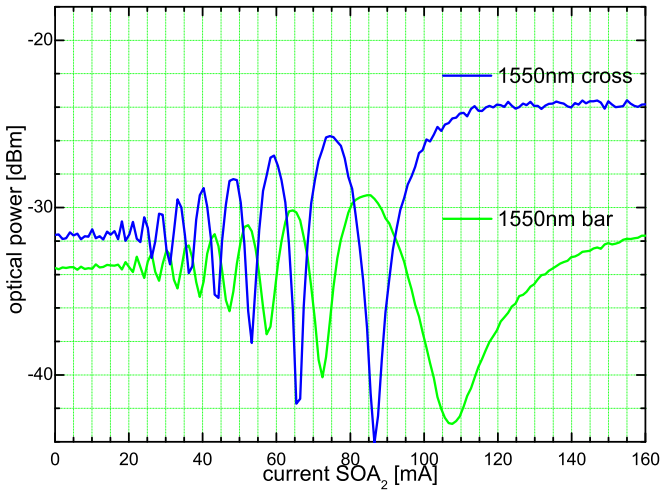

Figure 5.14 Measured transfer function for current induced switching, GS switching scheme on a GS-MZI (MZI#4), (λ_{cw}=1550 nm).

It can be clearly seen, that the current induced switching is more efficient in case of the GS switching scheme, regarding the contrast ratio and the phase shift on the output signal. The variation of the current between 0 mA to 160 mA causes a phase shift of 9π for the conventional switching scheme

(Figure 5.13) and a phase shift of 17π for the GS switching scheme (Figure 5.14). By using the same device, the influence of thermal effects on the comparison results has been excluded. Since the optical losses within the monolithically integrated MZI are high (~18 dB, estimated overall chip losses based on the measurement results presented in section 0), the power of the cw source which arrives the SOAs can be assumed about -8 dBm. So the saturation effect of the cw light in case of conventional switching scheme can be excluded. The GS switching scheme shows directly in comparison of the conventional scheme, a distinctly enhanced contrast ratio and higher phase shift efficiency.

5.9 Optically Induced Switching

Since the all-optical switching is addressed, the current induced switching process can only be used to understand the interferometric switching behavior. To analyze the effect of a second optical signal on the transfer function of the MZI, a second cw light at wavelength of $\lambda_{control}$ can be injected into the port #1 of the MZI for controlling the switching mechanism in the MZI device as shown in the Figure 5.15.

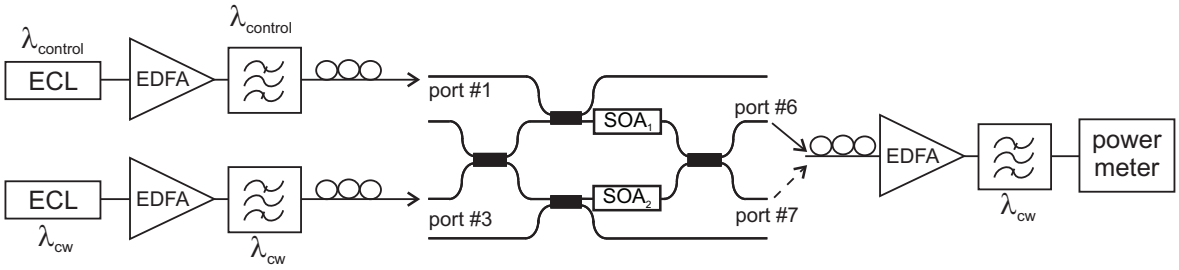

Figure 5.15 Experimental setup for optically induced switching.

An optical cw signal at the wavelength (λ_{cw}) 1550 nm has been injected into the input port #3 of the GS-MZI. The driving currents of both SOAs have been adjusted so that the optical signal at wavelength 1550 nm appears to the output port #7 (I_{SOA1}=100 mA, I_{SOA2}=74 mA). The interferometer has been debalanced then by injecting a variable optical control signal at the wavelength ($\lambda_{control}$) of 1510 nm into the control port of the SOA_1 (port #1). The output probe signal intensity versus the optical control input power is depicted in the Figure 5.16.
A phase shift of more than π, which means a complete switching of the probe signal from the port #7 to the port #6, has been achieved with a contrast ratio of 15 dB [40].

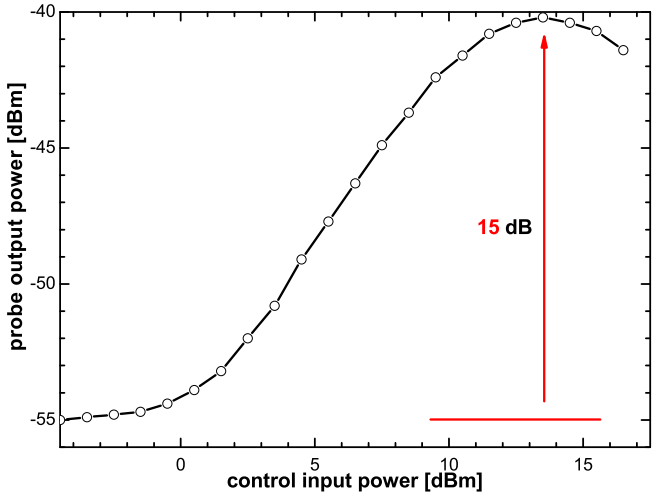

Figure 5.16 Optically induced switching in the GS-MZI (MZI#4).

5.10 Monitoring Method for MZI Dynamics

Essentially the switching properties of the all-optical Mach-Zehnder interferometer have to be investigated thoroughly under dynamic conditions. Here, a time resolution of ≤ 1 ps is needed, since the high-speed switching applications are aimed. Commercially available fast sampling oscilloscopes do not provide the required time resolution at high speed. Moreover, streak cameras cannot measure the on/off contrast ratios accurately. Therefore the pump-probe experiments [41] are used to study the monolithically integrated MZI switching properties under dynamic conditions.
The key components for the pump-probe technique are two ps-pulse sources, which enable the time resolved analysis at a high repetition rate. A tunable mode-locked laser (TMLL) [67] triggered with an external frequency generator provides the required ps-pulses with typical widths of 1 to 2 ps and with a sech^2 pulse shape (Figure 5.17) [41]. The repetition rate of the pulses can be varied between 2 GHz and 10 GHz, and the emission wavelength of this semiconductor-based laser is also tunable within the C-band. The principle of the pump-probe technique relies on the measurement of the power changes on the probe pulse, which propagates trough the device under test and experiences the refractive index changes within the test device. A high power pulse can evoke the refractive index change within the DUT. The influence of the

probe pulse on the test device is assumed to be negligible, since the probe optical power low enough.

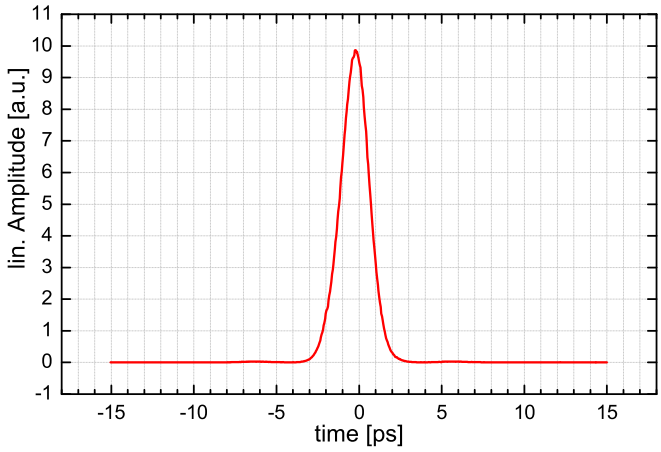

Figure 5.17 The measured autocorrelation of typical TMLL pulses after [41].

There are two basic configurations, which allows either static or dynamic monitoring of the intensity modulation of the probe pulses. Since the pulse sources are triggered with the same frequency (f_{probe}=f_{pump}), the wavelength spectrum of the probe signal can be monitored statically by using an optical spectrum analyzer as show in the principle setup for static pump-probe measurements (Figure 5.18).

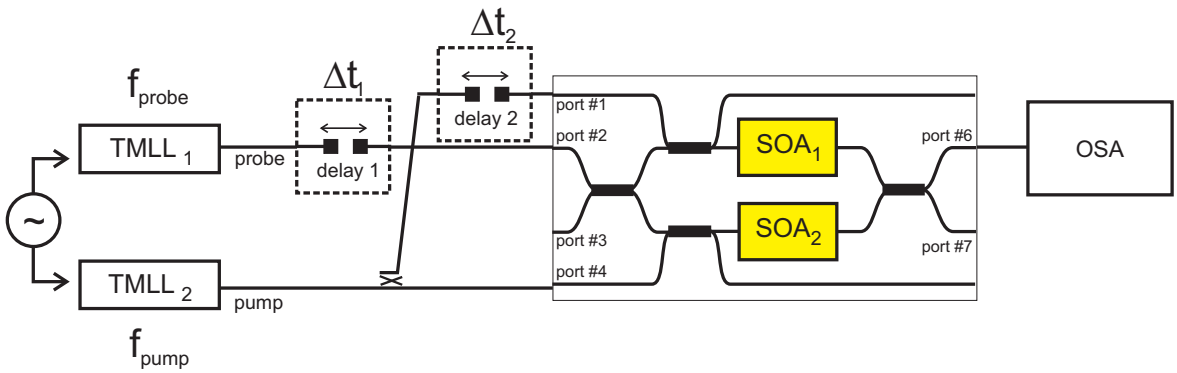

Figure 5.18 Principle setup of static pump-probe measurements.

An external delay line delay1 enables the determination of the temporal time delay Δt_1 ($\Delta\tau$) between the probe pulses and pump pulses. The second external delay determines the relative delay Δt_2 between the two control pulse streams, respectively. By varying the delay Δt_1 of the probe pulses with respect to the pump pulses, the power change of the probe signal can be moni-

tored as a function of the temporal delay Δt_1, so the dynamic response of the DUT can be resolved within the whole repetition period $T=1/f_{pump}=1/f_{probe}$.

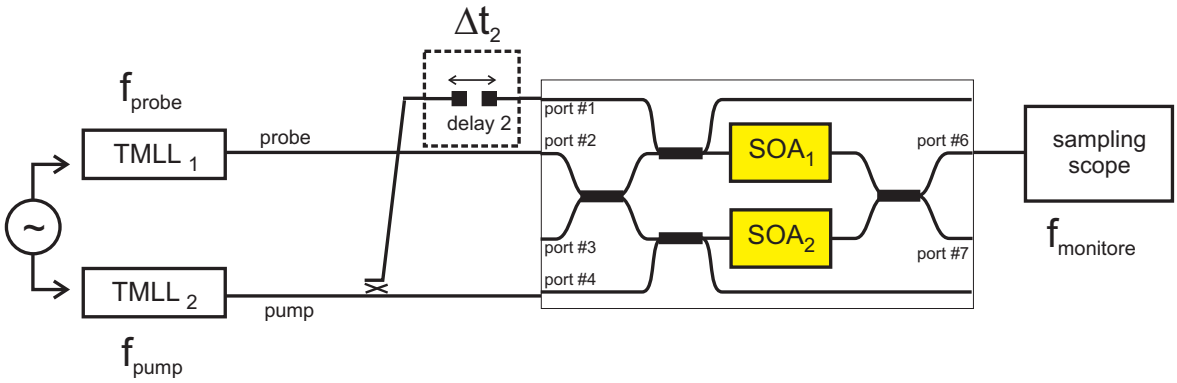

Figure 5.19 Principle setup of dynamic pump-probe measurements.

The main difference in the dynamic monitoring configuration (Figure 5.19) is, that the trigger frequencies of the probe and pump sources are not equal. The repetition frequency of probe pulses f_{probe} is slightly different from the repetition frequency of the pump pulses f_{pump}. As a result, the temporal time delay of the probe pulses changes with respect to the pump pulses in every period of T_{pump} and scans the influence of the pump signal with a frequency $f_{monitor}=f_{pump}-f_{probe}$. By choosing the monitoring frequency small enough ($\leq$ 10 MHz) the power change of the probe signal can be detected by using a slow photodiode and a conventional sampling scope.

5.11 Operation Conditions for Dynamic Analysis

Depending on the operation conditions and on the selected input and output ports, several dynamic features of the MZI and of the integrated SOAs can be measured by using the experimental setups as given in the section 0. The dynamic features, which can be measured by using the pump-probe technique, are listed below:

- Switching window of MZI (sw)
- Saturated gain response of integrated SOA_1 (gr1)
- Saturated gain response of integrated SOA_2 (gr2)
- 'Hidden' phase response of integrated SOA_1 (pr1)
- 'Hidden' phase response of integrated SOA_2 (pr2)
- Unsaturated gain response of integrated SOA_1 (g01)
- Unsaturated gain response of integrated SOA_2 (g02)

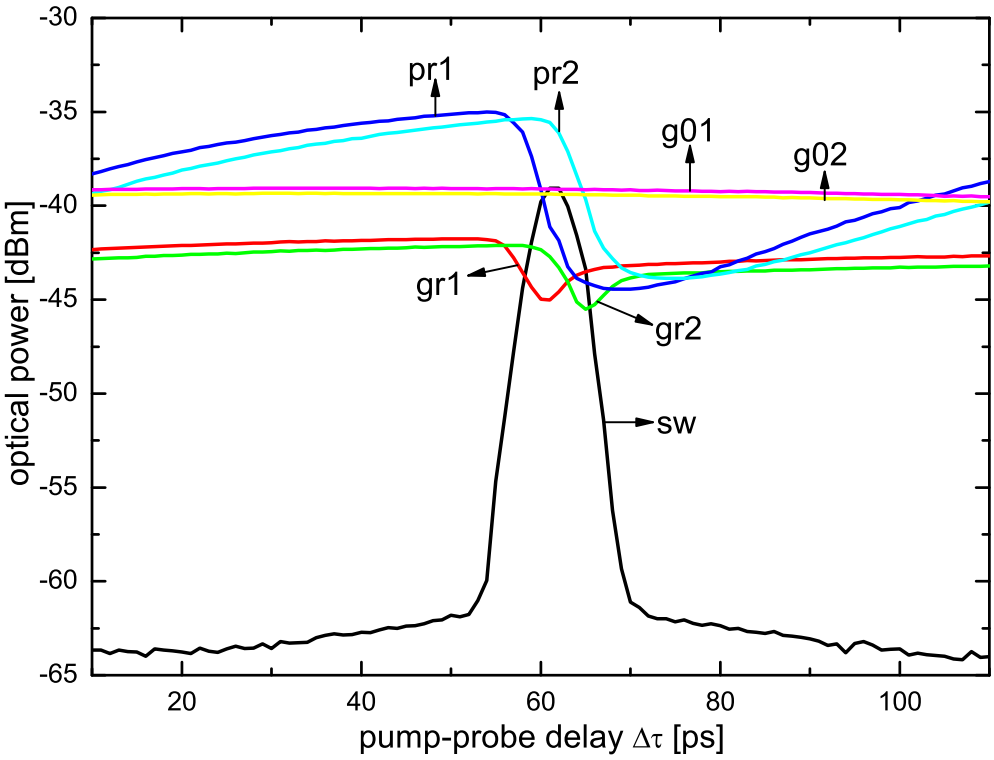

Figure 5.20 Curves representing the measurement results of monitored dynamic features within the monolithically integrated MZI.

The curves representing these measurement results are depicted in the Figure 5.20. For example, the gain response of SOA_1 can be measured by injecting the pump signal into the port #1 and the probe signal into the port #2. If only the SOA_1 is on, the monitored probe signal at the output port #6 corresponds to the saturated gain response of the SOA_1.
The gain recovery and phase response of each SOA and the switching window of the MZI are important dynamic features. In the Table 5.2 the operation conditions for each feature are summarized [68], which will be used for further analysis of gain (section 5.12) and phase response (section 5.13) of the integrated GS-SOA, relative phase shift of GS-MZI (section 5.14) and switching windows of GS-MZI (section 5.15). Here, a GS-MZI MZI#7 (section 9.5) with gain maximum of SOAs at 1530 nm is used to analyze the dynamic features. The wavelength of the pump signal ($TMLL_2$) is at 1535 nm.
The monitored MZI dynamics can be explained also theoretically. The summarized dynamic features in Table 5.2 and their measurement conditions can be extracted from the transfer function of the MZI (section 9.2).

	Dynamic Feature	$pump_1$ port #1	probe port #2 or #3	$pump_2$ port #4	port #6 or #7	I_{SOA1}	I_{SOA2}	Eq.
sw	Switching window of MZI	15.9 dBm	1.3 dBm	17 dBm	probe output	252 mA	296 mA	(5.5)
gr1	Gain response of SOA_1	15.9 dBm	1.3 dBm	not used	probe output	252 mA	off	(5.6)
gr2	Gain response of SOA_2	not used	1.3 dBm	17 dBm	probe output	off	296 mA	
pr1	'Hidden' phase response of SOA_1	15.9 dBm	1.3 dBm	not used	probe output	252 mA	296 mA	(5.7)
pr2	'Hidden' phase response of SOA_2	not used	1.3 dBm	17 dBm	probe output	252 mA	296 mA	
g01	Gain response of unsaturated SOA_1	not used	1.3 dBm	not used	probe output	252 mA	off	
g02	Gain response of unsaturated SOA_2	not used	1.3 dBm	not used	probe output	off	296 mA	(5.8)

Table 5.2 Dynamic features and their measurement conditions.

5.12 Gain Response of Integrated GS-SOA

The gain response (10 GHz) of the GS-SOA within the GS-MZI has been investigated by varying the wavelength of the probe signal ($TMLL_1$) from 1550 nm to 1570 nm and using the measurement conditions listed in the Table 5.2 and the experimental setup described in section 5.10. This analysis corresponds to the equation (section 9.2):

$$H_{D_1} = \frac{P_{D_1}}{P_{A_1}} = \left| \left[\frac{D_1}{A_1} \right]_{A_2=0} \right|^2 = \frac{1}{4} G_1 + \frac{1}{4} G_2 - \frac{1}{2} \sqrt{G_1 G_2} \cos\Delta\Phi \qquad (5.5)$$

under the condition that the second SOA is not used ($G_2 = 0$) and the transfer function can be written as:

$$H_{gain\ response} = \left[H_{D_1} \right]_{G_2=0} = \frac{1}{4} G_1 \qquad (5.6)$$

The measured gain dynamics for different wavelengths of the probe signal are depicted in Figure 5.21.

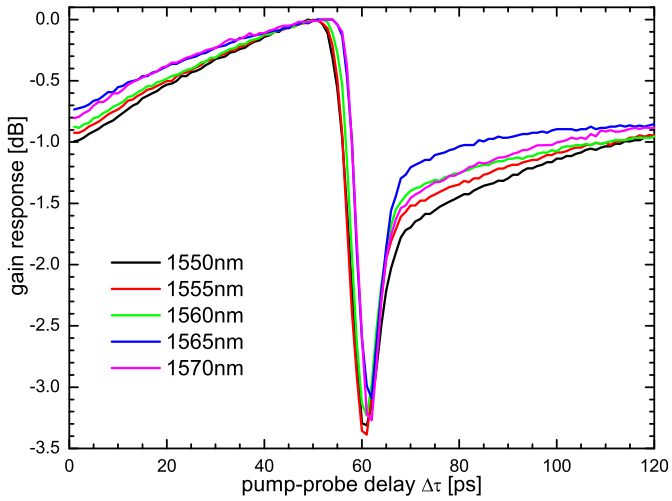

Figure 5.21 Gain dynamics of the GS-SOA in dependence of probe signal wavelength (gain maximum at 1530 nm).

No significant differences could be observed in the gain dynamics of SOA_1 for the conventional (λ_{probe}=1550 nm) and GS (λ_{probe}=1570 nm) switching schemes. The saturation of the gain decrease is in both schemes about 3 dB.

5.13 Phase Response of Integrated GS-SOA

The phase dynamics Φ of the integrated SOA cannot be directly measured. This can be evaluated from different measurements (Table 5.2). The 'hidden' phase response can be expressed after equation (5.5) as follows:

$$\begin{aligned} H_{hiddenphase} &= [H_{D_1}]_{pump_2=0} \\ &= \frac{1}{4}G_1 + \frac{1}{4}G_{2,0} - \frac{1}{2}\sqrt{G_1 G_{2,0}}\cos(\Phi_1 - \Phi_{2,0}) \end{aligned} \qquad (5.7)$$

Here, the unsaturated gain response of SOA_2 ($G_{2,0}$) can be measured corresponding to the following equation:

$$H_{unsaturated\ gain\ response} = [H_{D_1}]_{pump_1=0,\, pump_2=0, G_1=0} = \frac{1}{4} G_{2,0} \qquad (5.8)$$

The measured 'hidden' phase dynamics for different wavelengths of the probe signal are depicted in the Figure 5.22.

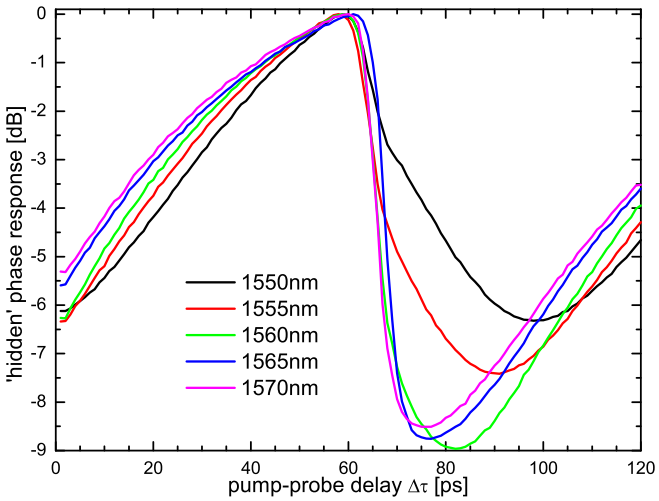

Figure 5.22 Phase response of the integrated GS- SOAs (gain maximum at 1530 nm).

The change in the hidden phase response of the integrated GS-SOA in case of GS switching scheme is about 3 dB larger than in the case of conventional scheme.

5.14 Relative Phase Shift within the GS-MZI

The relative phase change $\Delta\Phi$ is essential for interferometric switching. The dependence of $\cos\Delta\Phi$ and $\Delta\Phi$ on the operating wavelength has been analyzed for the GS switching scheme. First, $\cos\Delta\Phi$ is calculated by using the equation (5.5) and the measurement results sw, gr1 and gr2 (Table 5.2, Figure 5.20), corresponding to the following equation:

$$\cos\Delta\Phi = -\frac{H_{D_1} - G_1 - G_2}{2\sqrt{G_1 G_2}} \qquad (5.9)$$

Then the relative phase change ΔΦ is calculated The results of wavelength dependent cosΔΦ and ΔΦ are depicted in Figure 5.23 and Figure 5.24, respectively.

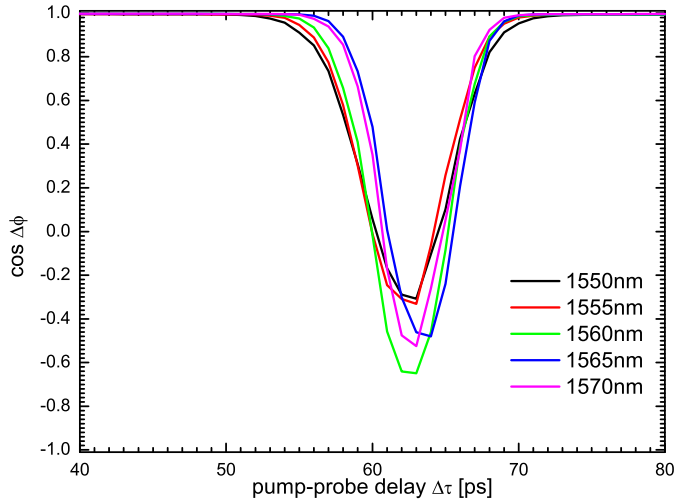

Figure 5.23 Calculated cosΔΦ of GS-MZI (gain maximum at 1530 nm).

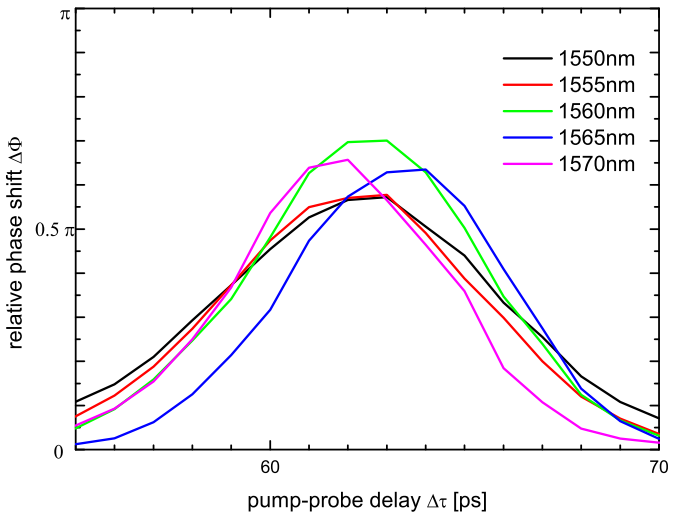

Figure 5.24 Calculated ΔΦ of GS-MZI (gain maximum at 1530 nm).

The relative phase change is improved by introducing the GS scheme about 15%.

5.15 Switching Windows of GS-MZI

In the previous sections the dynamics of integrated GS-SOA were discussed. The dynamic behavior of the GS-MZI is determined by their performances, because the SOAs are the only nonlinear elements within the MZI. The dynamic response of the monolithically integrated GS-MZI has been investigated by the pump probe measurements as described in the section 0 by using the measurement conditions in the Table 5.2. The wavelength of the probe signal relative to the gain maximum of the SOA and to the pump signal defines the switching scheme. The influence of the probe wavelength on the switching windows of the GS-MZI have been analyzed by varying the probe wavelength from 1550 nm to 1570 nm by keeping the operating conditions constant. This corresponds to the equation (5.5). The results are depicted in the Figure 5.25. The contrast of the switching windows increases by shifting the probe signal towards the longer wavelengths. This dynamic investigation confirms the static current induced switching measurements. This behavior can be understood by the dynamic response of the GS-SOA.

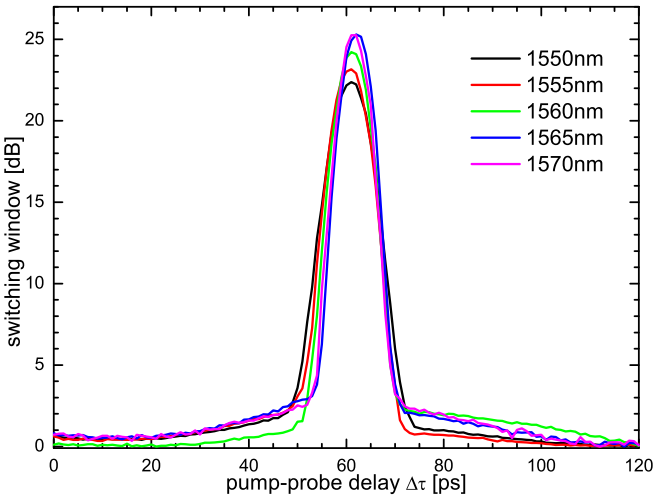

Figure 5.25 Measured switching windows of GS-MZI (gain maximum at 1530 nm).

The contrast of the switching windows increases by shifting the probe signal towards the longer wavelengths. Taking into account the similar gain responses for the conventional and GS switching schemes makes clear, that the enhanced overall switching performance [69] of the monolithically integrated GS-MZI is achieved by the improvement of the phase response in the inte-

grated GS-SOA compared to the conventional scheme. The results of the discussed measurements on the switching windows of the monolithically integrated GS-MZIs and the gain-/phase dynamics of the integrated SOAs are summarized in the Table 5.3 [68]. The GS switching scheme provides an enhanced switching contrast of 25.3 dB compared to the conventional scheme. The relative phase change used for the interferometric switching is improved by introducing the GS scheme by about 15%.

λ_{probe} [nm]	1550	1555	1560	1565	1570
Switching scheme	Conv.	GS	GS	GS	GS
Gain decrease in the gain response of SOA [dB]	3.3	3.4	3.2	3.1	3.3
Gain decrease in the 'hidden' phase response of SOA [dB]	6.3	7.4	9.0	8.7	8.5
$\cos\Delta\Phi$	-0.3	-0.33	-0.64	-0.46	-0.52
$\Delta\Phi$	0.57π	0.57π	0.7π	0.63π	0.65π

Table 5.3 Results of dynamic analysis.

5.16 Parameters of the Switching Window

The switching windows representing the MZI dynamics have been analyzed regarding the switching parameters in terms of the ultrafast all-optical demultiplexing. In the Figure 5.26 an exemplarily switching window of the monolithically integrated GS-MZI is depicted.

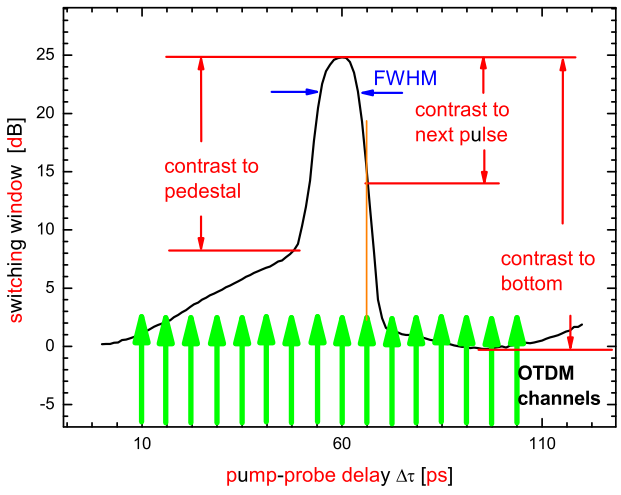

Figure 5.26 Parameters of the switching window.

To compare the switching windows and analyze the switching performance of the MZI, the parameters of the switching windows have to be extracted. These parameters describe the width and the depth of the switching window.
The width of the switching window can be expressed by the full width at half maximum (FWHM). Depending on the bit rate of the data stream, there is a maximum width, which can be tolerated for a successful switching performance. The maximum width is equal to the bit period of the data signal. If the FWHM is larger than this maximum, adjacent OTDM channels will be also switched. The minimum width of the switching window depends on the pulse width of data signal stream. If the switching window is narrow than the data pulse width, it leads to reshaping of this data pulse. This kind of reshaping is required for the synchronous modulation type 3R regeneration [70], but for all-optical demultiplexing this leads to the degradation of the transmission system.
For the definition of the switching window depth, as shown in the Figure 5.26 there are three possible references, which can be used to calculate the contrast ratio:

- The position of the next/adjacent pulse
- The pedestal of the switching window
- The bottom of the switching window

Depending on the selection of the reference level, the value for the contrast ratio changes in terms of the shape of the switching window. To take the position of the next OTDM channel as a reference is the most convenient method for the definition of the switching depth. Because, this elucidates the suppression of other channels, since demultiplexing application is of the interest.
Indeed, the best methods to analyze and assess the switching performance of the MZI switch are bit error-rate or Q-factor measurements on the demultiplexed signal. Usually these measurements are used to monitor the system performance.
Recently, a new aspect had been introduced to analyze the switching windows, the so-called integrated contrast ratio (ICR) [71]. The ICR defines the ratio between the demultiplexed OTDM channel and transmitted OTDM channels.
The switching windows of GS-MZI for different probe signal wavelengths (Figure 5.25), which were discussed in section 5.15, have been analyzed based on the described parameters such as contrast, FWHM and ICR and summarized in the Table 5.4.

λ_{probe} [nm]	1550	1555	1560	1565	1570
Switching scheme	Conv.	GS	GS	GS	GS
FWHM [ps]	7.5	6.3	6.1	5.6	5.4
Contrast to pedestal [dB]	20.3	19.7	22	22.2	21.9
Contrast to bottom [dB]	22.4	22.3	24.2	25.2	25.7
ICR for 80 Gbit/s [dB]	12.4	12.5	14.7	15.5	15.6
ICR for 160 Gbit/s [dB]	3.4	5.6	7.1	8.2	9.12

Table 5.4 Analysis of switching windows depicted in Figure 5.25.

The performance of the switching window changes depending on the switching schemes, the specifications of the pump and probe signal and generally on the operation conditions. The following variables actuate the switching dynamics of the monolithically integrated MZI:

- Driving currents of the SOAs
- Power levels of pump and probe signals
- Pulse shapes of pump and probe signals
- Repetition rates of pump and probe signals
- Wavelengths of pump and probe signals
- Delay between the pump pulse streams

Regarding the all-optical 160 to 10 Gbit/s demultiplexing application the following parameters and their effects on the switching performance of the monolithically integrated MZI have been investigated:

- External delay Δt_2 between the pump pulse streams
- Wavelength of the probe signal
- Power level of the probe signal
- Pulse widths of the pump pulses

The external delay Δt_2 between the pump pulse streams (Figure 5.19) changes primarily the width of the switching window and affects secondarily the shape of this. To analyze the influence of the external delay on the switching dynamics of the MZI, the delay has been varied while keeping all the other conditions constant. The repetition rate of pump pulses was 10 GHz. The results are summarized in the Figure 5.27.
As depicted, the smallest switching window has been achieved with a FWHM of 3 ps, which is required for demultiplexing of a 320 Gbit/s data stream. The largest switching window has the FWHM of more than 20 ps, which can be used for 40 Gbit/s data stream. The maximum achieved contrast ratio amounts

27 dB. A switching window with 22 dB contrast ratio and with FWHM of 6 ps have been used for 160 to 10 Gbit/s all-optical demultiplexing. The symmetric Mach-Zehnder interferometer is a bit-rate flexible device.

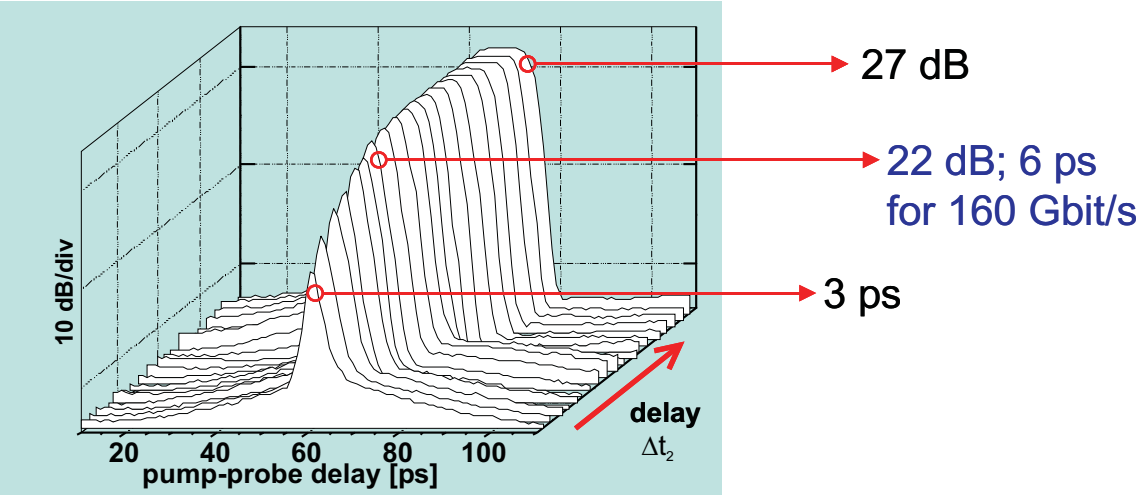

Figure 5.27 Switching windows with different widths.

As an example, the dependence of the switching window width on the external delay Δt_2 is depicted in the Figure 5.28. The switching window width increases by increasing the physical delay nearly linear; the minor deviations are due to the mechanical inaccuracy of the delay line.

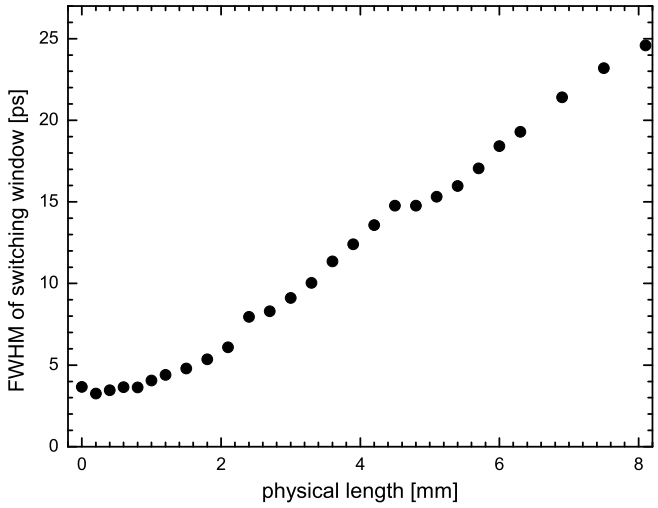

Figure 5.28 Dependence of the switching window on the external delay.

The corresponding contrast ratios of the switching windows given in the Figure 5.28 are shown in the Figure 5.29. Here, the contrast ratios have been

measured by taking the bottom of the switching window as a reference. First, by broadening the switching window, the contrast increases. For very broad switching windows the contrast begins to decrease because of the mismatch between SOA dynamics.

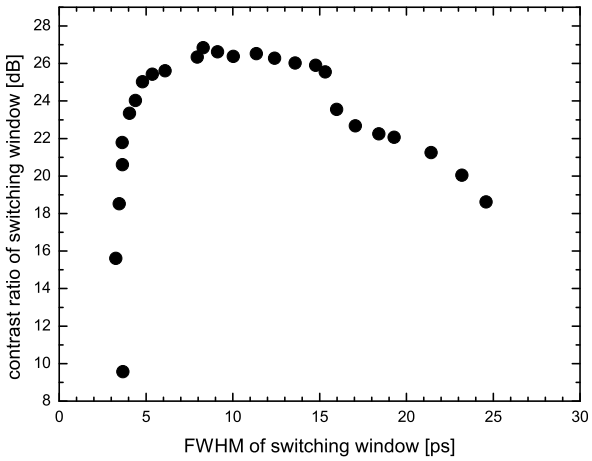

Figure 5.29 Contrast ratio of the switching windows with their FWHM give in the Figure 5.28.

In an OTDM switching node, there are local variables like SOA currents, and specifications of the control signal. These can be adjusted to perform a sufficient switching. Hereto, an online monitoring system with an automated feedback is needed to analyze the switching performance and adjust the local parameters, which is not the topic of this thesis. However, the power level of the data signal cannot be controlled in the switching node. The switching dynamics of the MZI should not be influenced by the changes within the data signal. There are three possible changes regarding the data signal: its polarization, its power level and the position of each data pulse (jitter). The polarization dependence had been analyzed during the static characterizations (Figure 5.7); polarization sensitivity less than 1 dB has been shown. Since several OTDM sources are used, the power level of the data signal can change depending its origin and its polarization. Therefore, the dependence of the switching response of the MZI on the power level fluctuations of the probe signal becomes important. To avoid the fluctuations in the power level of different OTDM channels, an inline power equalizer is needed. This can be realized by using the novel ultralong SOA [72], which is also not the topic of this thesis. The influence of the data signal intensity on the switching has been investigated by varying the probe signal input power of the MZI switch between -25 dBm and +10 dBm. Here, the switching window specifications have been analyzed. The analyzed switching windows are depicted in the Figure 5.30.

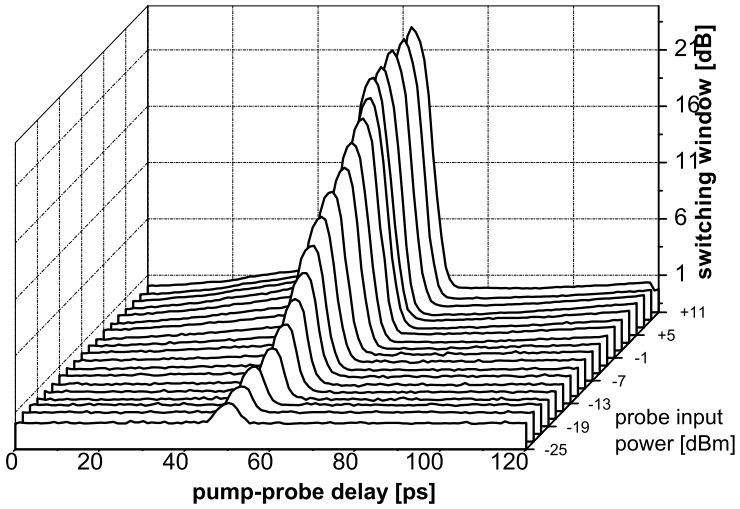

Figure 5.30 Probe intensity dependence of the MZI switching dynamics.

As shown in the Figure 5.31 the FWHM of the switching windows is not influenced by the probe signal power above -15 dBm input power. The contrast of the switching window changes linearly over a wide range.

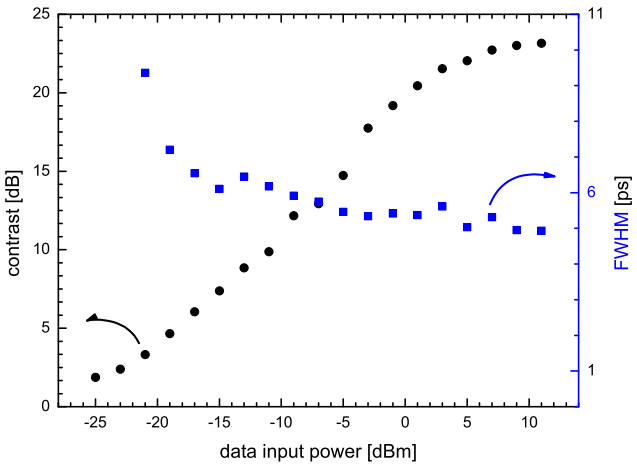

Figure 5.31 Switching window specifications by varying the probe signal power.

By comparing the switched signal intensity and the input signal intensity, the expected linearity over a range of nearly 20 dB can be shown (Figure 5.32). The linearity is limited by the gain saturation effects for high data input power and by the ASE of SOAs for low data input power levels, where the signal to noise ratio becomes low. With its linearity, the all-optical MZI switch fulfills the one of the important requirements for all-optical sampling.

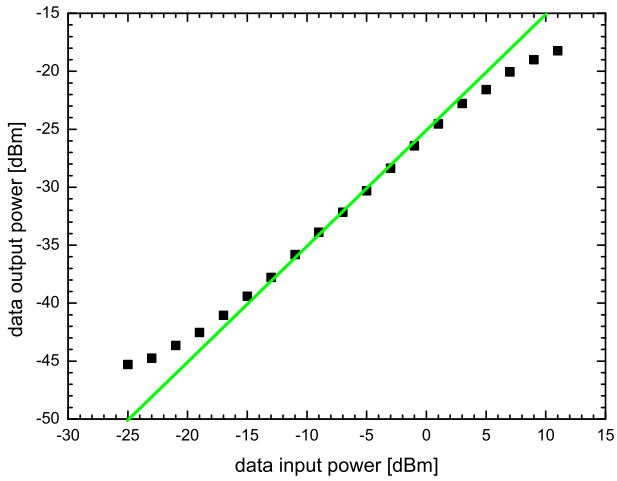

Figure 5.32 Linear switching dynamics of MZI.

To investigate the influence of the optical control pulses and the external optical delay (Δt_2) on the switching performance, the VPIcomponentMaker^{TM} [73] is used for simulations. The 3 ps pulses of sech^2-shape at 160 Gbit/s are used as data stream. Here, the contrast ratio of the demultiplexed optical data signal have been investigated for different widths (FWHM) of the control pulses (sech^2) and for different widths of the switching windows. The Figure 5.33 depicts the simulation results for 160 to 10 Gbit/s demultiplexing. The extinction ration degrades by 10 dB with increased width of the control pulse from 0.5 ps to 3 ps. This demonstrates the strong enhancement by very short pulses for demultiplexing processes of the MZI type demultiplexer.

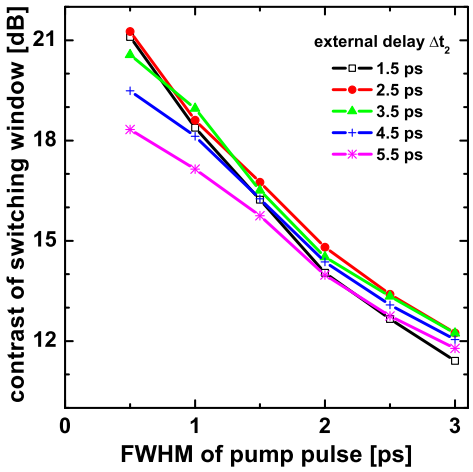

Figure 5.33 Contrast ratio for different widths of control pulses (sech^2) and for different widths of the switching windows.

6 All-Optical Demultiplexing Experiments

In this chapter, the results of all-optical demultiplexing system experiments represent the development of monolithically integrated Mach-Zehnder interferometer towards higher bit-rate operation.
For the realization of an ultrafast all-optical demultiplexer as a first step symmetric MZIs have been used for error-free 80 to 10 Gbit/s all-optical demultiplexing.
The main goal of this research work was to develop a 160 Gbit/s all-optical demultiplexer. By using the novel GS switching scheme the first error-free monolithically integrated 160 Gbit/s all-optical demultiplexer has been realized and the system performance has been successfully demonstrated.

6.1 Symmetric MZI for All-Optical Demultiplexing of 80 Gbit/s Signals

For all-optical demultiplexing at 80 Gbit/s both types of monolithically integrated symmetric Mach-Zehnder interferometers (Figure 6.1) have been used:

- Conventional Mach-Zehnder interferometer (MZI#5)
- GS Mach-Zehnder interferometer (MZI#6)

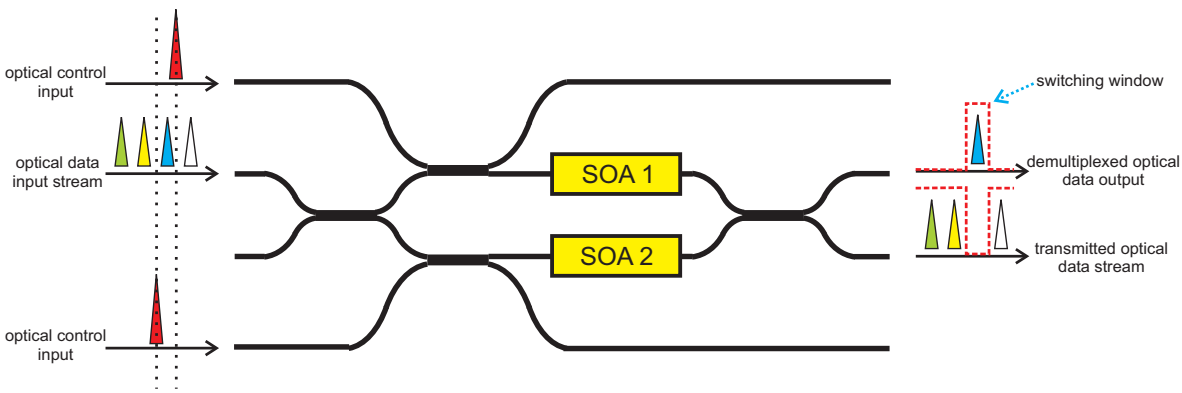

Figure 6.1 Operating scheme of symmetric MZI as all-optical demultiplexer.

The conventional MZI (MZI#5, section 9.5) is monolithically integrated with the semiconductor optical amplifiers with the gain maximum centered at 1550 nm. The performance of this device has been analyzed first in conventional switching scheme, where the wavelengths of the control and data signal are located at 1540 nm and 1550 nm, respectively. The same device was used as switch with shifted wavelengths of data and control signals, 1535 nm and 1560 nm, respectively. Thus realize a GS switching scheme.
The second device, which has been used for 80 Gbit/s demultiplexing experiments, is the 'gain shifted' monolithically integrated MZI (MZI#6, section 9.5). Hereto, the gain shifted semiconductor optical amplifiers with the gain maxima centered at 1500 nm are integrated.
The high-speed all-optical demultiplexing experiments have been performed by using packaged symmetric MZIs (section 9.4). The symmetric MZI chips were fabricated with an advanced technology (section 9.3). By using the tapered passive waveguides the fiber-chip coupling losses have been decreased by at least 4 dB. The improved processing techniques for the SOA layers lead to an enhanced gain and therefore an optimized switching behavior for the conventional switching scheme. Analyzing the switching behavior of both symmetric MZIs has been done using the pump-probe measurements.

6.1.1 Switching Dynamics of Symmetric MZI for 80 Gbit/s Demultiplexing

The switching window measurements have been performed by using a pump-probe experimental setup as described in section 5.10. Herewith the best suited operating condition (e.g. SOA currents, optical pump power) for the all-optical demultiplexing has been found, regarding the shape of the switching windows defined by the contrast ratio and the switching window width.
The typical SOA (I_{SOA1}=90 mA) gain curve within the monolithically integrated conventional MZI (MZI#5) is shown in the Figure 6.2. Here, the pump (control, 13 dBm) and probe (data, 3 dBm) signal wavelengths are close to each other at 1540 nm and 1550 nm, respectively and both are on the top of the ASE curve of the SOAs. A resulting switching window is shown in the Figure 6.3, which corresponds to the conventional switching scheme (I_{SOA1}=90 mA, I_{SOA2}=90 mA, P_{pump1}=13 dBm, P_{pump2}=13 dBm, P_{probe}=3 dBm).

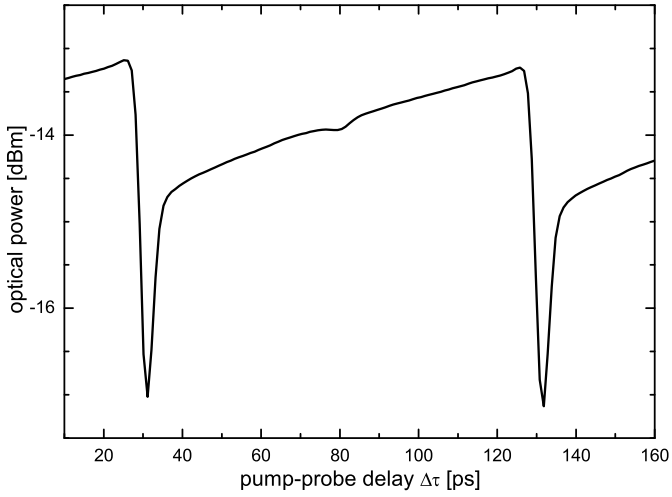

Figure 6.2 Gain recovery of conventional driven SOA_1 of MZI#5, λ_{pump}=1540 nm λ_{probe}=1550 nm, gain maximum of SOA at 1550 nm.

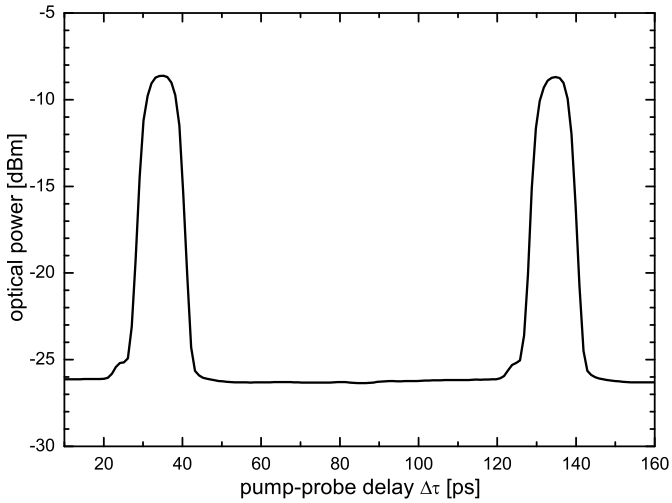

Figure 6.3 Optical switching window of conventional MZI MZI#5, λ_{pump}=1540 nm λ_{probe}=1550 nm, gain maximum of SOA at 1550 nm.

To compare the different switching schemes, the same conventional monolithically integrated MZI device (MZI#5) has been tested in the GS switching scheme, where only the wavelengths of the data and control signals have been changed to 1560 nm and 1534 nm, respectively. Under these conditions the gain recovery and switching dynamics have been analyzed and the results are depicted in the Figure 6.4 and Figure 6.5.

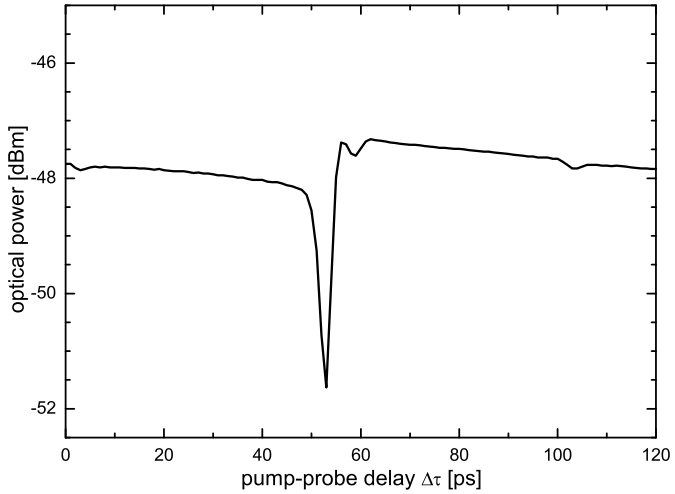

Figure 6.4 Gain recovery curve of GS driven SOA_1 of MZI#5, λ_{pump}=1534 nm λ_{probe}=1560 nm, gain maximum of SOA at 1550 nm.

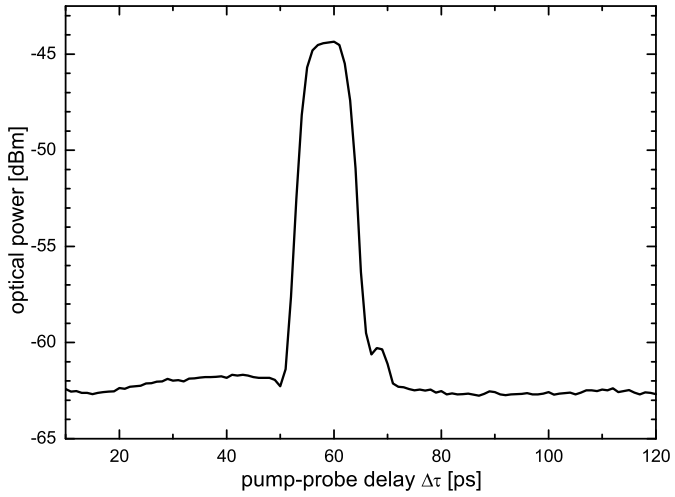

Figure 6.5 Switching window of GS driven conventional MZI MZI#5, λ_{pump}=1540 nm λ_{probe}=1550 nm, gain maximum of SOA at 1550 nm.

The switching properties of the second device, the symmetric GS MZI (MZI#6, section 9.5), have been also analyzed by pump-probe measurements. Hereto, the pump (12.5 dBm) signal wavelength and the probe (11.5 dBm) signal wavelength have been set to 1535 nm and 1560 nm. The wavelength of the pump signal is on the gain curve of the SOA with the gain maximum at 1500 nm and the probe signal is far from the gain maximum of the device.

The measured gain recovery curve (I_{SOA1}=203 mA) is shown in the Figure 6.6. The resulting switching window is depicted in the Figure 6.7, where I_{SOA1}=203 mA, I_{SOA2}=185 mA, P_{pump1}=12.5 dBm, P_{pump2}=14.8 dBm, P_{probe}=11.6 dBm.

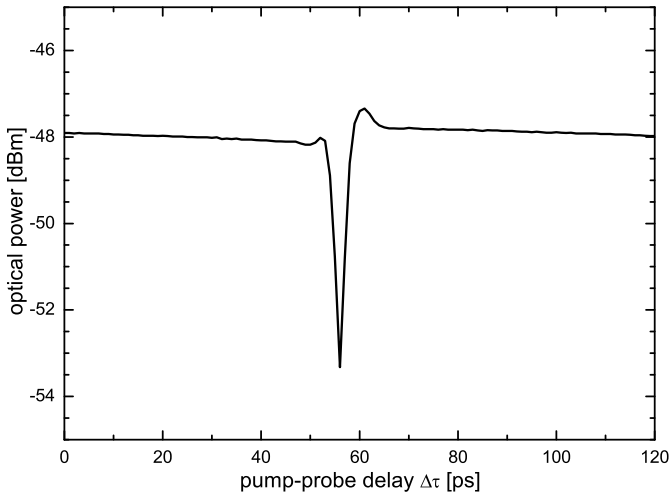

Figure 6.6 Gain recovery curve of GS SOA_1 within the MZI#6 λ_{pump}=1535 nm λ_{probe}=1560 nm, gain maximum of SOA at 1500 nm.

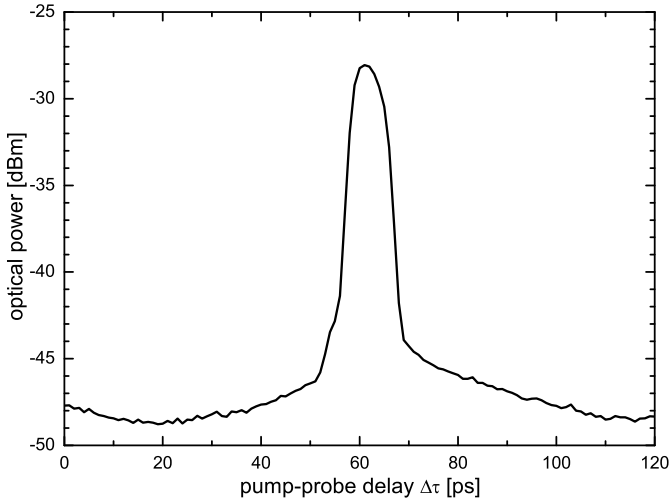

Figure 6.7 Switching window of GS MZI MZI#6, λ_{pump}=1535 nm λ_{probe}=1560 nm, gain maximum of SOA at 1500 nm.

6.1.2 Error-Free All-Optical Demultiplexing at 80 Gbit/s

Error-free all-optical demultiplexing at 80 Gbit/s has been demonstrated by using a system setup corresponding to the Figure 6.8.

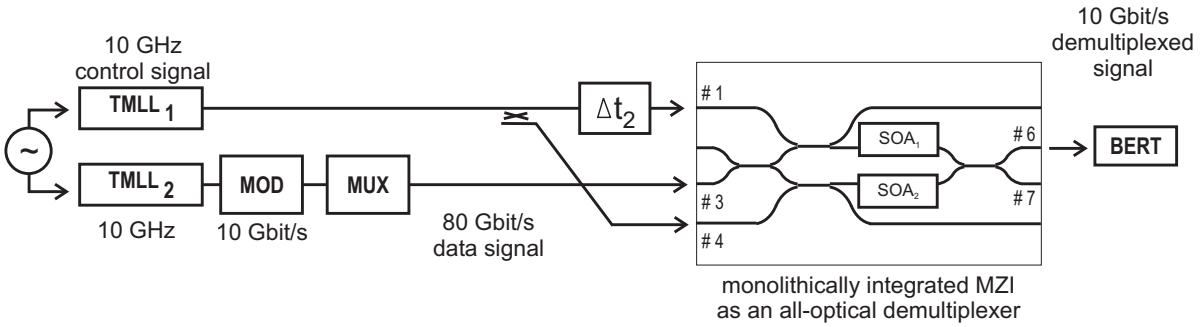

Figure 6.8 Principle experimental setup for 80 to 10 Gbit/s all-optical demultiplexing using monolithically integrated MZI.

The Figure 6.8 illustrates the experimental setup of the monolithically integrated MZI switch in its applications as a 80 Gbit/s to 10 Gbit/s all-optical demultiplexer.
The optical pulses for both control and data signals are generated by using tunable mode-locked lasers [67]. These optical sources provide $sech^2$-pulses of 1.3 ps width at a repetition rate of 10 GHz. The wavelength of the control signal ($TMLL_1$) is set to $\lambda_{control}$ (Table 6.1). The wavelength of the data signal ($TMLL_2$) is set to λ_{data} (Table 6.1). The 10 GHz pulse train from $TMLL_2$ is intensity modulated with a pseudo random bit sequence (PRBS = 2^7-1) to form the RZ data signal. It is then passively multiplexed by a fiber delay line multiplexer (3 stages) to a 80 Gbit/s single polarization data stream and coupled into the MZI at port #3. To ensure a multiplexed pseudo random bit sequence data stream, the bit sequences are shifted against each other by (2^7-1)/2n bit periods with n = 1, 2, 3.
The interferometer is balanced by proper adjustment of the injection currents of the SOAs (Table 6.1) to provide no data transmission to the port #7 in the absence of control pulses. The control signal at 10 GHz is injected into the ports #1 and #4 in the additional arms of the symmetric MZI. The average power in the control arms #1 and #4 is $P_{control1}$ and $P_{control2}$, respectively (Table 6.1). Thus the SOAs become saturated separately at different times, which are defined by an external optical delay line. This time delay Δt_2 determines a gating window in which the data pulses are switched to the port #7 of the integrated switch. The injected average power into the data input port #3 is P_{data} (Table 6.1). To investigate the performance of the monolithically integrated

MZI switch, the bit error rate for 80 to 10 Gbit/s all-optical demultiplexing is measured.

	MZI#5	MZI#5	MZI#6
Switching scheme	Conventional	GS	GS
Gain maximum of SOAs [nm]	1550	1550	1500
$\lambda_{control}$ [nm]	1540	1534	1535
λ_{data} [nm]	1550	1560	1560
$P_{control1}$ [dBm]	13	13	12.5
$P_{control2}$ [dBm]	13	13	14.8
P_{data} [dBm]	3	3	11.6
I_{SOA1} [mA]	90	90	203
I_{SOA2} [mA]	90	90	185
BER results	Figure 6.9	Figure 6.10	Figure 6.11
Power penalty at BER=10^{-9} [dB]	4	3	4
Switching window	Figure 6.3	Figure 6.5	Figure 6.7
FWHM of switching window [ps]	9.3	8.7	7.0
Contrast to pedestal [dB]	16.4	15.8	15.9
Contrast to bottom [dB]	17.7	18.4	20.7
ICR for 80 Gbit/s [dB]	9.1	9.5	10.6
ICR for 160 Gbit/s [dB]	2.8	3.6	6.1

Table 6.1 Experimental details for 80 to 10 Gbit/s all-optical demultiplexing.

Compared to the demultiplexing experiments performed with the conventional monolithically integrated MZI (MZI#5) using the conventional switching scheme the performance of this device at 80 to 10 Gbit/s could be improved only by changing the operating wavelength conditions for the GS switching scheme. The corresponding switching windows for both schemes, presented in the Figure 6.2 and in the Figure 6.4, show a contrast ratio of 17.7 dB and 18.4 dB, respectively. By using both switching windows, all-optical demultiplexing from 80 to 10 Gbit/s could be performed successfully. As shown in the Figure 6.9 and Figure 6.10 the BER curves indicate no error floor. By using the new switching scheme additionally the penalty could be reduced from 4dB to less then 3dB. In this configuration furthermore the error free all-optical demultiplexing is demonstrated for any arbitrary chosen channel.

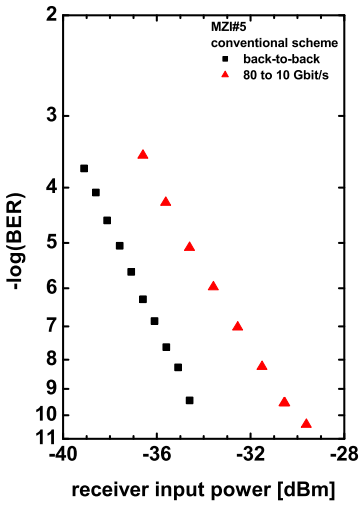

Figure 6.9 BER performance of MZI#5 for 80 to 10 Gbit/s all-optical demultiplexing using the conventional switching scheme. Switching window depicted in Figure 6.3.

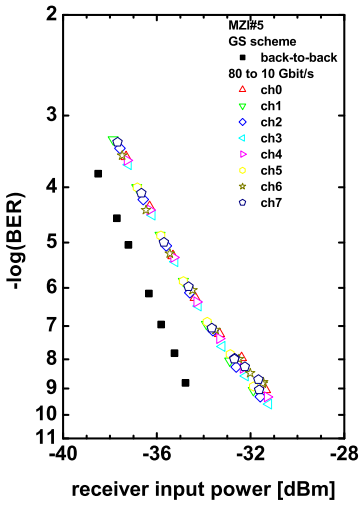

Figure 6.10 BER performance of MZI#5 for 80 to 10 Gbit/s all-optical demultiplexing using the GS switching scheme. Switching window depicted in Figure 6.5.

The best results have been achieved using a GS-MZI (MZI#6) consisting of integrated SOAs with their gain maximum at 1500 nm. Here all-optical demultiplexing could be performed from 160 to 10 Gbit/s. All the 16 arbitrary channels showed comparable BER performance. However, while the 80 to 10 Gbit/s demultiplexing could be performed error-free with a penalty of

4 dB, 160 to 10 Gbit/s demultiplexing could be demonstrated only down to a BER of 10^{-8} due to an arising error floor (Figure 6.11).

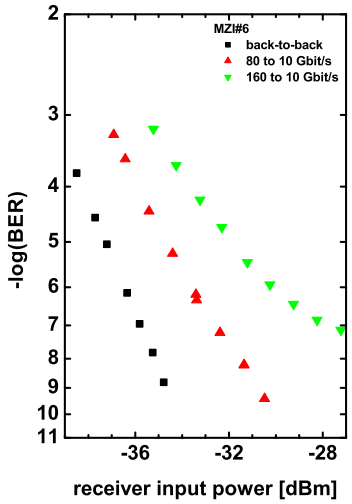

Figure 6.11 BER performance of GS-MZI MZI#6 for 80 and 160 to 10 Gbit/s all-optical demultiplexing using the GS switching scheme. Switching window depicted in Figure 6.7.

The Figure 6.12 depicts the eye diagram of the received signal pulses demultiplexed from 160 to 10 Gbit/s measured by a sampling oscilloscope. The 160 Gbit/s experiment shows a clear and open eye. However, BER performance indicates an error floor at 10^{-8} due to the losses of the monolithically integrated switch, such as passive waveguide losses, fiber-chip coupling losses. Additionally due to the shifted gain spectrum the data signal experiences reduced gain.

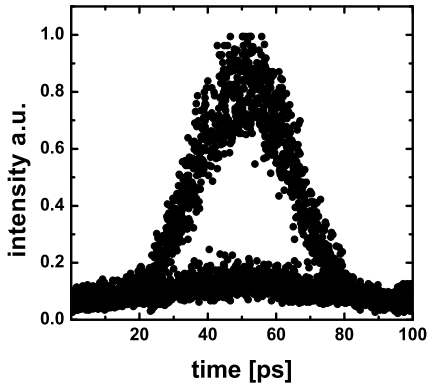

Figure 6.12 Eye diagram of 160 Gbit/s experiment. Switching window depicted in Figure 6.7.

That can be explained by the non ideal switching behavior shown in Figure 6.7. The contrast ratio of about 10 dB between the switched pulse and the next unswitched pulse at a timing distance of only 6.25 ps is too small for error-free detection in the BER receiver. The experiment had been repeated under different operating conditions, but within the available measuring time no higher extinction ratios for the small timing distance of 6.25 ps could be achieved. All optical demultiplexing by using symmetric monolithically integrated Mach-Zehnder interferometer structures have been performed error-free at 80 to 10 Gbit/s for both conventional and gain shifted switching schemes, and with a BER down to 10^{-7} at 160 to 10 Gbit/s demultiplexing for the gain shifted MZI. For any arbitrary chosen channel the demultiplexing performance is comparable good without any readjustment of the measurement setup.
The switching windows, gain and phase dynamics have been measured to explain the switching behavior of different schemes and to chose the best operating conditions for all-optical demultiplexing experiments. As expected the GS scheme provides an improved performance.

6.2 GS-MZI as 160 Gbit/s Error-Free All-Optical Demultiplexer

The first error-free 160 Gbit/s all-optical demultiplexer based on monolithically integrated MZI has been realized and the system performance has been successfully demonstrated by using the novel GS switching scheme with GS-MZI [69]. Error-free demultiplexing beyond 100 Gbit/s has been achieved first with hybrid-integrated MZI [74] at 168 Gbit/s and with hybrid GT-MZI [75] at 160 Gbit/s.
In this section, 160 Gbit/s error-free all-optical demultiplexing experiments are reported by using a monolithically integrated MZI (MZI#7, section 9.5) with GS-SOAs [69]. The switching dynamics of MZI#7 was discussed in detail in Chapter 5. The minimum achievable window width is 3 ps, the highest contrast value is about 27 dB (Figure 5.27). For the demultiplexing experiments at 160 Gbit/s a window width of about 6 ps with a contrast of about 22 dB is sufficient. In a range of ~20 dB linear dependence is observed (Figure 5.32). This dynamic range is limited by amplified spontaneous emission for low input power and by gain saturation of the SOA for high input power. In this linear range, the switching performance of the GS-demultiplexer is independent on the data input power.

The Figure 6.13 illustrates the experimental setup of the monolithically integrated GS-MZI switch in its application as a 160 Gbit/s to 10 Gbit/s all-optical demultiplexer. The key components of this interferometric switch are the two GS-SOAs integrated within its branches. The gain maximum of the SOAs is at a wavelength of 1500 nm far from the data wavelength, which is at 1560 nm. The experimental comparison of the GS-MZI switch with the conventional MZI, regarding its better linearity, better contrast ratio and a higher phase shift can be found in Chapter 5.

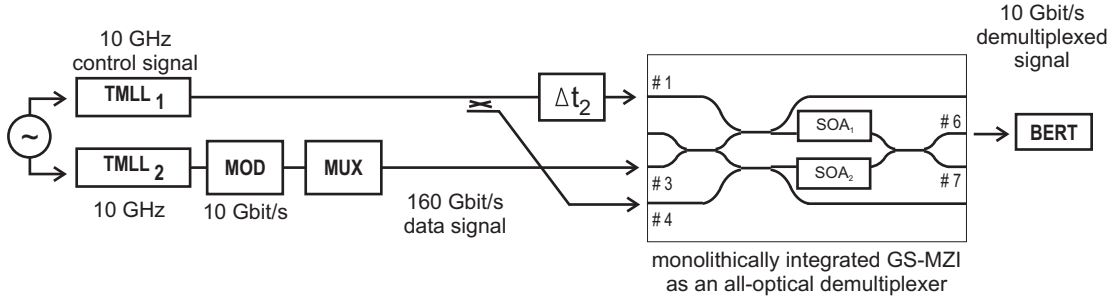

Figure 6.13 Experimental setup for 160 Gbit/s demultiplexing.

The optical pulses for both control and data signals are generated by using the tunable mode-locked lasers [67]. These optical sources provide $sech^2$-pulses of 1.3 ps width at a repetition rate of 10 GHz. The wavelength of the control signal ($TMLL_1$) is set to $\lambda_{control}$ = 1535 nm within the gain region of the GS-SOAs, where conventional Erbium doped fiber amplifiers still can be used for amplification. The wavelength of the data signal ($TMLL_2$) is set to λ_{data} = 1560 nm. The 10 GHz pulse train from $TMLL_2$ is intensity modulated with a pseudo random bit sequence (PRBS = 2^7-1) to form the RZ data signal. It is then passively multiplexed by a fiber delay line multiplexer (4 stages) to a 160 Gbit/s single polarization data stream and coupled into the GS-switch at port #3. To ensure a multiplexed pseudo random bit sequence (PRBS) data stream, the bit sequences are shifted against each other by (2^7-1)/2n bit periods with n = 1, 2, 3, 4.
The interferometer is balanced by proper adjustment of the injection currents of the SOAs to provide no data transmission to the port #7 in the absence of control pulses. The control signal at 10 GHz is injected into the ports #1 and #4 in the additional arms of the symmetric MZI. The average power in the control arms #1 and #4 is $P_{control1}$ = 15.5 dBm and $P_{control2}$ = 17.7 dBm, respectively. Thus the SOAs become saturated separately at different times, which are defined by an external optical delay line. This time delay Δt_2= 6 ps determines a gating window in which the data pulses are switched to the port #7 of the integrated switch. The injected average power into the data input port #3 is P_{data} = 5.5 dBm.

To investigate the performance of the monolithically integrated GS-MZI switch, the bit error rate for 160 to 10 Gbit/s and 80 to 10 Gbit/s all-optical demultiplexing is measured.
The Figure 6.14 illustrates the BER performances of the system in a back-to-back arrangement and in the all-optical demultiplexing experiment from 80 Gbit/s to 10 Gbit/s and 160 Gbit/s to 10 Gbit/s by using the GS-MZI switch. The received optical power is measured at the 10 Gbit/s receiver.
For the back-to-back curve the unmultiplexed 10 Gbit/s signal is used. Error-free operation is obtained in cases, 80 to 10 Gbit/s and 160 to 10 Gbit/s all-optical demultiplexing, respectively.
For the all-optical 80 Gbit/s demultiplexing, the BER performance is excellent. The small power penalty of 1 dB (BER = 10^{-9}), which can be attributed to the slightly decreased signal-to-noise ratio, is due to the loss of the device (about 20 dB), which can be reduced by improved fiber-chip coupling.
For the all-optical 160 Gbit/s demultiplexing the power penalty at a BER of 10^{-9} is about 3.5 dB. An indication of an error floor at 10^{-11} is observed, which is mainly due to the jitter in the control pulse source. However, for all the 16 channels (under unchanged operation conditions), error-free operation (PRBS = 2^7-1) is obtained with a BER less than 10^{-9}. Figure 6.15 illustrates the system penalty of all OTDM channels for a BER less then 10^{-9}. The variation in the system penalty for different channels is due to the losses in the passive fiber delay line multiplexer.

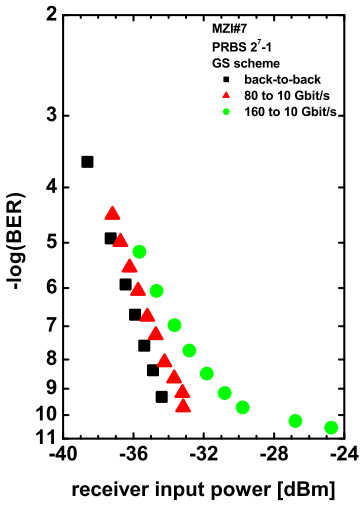

Figure 6.14 BER performance of GS Mach-Zehnder interferometer as an all-optical demultiplexer at 80 Gbit/s and 160 Gbit/s data streams..

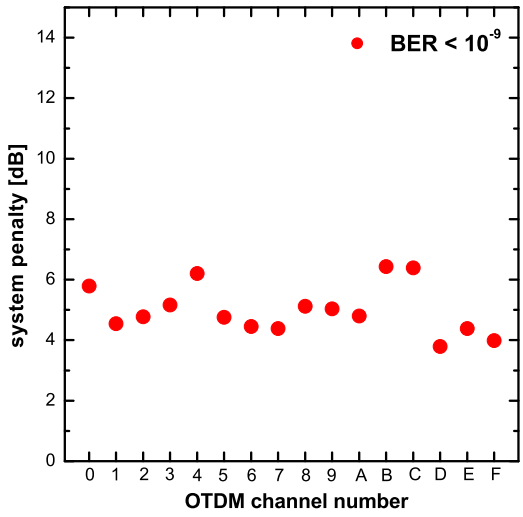

Figure 6.15 The system penalty of all OTDM channels for error-free all-optical demultiplexing at 160 Gbit/s.

The error-free all-optical demultiplexing of 160 Gbit/s data signals to 10 Gbit/s was performed with the monolithically integrated Mach-Zehnder interferometer comprising ‘gain shifted’ SOAs. The GS-MZI is a compact and stable device providing switching windows with high contrast and short window width. Using shorter control pulses and reducing the jitter of the pulse sources can expect demultiplexing from even higher data rates.

7 Conclusions and Outlook

This thesis describes theoretical and experimental studies on a monolithically integrated ‘gain shifted’ Mach-Zehnder interferometer as an all-optical demultiplexer. Particularly design, switching dynamics and system performance of this demultiplexer were considered.

7.1 Conclusions

7.1.1 Gain Shifted Mach-Zehnder Interferometer

The existing solutions for optical demultiplexers have been reviewed in Chapter 2. The symmetric Mach-Zehnder interferometer has been used in this thesis for the development of all-optical demultiplexers towards ultrafast application, due to its superior specifications compared to other structures. The symmetric MZI enables bit-rate flexible operation, since the switching window width can be determined by using an external delay between the control signals. The data and control pulses can propagate co- and contra-directional, which provides further flexibility regarding the operation. The possibility to saturate the SOAs separately enables also an improved contrast ratio for the switched signal.
The existing switching schemes have been compared within the Chapter 3. Here, the drawbacks of the conventional and ‘gain transparent’ schemes motivate the development of the ‘gain shifted’ scheme.
The ‘gain shifted’ switching scheme investigated here was intended to find a compromise between the advantages and disadvantages of the ‘conventional’ and ‘gain transparent’ switching scheme. Moreover, this work presents the first monolithically integrated interferometric switch in a non-conventional switching scheme.
The shifted gain spectrum due to the band gap shift of the SOA reduces the amplified spontaneous emission noise. Therefore, the pattern effects and cross-talk are expected to be low. Further, the reduced gain dependence of the data signal leads to a linearity of about 20 dB and wide bandwidth. The enhanced phase response of the ‘gain shifted’ switching scheme enables high switching contrast up to 27 dB.

Additionally the ‘gain shifted’ switching scheme is compatible with the all-optical clock recovery proposed within an all-optical signal regeneration concept. This is a prerequisite for advanced applications of the MZI switches e.g. in a complete true all-optical 3R regeneration scheme. The relative small distance between data- and control-signal wavelengths, compared to the gain transparent switching scheme, allows a wavelength translation by using the all-optical wavelength converter. Furthermore, the insertion losses, which lead to a limitation in the gain transparent switching scheme, are reduced by using the ‘gain shifted’ scheme.

7.1.2 Design of Monolithically Integrated MZI

A wide range of basic components is provided by photonic integration technologies. To combine these possibilities to functional devices, is the main challenge, since they have to meet the requirements for system applications.
In Chapter 4 the state of art of technology has been summarized, which enabled the design of further optimized monolithically integrated Mach-Zehnder interferometer switch for error-free 160 Gbit/s all-optical demultiplexing application. The polarization insensitive design of the monolithically integrated gain shifted Mach-Zehnder interferometer has been also presented, which enables process tolerant technological realization of the devices with reduced internal losses, reduced internal reflections and improved fiber-chip coupling.
The compactness of the realized devices has to be ascribed to the applied design of MZI consisting of MMI-couplers, waveguide bends and semiconductor optical amplifiers butt-coupled to the passive waveguides within the buried hetero structure technology. By introducing the angled active/passive interface, AR-coating and angled facets internal reflections have been reduced.
The usage of pn-blocking, compact low-loss MMI-couplers and waveguide bends, and spot size converters combined with double-mode passive waveguides lead to improvements of the over-all loss budget.
Due to the selected switching scheme, the all-optical demultiplexer is compatible with other optical components within the C-band.
Furthermore, the applied half-stack integration technology and the new design provide reproducible and process tolerant technological realization of the monolithically integrated MZI.

7.1.3 Switching Dynamics of GS-MZI

In Chapter 5 the characterization of monolithically integrated Mach-Zehnder interferometer has been described in view of the ultrafast demultiplexing op-

eration. Static and dynamic switching performances of the gain shifted Mach-Zehnder interferometer have been analyzed and compared.
The symmetry properties of monolithically integrated MZI, and power characteristics of integrated SOAs are discussed by monitoring the ASE output power at different output ports. The gain spectrum and polarization dependence of gain shifted SOAs have been investigated. A polarization sensitivity of 1 dB has been achieved by using the GS scheme. The analyzed losses in passive waveguides amount 7 dB per centimeter. In current induced switching experiments, the gain shifted switching scheme shows a phase shift of 17π compared to a phase shift of 9π in the conventional scheme. In case of optically induced switching the GS-MZI provides a phase shift of π and a contrast ratio of 11 dB by only 5 dB change of the control signal power.
In particularly, the dynamic response of the semiconductor optical amplifiers, and switching dynamics of gain shifted Mach-Zehnder interferometers has been evaluated by using pump-probe measurements.
Gain and phase response of the integrated GS-SOAs have been analyzed for the first time by using the switching dynamics. The relative phase shift within the interferometric structure extends from $\pi/2$ to $3\pi/4$ by introducing the GS switching scheme. The parameters of the switching window, namely its width and depth, are discussed in the dependence of the actuating variables such as external delay, probe signal wavelength and probe signal input power. The GS-MZI switch provides switching windows with FWHM of 3 ps to 20 ps and with a contrast ratio up to 27 dB. The width of switching window depends linearly on the external delay. The switched signal power shows a linear dependence on the variation of the input signal power over a range of 20 dB. A switching window with a contrast ratio of 22 dB and with FWHM of 6 ps has been used successfully for error-free all-optical demultiplexing.

7.1.4 System Performance of GS-MZI

The system performances of the realized MZIs are presented in Chapter 6. The devices have been tested in the OTDM transmission test bed of HHI. The system tests at 80 Gbit/s and 160 Gbit/s have been performed by using different generations of devices, which represent the development steps of all-optical demultiplexer towards higher bit-rate operation.
First, symmetric Mach-Zehnder Interferometer has been used as all-optical demultiplexer at 80 Gbit/s data stream. To compare the conventional and gain shifted switching schemes, all-optical demultiplexing has been performed on the same device. For both switching schemes error-free demultiplexing has been observed. By using the new switching scheme additionally the penalty could be reduced from 4 dB to less then 3 dB. In this configuration, error-free

all-optical demultiplexing is demonstrated for any arbitrary chosen channel. Furthermore, best results have been achieved using the first generation of GS-MZI with a gain shifted to 1500 nm. All-optical demultiplexing could be performed from 80 to 10 Gbit/s error-free, with a penalty of 3 dB.
Finally, the first error-free all-optical demultiplexing experiments from 160 Gbit/s to 10 Gbit/s have been performed with monolithically integrated Mach-Zehnder interferometer comprising 'gain shifted' semiconductor optical amplifiers, which have been processed by using the advanced integration technology. Here, the power penalty at a BER of 10^{-9} is about 3.5 dB. An indication of an error floor at 10^{-11} is observed, which is mainly due to the jitter in the control pulse source. For all the 16 OTDM channels (under unchanged operational conditions), error-free operation (PRBS = 2^7-1) is obtained with a BER less than 10^{-9}. The monolithically integrated 'gain shifted' MZI as an all-optical demultiplexer meets the general requirements for nonlinear switching devices in the network applications [39]:

- **Operating power dependence:** The pre-amplification of signals is possible by using EDFAs. The device is tolerant to a certain degree of variation in data signal power.
- **Speed of response:** Due to the MZI configuration and the GS switching scheme, all-optical demultiplexing could be performed at speeds very much faster than the relaxation time of the integrated SOAs.
- **Optical loss:** Overall losses including input- and output-coupling are small compared to its counterparts due to the optimized fiber-chip coupling and the design for advanced processing technology.
- **Device format:** The monolithically integrated chip has the dimensions of 1 mm x 5 mm. It is stable and the module is insensitive to thermal expansion, mechanical shock and other environmental disturbances.
- **Spectral range and sensitivity:** The working signal wavelengths are within the C-band, which is within the gain spectrum of EDFAs.
- **Polarization sensitivity:** The polarization insensitivity is within 1 dB for the tensile strained SOAs.
- **Spectral purity:** Since the device bases on semiconductors there is no dispersion induced temporal walk-off. The GS-MZI does not induce significant wavelength shifts, chirp or pulse broadening.
- **Latency:** Because of its small dimensions, the latency is negligible for in-line signal processing in a long distance point-to-point link, also in network context.

7.2 Outlook

7.2.1 Integration

For the design and development of a polarization insensitive monolithically integrated Mach-Zehnder interferometer as an all-optical demultiplexer, it is recommended to adjust the width and thickness of the layer stack and the crystallographic strain within the active layer. Additionally the SOA can be dimensioned in such a way that a residual polarization sensitivity of the MZI could be compensated for a given working point. The angled facet is an important tool to reduce the facet reflections. However, AR-coating layers have to be adapted to the introduced off angle. For the monolithically integrated MZI an off angle of 7° on the chip (corresponding to ca. 23° in air) has been found to be sufficient for the reduction of facet reflections on one hand and a good technological reproducibility on the other hand. The introduction of mode filters (bends with adequate radius) in front of the MMI coupler is essential since the dimensions of the MMI-coupler are designed under assumption of injection of the fundamental mode from the supplying waveguide. Here any deviation can lead to a not calculable behavior of the coupler concerning polarization and optical losses.
In terms of compact, stable photonic devices, monolithical integration is recommended. Although it is a complex process to develop devices with special requirements, monolithical integration is well suited for low cost production.
For verifying new approaches and to test new ideas, hybrid integration opens new frontiers. The possibility to optimize different elements in different platforms and to combine them to functional subsystem is attractive. The main challenge of this integration technology is to achieve low-loss interfaces.

7.2.2 All-Optical Switching

For all-optical ultrafast switching, interferometric structures are recommended, especially Mach-Zehnder interferometer, since stability is provided by integration. The asymmetric MZI structure is simple, but because of its asymmetric shaped switching windows not suitable for high-speed applications. The two additional arms of symmetric MZI enable to control the SOAs separately leading to additional flexibility in the bit-rate and enhanced switching properties like high contrast and narrow switching window.
The recommended lengths of the integrated semiconductor optical amplifiers for all-optical demultiplexing applications are about 1000 µm to 1500 µm for

symmetric MZI. Longer SOAs cause a broadening of the pulses and reduce the switching performance.
In case of all-optical demultiplexing short, low-jitter control pulses are required to provide narrow and stable switching windows. By using ps-pulses a switching window width of 3 ps has been obtained, which can be used for demultiplexing from a 320 Gbit/s data stream.
Depending on the availability of pre-amplification and on the special requirements of the application, the gain shift of the integrated SOAs has to be adapted to find a compromise between the switching performance and system resources.

7.2.3 Further Works

With the gain shifted Mach-Zehnder interferometer structure and its advanced technology as described in this thesis, there is a good feasibility of fabricating low-loss, polarization insensitive monolithically integrated interferometer for ultrafast all-optical switching. Nevertheless starting from the state of the art, there are still several possible improvements, which are necessary on the way to a product. By introducing thicker separate confinement layers into the SOA layer structure a further improvement of the polarization sensitivity can be achieved. This not only influences the basic characteristics, but also leads due to higher tolerances for the epitaxial growth process (at thin layers the absolute error of the growth process of ± 2.5 nm is dominant) to a better reproducibility. Introduction of mono-mode waveguides in combination with Fe-blocking will reduce the passive waveguide losses. The usage of moderate taper dimensions (0.7 µm) will enhance the processing tolerances.
An error-free all-optical demultiplexing at 160 Gbit/s was demonstrated in this thesis for an OTDM system. This result was obtained by using an ideal system with a perfect synchronization of transmitter and receiver. Here, the synchronization of control pulses at the receiver node has been realized directly from the clock generator of the data channels. However, in practical receiver nodes of OTDM systems the clock signals should be extracted/recovered from the data signals. Therefore, an all-optical clock recovery with ps-pulses and low jitter is necessary. To improve the transparency of the receiver nodes in an OTDM network monitoring schemes should be added. Further functionalities like add-drop multiplexing, full-demultiplexing and bit processing can attract the all-optical networks.

8 Bibliography

[1] R. Ramaswami, K. N. Sivarajan, 'Optical Networks: A Practical Perspective', Morgan Kaufmann Publishers Inc. (1998).

[2] S. Kawanishi, 'Ultrahigh-Speed Optical Time-Division-Multiplexed Transmission Technology Based on Optical Signal Processing', IEEE Jour. of Quantum Electronics vol.34 pp.2064-2079 (1998).

[3] T. Tekin, 'Update and Comparison of Existing Solutions for OTDDmux', unpublished report HHI, Berlin, Germany (1998).

[4] D. Hoffmann, 'Optische Modulatoren und Schalter' Kapitel 15 in E. Voges, K. Petermann, 'Optische Kommunikationstechnik: Handbuch für Wissenschaft und Industrie', Springer (2002).

[5] E. Hilliger, 'Optisches Schalten mit Elektroabsorptionsmodulatoren', PhD thesis, Technische Universität Berlin, Germany (2003).

[6] H.G. Weber, 'Nichtlineare Optik und optische Signalverarbeitung' Kapitel 16 in E. Voges, K. Petermann, 'Optische Kommunikationstechnik: Handbuch für Wissenschaft und Industrie', Springer (2002).

[7] P.A. Andrekson, N.A. Olsson, J.R. Simpson, T. Tanbun-Ek, R.A. Logan, K. Haner, '16 Gbit/s All-Optical Demultiplexing Using Four-Wave Mixing', Electron. Lett. vol. 27, pp. 922-924 (1991).

[8] R. Ludwig, G. Raybon, 'All-Optical Demultiplexing Using Ultrafast Four-Wave Mixing in a Semiconductor Laser Amplifier at 20 Gbit/s', Tech. Dig. ECOC'93 3, 57-60 (1993).

[9] S. Kawanishi, T. Morioka, O. Kamatani, H. Takara, J.M. Jacob, M. Saruwatari, '100 Gbit/s All-Optical Demultiplexing Using Four-Wave Mixing in a Travelling Wave Laser Diode Amplifier, Electron. Lett. vol. 30, pp. 981-982 (1994).

[10] S. Kawanishi, T. Morioka, O. Kamatani, H. Takara, M. Saruwatari, '100 Gbit/s, 200km Optical Transmission Experiment Using Extremely Low Jitter PLL Timing Extraction and All-Optical Demultiplexing Based on Polarisation Insensitive Four-Wave Mixing', Electron. Lett. vol. 30, pp. 800-801 (1994).

[11] T. Morioka, H. Takara, S. Kawanishi, K. Uchiyama, M Saruwatari, 'Polarisation-Independent All-Optical Demultiplexing up to 200Gbit/s Using Four-Wave Mixing in a Semiconductor Laser Amplifier', Electron. Lett. 32, 840-842 (1996).

[12] G. Contestabile, F. Martelli, A. Mecozzi, L. Graziani, A. D'Ottavi, P. Spano, G. Guekos, R. Dall'Ara, J. Eckner, 'Efficiency Flattening and Equalization of Frequency Up- and Down-Conversion Using Four-Wave Mixing in Semiconductor Optical Amplifiers', Photon. Tech. Lett. vol. 10, pp. 1398-1400 (1990).

[13] I. Ogura, H. Kurita, Y. Hashimoto, T. Shimizu, H. Yokoyama, 'Demonstration of All-Optical Clock Recovery and Demultiplexing With a Simple-Geometry Utilizing Mode-Locked Laser Diodes', Proc. IOOC /ECOC'97 2, 77-80 (1997).

[14] H. Kurita, I. Ogura, H. Yokoyama, 'Ultrafast All-Optical Signal Processing With Mode-Locked Semiconductor Lasers', IEICE Trans. Electron. E81-C, 129-139 (1998).

[15] http://www.photonics.com/dictionary/

[16] M. Eiselt, 'Optical Loop Mirror With Semiconductor Laser Amplifier', Electron. Lett. vol. 28, pp. 1505-1507 (1992).

[17] J.P. Sokoloff, P.R. Prucnal, I. Glesk, M. Kane, 'A Terahertz Optical Asymmetric Demultiplexer (TOAD)', IEEE Photon. Tech. Lett. vol. 5, pp. 787-790, (1993).

[18] A.D. Ellis, D.M. Spirit, 'Compact 40Gbit/s Optical Demultiplexer Using a GaInAsP Optical Amplifier', Electron. Lett. vol. 29, pp. 2115-216 (1993).

[19] M. Eiselt, W. Pieper, H. G. Weber, 'SLALOM: Semiconductor Laser Amplifier in a Loop', J. of Lightwave Tech. vol. 13, pp.2099-2112 (1995).

[20] M.G. Kane, I. Glesk, J.P. Sokoloff, P.R. Pruvnal, 'Asymmetric Optical Loop Mirror: Analysis of an All-Optical Switch', Applied Optics vol. 33, pp. 6833-6842 (1994).

[21] I. Glesk, J.P. Sokoloff, P.R. Prucnal, 'Demonstration of All-Optical Demultiplexing of TDM Data at 250 Gbit/s', Electron. Lett. vol. 30, pp. 339-341 (1994).

[22] K. Suzuki, K. Iwatsuki, S. Nishi, M. Saruwatari, 'Error-Free Demultiplexing of 160 Gbit/s Pulse Using Optical Loop Mirror Including Semiconductor Laser Amplifier', Electron. Lett. vol. 30, pp. 1501-1503 (1994).

[23] S. Diez, R. Ludwig, H.G. Weber, 'All-optical Switch for TDM and WDM/TDM Systems Demonstrated in a 640 Gbit/s Demultiplexing Experiment', Electron. Lett. vol. 34, pp. 803-805 (1998).

[24] E. Jahn, N. Agrawal, W. Pieper, H.J. Ehrke, W. Pieper, D. Franke, W. Fürst,C. M. Weinert, 'Monolithically Integrated Nonlinear Sagnac Interferometer and Its Application as a 20 Gbit/s All-Optical Demultiplexer', Electron. Lett., vol. 32, pp. 782-784 (1996).

[25] N.S. Patel, K. A. Rauschenbach, and K. L. Hall, '40 Gbit/s Demultiplexing Using an Ultrafast Nonlinear Interferometer (UNI)', IEEE Photonics Letters, Vol. 8, No. 12, (1996).
[26] A.I.S. Bhardwaj, 'All-Optical Logic Circuits based on the Polarization Properties of Non-Degenerate Four-Wave Mixing', PhD thesis, California Institute of Technology, California (2001).
[27] C. Schubert, 'Interferometric Gates for All-Optical Signal Processing', PhD thesis, Technische Universität Berlin, Germany (2004).
[28] K. Tajima, 'All-Optical Switch with Switch-Off Time Unrestricted by Carrier Lifetime', Jpn. J. Appl. Phys. Vol. 32 pp.L1746-L1749 (1993).
[29] S. Nakamura, K. Tajima, Y. Sugumoto, 'Experimental Investigation on High-Speed Switching Characteristics of a Novel Symmetric Mach-Zehnder All-Optical Switch', Appl. Phys. Lett. vol.65, pp.283-285 (1994).
[30] K.I. Kang, I. Glesk, T.C.G. Chang, P.R. Prucnal, R.K. Boncek, 'Demonstration of All-Optical Mach-Zehnder Demultiplexer', Electron. Lett. vol. 31, pp. 749-750 (1995).
[31] E. Hilliger, S. Diez, H.J. Ehrke, R. Ludwig, C. Schmidt, H.G. Weber, J.Y. Emery, '80Gbit/s All-Optical Demultiplexing Using a hybrid Mach-Zehnder–Interferometer Switch with Gain-Clamped Semiconductor Optical Amplifiers', Photon. in switch, Santa Barbara (1999).
[32] A.W. O'Neill, R.P. Webb, 'All-Optical Loop Mirror Switch Employing an Asymmetric Amplifier/Attenuator Combination', Electron. Lett. vol.26, pp. 2008-2009 (1990).
[33] E. Jahn, N. Agrawal, M. Arbert, H.J. Ehrke, D. Franke, R. Ludwig, W. Pieper, H.G. Weber, C.M. Weinert, '40 Gbit/s All-Optical Demultiplexing Using a Monolithically Integrated Mach-Zehnder Interferometer With Semiconductor Laser Amplifiers', Electron. Lett. vol. 31, pp. 1857-1858 (1995).
[34] E. Jahn, N. Agrawal, H.J. Ehrke, R. Ludwig, W. Pieper, H.G. Weber, 'Monolithically Integrated Asymmetric Mach-Zehnder Interferometer as a 20 Gbit/s All-Optical Add/Drop Multiplexer for OTDM Systems', Electron. Lett. vol. 32, pp. 216-217 (1996).
[35] P. Gunning, J.K. Lucek, D. Nesset, J.V. Collins, C.W. Ford, D. Pitcher, K. Smith, D. Cotter, E. Jahn, N. Agrawal, A.S. Siddiqui, ,Optical-TDMA LAN Incorporating Packaged Integrated Mach-Zehnder Interferometer Channel Selector', Electron. Lett. vol. 33, pp.1404-1405 (1997).
[36] Mikkelsen, T. Durhuus, C. Jorgensen, S.L. Danielsen, R.J.S. Pedersen, K.E. Stubkjaer, 'Wavelength Conversion Using Interferometric Struc-

tures Containing Semiconductor Laser Amplifiers', Optical Amplifiers and their App. OSA Tech. Dig. Series vol. 18, pp. 238-241 (1995).

[37] M. Vaa, B. Mikkelsen, K.S. Jespen, K.E. Stubkjaer, R. Hess, M. Duelk, W. Vogt, E. Gamper, E. Gini, P. A. Besse, H. Melchior, 'Bit Error Rate Assessment of 80 Gb/s All-Optical Demultiplexing by a Monolithically Integrated Mach-Zehnder Interferometer With Semiconductor Optical Amplifiers', ECOC 97 Conf. Pub. No.448, pp. 31-34 (1997).

[38] J. Leuthold, P.A. Bess, E. Gamper, M Dülk, W. Vogt, H. Melchior, 'Cascadable MZI All-Aptical Switch With Separate Ports For Data- and Control-Signals', ECOC 98, pp. 463-464 (1998).

[39] D. Cotter, 'Nonlinear Optics For Future High-Speed Photonic Networks', Nonlinear Optics vol. 13 pp. 185-201, 1995.

[40] T. Tekin, M. Schlak, W. Brinker, B. Maul, R. Molt, 'Monolithically Integrated MZI Comprising Band Gap Shifted SOAs: A New Switching Scheme For Generic All-Optical Signal Processing', Proc. of 26th Europ. Conf. Opt. Commun. (ECOC'2000), vol.3, pp. 123-124 (2000).

[41] S. Diez, 'All-Optical Signal Processing by Gain-Transparent Semiconductor Devices', PhD thesis, Technische Universitär Berlin, Germany (2000).

[42] J.P.R. Lacey, G.J. Pendock, R.S. Tucker, 'All-Optical 1300-nm to 1550-nm Wavelength Conversion Using Cross-Phase Modulation in a Semiconductor Optical Amplifier', IEEE Photonics Technology Letters vol.8, pp. 885-887 (1996).

[43] R. Ludwig, U. Feiste, S. Diez, C. Schubert, C. Schmidt, H. J. Ehrke, H. G. Weber, 'Unrepeatered 160 Gbit/s RZ single-channel transmission over 160 km of standard fibre at 1550 nm with hybrid MZI optical demultiplexer', Electronics Letters, Vol. 36, No. 16, pp. 1405 (2000).

[44] G.P. Agrawal, N.K. Dutta, 'Semiconductor lasers', Kluwer Academic, Boston, (1993).

[45] M. Schilling, T. Durhuus, C. Joergensen, E. Lach, D. Baums, K. Daub, W. Idler, G. Laube, K.E. Stubkjaer, and K. Wuensel, 'Monolithic Mach-Zehnder Interferometer Based Optical Wavelength Converter Operated at 2.5Gbit/s With Extinction Ratio Improvement and Low Penalty', Proceedings of 20th European Conference on Optical Communication, vol. 2, 647-650 (1994).

[46] G.P. Agrawal, N.K. Dutta, 'Long Wavelength Semiconductor Lasers', ch. 5, ISBN 0-442-20995-9 Van Nostrand Reinhold, New York (1986).

[47] E. Jahn, 'Monolithically Integrated Semiconductor Laser Amplifier Based Interferometers for Optical Signal Processing', PhD thesis, Technische Universität Berlin, Germany (1996).

[48] D. Marcuse, ‘Bending Losses of Asymmetric Slab Waveguide’, The Bell System Technical Journal, vol. 50, pp. 2551-2563 (1971).
[49] Ch. Schmidt, Special design calculations done at HHI.
[50] O. Bryndahl, ‘Image Formation Using Self-Imaging Techniques’, J. Opt. Soc. Am. vol. 63, pp. 416-418 (1973).
[51] R. Ulrich, G. Ankele, ‘Self-imaging Inhomogeneous Planar Optical Waveguides’, Appl. Phys. Lett, vol.27, pp.337-339 (1975).
[52] L.B. Soldano, F.B. Veerman, M.K. Smit, B.H. Verbeek, A.H. Dubost, E.C.M. Pennings, ‘High-Performance Monomode Planar Couplers Using a Short Multi-Mode Interference Section’, Proc. Of 17th ECOC part 1, pp. 225-228 (1991).
[53] C.M. Weinert, ‘Three-Dimensional Coupled Mode Method for Simulation of Coupler and Filter Structures’, IEEE Jour. of Lightwave Techno. Vol.10, pp. 1218-1225 (1992).
[54] C. Weinert. Special design calculations done at HHI.
[55] R. Ludwig, ‘Experimentelle Untersuchungen an Halbleiterlaserverstärkern für die optische Nachrichtentechnik’, PhD thesis, Technische Universität Berlin, Germany (1993).
[56] T. Saitoh, T. Mukai, ‘Traveling-Wave Semiconductor Laser Amplifiers’ in Coherence, Amplification, and Quantum Effects in Semiconductor Lasers, editor Y. Yamamoto (1991).
[57] M. Reed, ‘The Free Space Radiation Mode Method in Integrated Optics’, Diss. University of Nottingham (1998).
[58] R. Molt, Special design calculations done at HHI.
[59] J. Buus, M.C.Farries, D.J.Robbins, ‘Reflectivity of Coated and Tilted Semiconductor Facets’, IEE Journal of Quantum Electronics, Vol. 27, No.6 (1991).
[60] M. Schlak, special recipe developed at HHI.
[61] K. Petermann, ‘Laser Diode Modulation and Noise’, Advances in Optoelectronis, 3, Kluwer Academics Publishers (1988).
[62] J-Y. Emery, P. Doussiere, L.Goldstein, F. Pommereau, C. Fortin, R. Ngo, N. Tscherptner, J-L Lafragette, P. Aubert, F. Brillouet, ‘New, Process Tolerant, High Performance 1.55um Polarization Insensitive Semiconductor Optical Amplifier Based on Low Tensile Bulk GaInAsP’, ECOC 1996, WeD 2.3, pp.165-168 22nd European Conference on Optical Communication (1996).
[63] Philip Morris Stiftung, Philip Morris Research Price'99 press kit, München, Germany (1999).
[64] M.W. Austin, P.C. Kemeny, ‘Measurement of Semiconductor Optical Waveguide Loss Using a Fabry-Perot Interference Technique’, ECIO 1985, Berlin, Germany (1985).

[65] A. Gerster, M. Maile, Chr. Hentschel, 'State of the Art Characterization of Optical Components for DWDM Applications', Application Brief p/n 5980-1454E, Agilent Technologies (2002).

[66] H.-G. Unger, 'Optische Nachrichtentechnik Teil II: Komponenten, Systeme, Messtechnik', ISBN 3-7785-0961-6, Hedelberg:Hüthig (1985).

[67] R. Ludwig, S. Diez, A. Ehrhardt, L. Küller, W. Pieper, H.G. Weber, 'A Tunable Femtosecond Modelocked Semiconductor Laser For Applications in OTDM Systems', IEICE Trans. Electron., E81-C(2), pp. 140-145 (1998).

[68] T. Tekin, M. Schlak, Ch. Schmidt, C. Schubert, 'The Influence of Gain and Phase Dynamics in the Integrated GS-SOA on the Switching Performance of the Monolithically Integrated GS-MZI', submitted to Integrated Photonics Research IPR 2004.

[69] T. Tekin, C. Schubert, J. Berger, M. Schlak, B. Maul, W. Brinker, R. Molt, H. Ehlers, M. Gravert, H.-P. Nolting, '160 Gbit/s Error-Free All-Optical Demultiplexing Using Monolithically Integrated Band Gap Shifted Mach-Zehnder Interferometer (GS-MZI)', Integrated Photonics Research (IPR), IWC4, Vancouver (2002).

[70] T. Tekin, C. Bornholdt, J. Slovak, M. Schlak, B. Sartorius, J. Kreissl, S. Bauer, C. Bobbert, W. Brinker, B. Maul, Ch. Schmidt, H. Ehlers, 'Semiconductor Based True All-Optical Synchronous Modulator for 3R Regeneration', Proc of 29th European Conference on Optical Communication 14th International Conference on Integrated Optics and Optical Fibre Communication ECOC-IOOC2003 Rimini, vol.3 pp. 794-795 (2003).

[71] G. Topchiyski, K. Petermann, S. Diez, E. Hilliger, C. Schmidt, R.. Ludwig, H.G. Weber, 'Evaluation of Switching Windows for Fast Optically-Controlled SOA Switches', Tech. Dig. Of 25th Optical Fiber Commun. ThF4, pp. 84-86 Baltimore (2000).

[72] U. Busolt , G. Bramann, H.-J. Wünsche, Chr. Schmidt, B. Sartorius, H.-P. Nolting, T. Rosin, 'Two-Wave Competition for All-Optical Signal Processing: First Experimental Verification in Ultra-Long SOAs' Proc of 29th European Conference on Optical Communication 14th International Conference on Integrated Optics and Optical Fibre Communication ECOC-IOOC2003 Rimini, pp. 1060 (2003).

[73] http://www.VPIsystems.com

[74] S. Nakamura, Y. Ueno, K. Tajima, J. Sasaki, T. Sugimoto, T. Kato, T. Shimoda, M. Itoh, H. Hatakeyama, T. Tamanuki, T. Sasaki, 'Demultiplexing of 168 Gb/s Data Pulses With Hybrid-Integrated Symmetric Mach-Zehnder All-Optical Switch', IEEE Photon. Technol. Lett., vol. 12, pp. 425-427 (2000).

[75] S. Diez, C. Schubert, R. Ludwig, H.-J. Ehrke, U. Feiste, C. Schmidt, H.G. Weber, '160 Gbit/s All-Optical Demultiplexer Using Hybrid Gain-Transparent SOA Mach-Zehnder', Electron. Lett., vol. 36, pp. 1484-1485 (2000).
[76] N.J. Doran, D. Wood, 'Nonlinear-Optical Loop Mirror' Optics Letters vol. 13, pp. 56-58 (1988).
[77] N.J. Doran, D.S. Forrester, B.K. Nayar, 'Experimental Investigation of All-Optical Switching in Fiber Loop Mirror Device', Electron. Lett. vol. 25, pp. 267-269 (1989).
[78] K. Otsuka, 'Nonlinear Antiresonant Ring Interferometer', Optics Letters vol. 8, pp. 471-473 (1983).
[79] M. Eiselt, 'Ring-Interferometer mit Halbleiterlaserverstärker: Grundlagen und Anwendungen', PhD thesis, Technische Universität Berlin, Germany (1994)
[80] B.P. Nelson, K.J. Blow, P.D. Constantine, N.J. Doran, J.K. Lucek, I.W. Marshall, K. Smith, 'All-optical Gbit/s switching using nonlinear optical loop mirror', Electron. Lett. vol.27, pp. 704-705 (1991).
[81] P.A. Andrekson, N A. Olsson, J.R. Simpson, D.J. Digiovanni, P.A. Morton, T. Tanbun-Ek, R.A. Logan, K.W. Wecht, '64 Gb/s all-Optical Demultiplexing With the Nonlinear Optical-Loop Mirror', Photon. Tech. Lett. vol. 4, pp. 644-647 (1992).
[82] S. Kawanishi, H. Takara, K. Uchiyama, M. Saruwatari, '64 to 8 Gbit/s All-Optical Demultiplexing Experiment Using New Phase Lock Loop Technique', Electron. Lett. vol. 29, pp. 231-233 (1993).
[83] K. Uchiyama, H. Takara, S. Kawanishi, T. Morioka, M. Saruwatari, T. Kitoh, '100 Gbit/s All-Optical Demultiplexing Using Nonlinear Optical Loop Mirror With Gating-Width Control', Electron. Lett. vol. 29, pp. 1870-1871 (1993).
[84] M.E. Fermann, F. Haberl, M. Hofer, H. Hochreiter, 'Nonlinear Amplifying Loop Mirror', Optics Letters vol. 15, pp. 752-754 (1990).
[85] M.J. O'Mahony, 'Semiconductor Laser Optical Amplifiers For Use In Future Fiber Systems', J. Lightwave Technol. Vol. 6, pp. 531-544, 1988.
[86] A. Yariv, P. Yeh, 'Optical Waves In Crystals', Jon Wiley &Sons Inc. (1984).
[87] T. Tekin, 'Herstellung und Charakterisierung von monolthisch integrierten MZI-Wellenlängenkonvertern' Diplomarbeit, Technische Universität Berlin, Fachbereich Elektrotechnik (1997).
[88] M. Saruwatari, K. Nawata, 'Semiconductor Laser To Single-Mode Coupler', Appl. Optics, 18, No 11 (1979).

[89] S. Diez, C. Schubert, U. Feite, R. Ludwig, J. Berger, H.G. Weber, ' 160Gb/s all-optical demultiplexing using a gain-transparent ultrad´fast-nonlinear interferometer', Techn. Dig. Of Optical Amplifiers and their Applications, OAA, pp. PD9 (2000).

[90] P. Maat, 'InP-based integrated MZI switches for optical communication', Diss. (2001).

[91] J. P. R. Lacey, F. P. Payne, 'Radiation loss from planar waveguides with random wall imperfections', IEE Proceedings, Vol. 137, Pt. J, No. 4, (1990).

[92] S.-P. Chen, J. Mähnß, H.-G. Unger, 'Scattering Loss of Optical Waveguides due to Edge-Imperfections, AEÜ Band 43, Heft 6, (1989).

[93] R. Hess, M. Caraccia-Gross, W. Vogt, E. Gamber, P.A. Besse, M. Duelk, E. Gini, H. Melchior, B. Mikkelsen, M. Vaa, K.S. Jepsen, K.E. Stubkaer, S. Bouchoule, 'All-optical demultiplexing 80 to 10 Gb/s signals with monolithic integrated high performance Mach-Zehnder interferometer', IEEE Photon. Technol. Lett., vol. 10, pp. 165-167 (1998).

[94] C. Schubert, S. Diez, J. Berger, R. Ludwig, U. Feiste, H. G. Weber, G. Toptchiyski, K. Petermann, V. Krajinovic, '160 Gb/s all-optical demultiplexing using a gain-transparent ultrafast-nonlinear interferometer (GT-UNI)', IEEE Photon. Technol. Lett., vol. 13, pp. 475-477 (2001).

[95] B. Mikkelsen, T. Durhuus, C. Jorgensen, S.L. Danielsen, R.J.S. Pedersen, K.E. Stubkjaer, 'Wavelength conversion using interferometric structures containing semiconductor laser amplifiers', Optical amplifiers and their app. OSA Tech. Dig. Series 18, pp. 238-241 (1995).

[96] N. Agrawal, E. Jahn, W. Pieper:'Integrated optics for high bitrate systems', MOC/GRIN'97 Tokyo, Japan (1997).

[97] J.P. Hall, M.Q. Kearly, A.J. Moseley and M.J. Goodwin, 'Micropackaging Technologies for optoelectronic components', ECOC 1997, Edinburgh, UK, Conf.3 Publ. No. 448 IEE, 4, pp. 101-104 (1997).

[98] A.R. Mickelson, N. Basavanhally, Y-C.Lee: 'Optoelectronic Packaging', Wiley &Sons, New York, pp. 45-58 (1997).

[99] M. Becker, R. Günther, R. Staske, R. Olschewsky, H. Gruhl and H. Richter, 'Laser micro welding and micro melting for connection of optoelectronic micro-components' in Laser in Engineering, Laser 93, W. Waidelich, Ed., Springer-Verlag, Berlin, pp. 457-460 (1994).

[100] D.S. Alles: 'Trends in Laserpackaging', Proceedings of 40th Electronic Components and Technology Conference, Las Vegas, pp. 185-192 (1990).

[101] D.S. Bargar, 'An Automated Fiber Alignment, Fixing and Hermetic Sealing System', SPIE Vol 1994 Optoelectronic Materials, Devices, Packaging and Interconnects II, pp. 12-17 (1988).

[102] T. Tekin, H. Ehlers, M. Schlak, J. Berger, C. Schubert, B. Maul, R. Ziegler, 'All-optical demultiplexing performance of monolithically integrated GS-MZI module', 1. Int. Workshop on Optical MEMS and Integrated Optics, Universität Dortmund, Germany, (2001).
[103] T. Tekin, M. Schlak, W. Brinker, J. Berger,C. Schubert, B. Maul, R. Molt, 'Ultrafast all-optical demultiplexing performance of monolithically integrated band gap shifted Mach-Zehnder interferometer', Proc. of 27th Europ. Conf. Opt. Commun. (ECOC'01), vol. 4, pp. 504-505, Amsterdam, Netherlands (2001).
[104] T. Tekin, M. Schlak, W. Brinker, J. Berger, C. Schubert, B. Maul, R. Molt, 'All-optical demultiplexing using monolithically integrated Mach-Zehnder interferometer based on band gap shifted semiconductor optical amplifier', Proc. of 10th Europ. Conf. on Integrated Optics, Postdeadline FrPD01, Paderborn, Germany (2001).
[105] T. Tekin, C. Schubert, J. Berger, M. Schlak, B. Maul, W. Brinker, R. Molt, H. Ehlers, '160 Gbit/s error-free all-optical demultiplexing using monolithically integrated band gap shifted Mach-Zehnder interferometer', 19th Congress of the International Commission for Optics, Firenze, Italy (2002).
[106] K.J. Blow, N.J. Doran, B.P. Nelson, 'Demonstration of the nonlinear fiber loop mirror as an ultrafast all-optical demultiplexer', Electron. Lett. vol. 26, pp. 962-964 (1990).
[107] S. Kawanishi, 'Ultrahigh-speed optical time-division-multiplexed transmission technology based on optical signal processing', IEEE J. of Quantum Electron. 34, 2064-2079 (1998).
[108] E. Bodtker, H.E. Bowers, 'Techniques for optical demultiplexing in hogh bit rate communication systems', Jour. of Lightwave Techn. vol.13, pp.1809-1814 (1995).
[109] E. Tangdiongga, 'Crosstalk mitigation techniques in multi-wavelength networks comprising photonic integrated circuits', PhD thesis , Eindhoven University of Technlogy, The Netherlands (2001).
[110] K. Obermann, 'All-optical wavelength conversion based on cross-gain modulation and four-wave mixing in semiconductor optical amplifiers', PhD thesis, Technische Universität Berlin, 1998.
[111] R. P. Schreieck. 'Ultrafast dynamics in InGaAsP/InP optical amplifiers and mode locked laser diodes', PhD thesis, Swiss Federal Institute of Technology Zurich, Switzerland (2001).
[112] P. Maat, 'InP-based integrated MZI switches for optical communication', PhD thesis, Technische Universiteit Delft, The Netherlands (2001).

[113] L. Occhi, 'Semiconductor optical amplifiers made of ridge waveguide bulk InGaAsP/InP: experimental characterization and numerical modelling of gain, phase, and noise', PhD thesis, Swiss Federal Institute of Technology Zurich, Switzerland (2002).
[114] Ch. Schmidt, 'Analyse und Modellierung integrierter optischer Mach-Zehnder Interferometer', Diplomarbeit, Technische Universität Berlin, Germany (2001).
[115] Y. Ueno, S. Nakamura, and K. Tajima, 'Penalty-free error-free all-optical data pulse regeneration at 84 Gb/s by using a Symmetric-Mach-Zehnder-type semiconductor regenerator', IEEE Photonics Technol. Lett., Vol. 13, No. 5, pp. 469-471 (2001).
[116] S. Nakamura, Y. Ueno, K. Tajima, J. Sasaki, T. Sugimoto, T. Kato, T. Shimoda, M. Itoh, H. Hatakeyama, T. Tamanuki, and T. Sasaki, 'Demultiplexing of 168-Gb/s data pulses with a hybrid-integrated symmetric Mach-Zehnder all-optical switch', IEEE Photonic Technol. Lett., Vol. 12, No. 4, pp. 425-427 (2000).
[117] S. Nakamura, Y. Ueno, and K. Tajima, '168-Gb/s all-optical wavelength conversion with a Symmetric-Mach-Zehnder-type switch', IEEE Photonic Technol. Lett., Vol. 13, No. 10, pp. 1091-1093 (2001).
[118] Y. Ueno, S. Nakamura, and K. Tajima, 'Ultrafast 168-GHz 1.5-ps 1-fJ symmetric- Mach-Zehnder-type all-optical semiconductor switch', Jpn. J. Appl. Phys., Vol. 39, Part 2, No. 8A, pp. L806-808 (2000).
[119] K. Tajima, S. Nakamura, Y. Ueno, J. Sasaki, T. Sugimoto, T. Kato, T. Shimoda, H. Hatakeyama, T. Tamanuki, and T. Sasaki, 'Ultrafast hybrid-integrated symmetric Mach-Zehnder all-optical switch and its 168 Gbps error-free demultiplexing operation', IEICE Trans., Electron., Vol. E-83C, No. 6, pp. 959-965 (2000).
[120] P.V. Studenkov, M.R. Gokhale, J. Wei, W. Lin, I. Glesk, P.R. Prucnal, S.R. Forrest, 'Monolithic integration of an all - optical Mach - Zehnder demultiplexer using an asymmetric twin - waveguide structure', IEEE Photonics Technology Letters, Vol. 13, No. 6, pp. 600-602 (2001).
[121] B. E. Olsson and D. J. Blumenthal, 'All-optical demultiplexing using fiber corss-phase modulation (XPM) and optical filtering', IEEE Photon. Technol. Lett., Vol. 13, pp. 875-877 (2001).
[122] J. Leuthold, F. Girardin, P.A. Besse, E. Gamper, G. Guekos, H. Melchior, 'Polarization independent optical phase conjugation with pump-signal filtering in a monolithically integrated Mach-Zehnder interferometer semiconductor optical amplifier Configuration', Photonics Technology Letters, Vol. 10., No. 11, pp. 1569-1571 (1998).
[123] J. Leuthold, E. Gamper, M. Dülk, P.A. Besse, J. Eckner, R. Hess, H. Melchior, 'Cascadable All-Optical Space Switch with High and Bal-

anced Extinction Ratios', 2nd Optoelectronic and Communications Conference (OECC'97), paper 9C3-4 (1997).
[124] J. Leuthold, P.A. Besse, E. Gamper, M. Dülk, St. Fischer, H. Melchior, 'Cascadable Dual-Order Mode All-Optical Switch with Integrated Data and Control-Signal Separators', Electronics Letters, Vol. 34, No. 16, pp. 1598-1600 (1998).
[125] J. Leuthold, J. Eckner, Ch. Holtmann, R. Hess, H. Melchior, 'All-Optical 2x2-Switches with 20 dB Extinction Ratios', IEEE J. of Quantum Electronics, Vol. 34, No. 4, pp. 622-633 (1998).
[126] J. Leuthold, P.A. Besse, E. Gamper, M. Duelk, St. Fischer, G. Guekos, H. Melchior, 'All-Optical Mach-Zehnder Interferometer Wavelength Converters and Switches with Integrated Data and Control-Signal Separation Schemes', J. of Lightwave Technology, Vol. 17, No. 6, pp. 1056-1066 (1999).
[127] S. Diez, R. Ludwig, and H. G. Weber, 'Gain-transparent SOA-switch for high-bitrate OTDM add/drop multiplexing', IEEE Photon. Technol. Lett., Vol. 11, No. 1, pp. 60–62 (1999).
[128] St. Fischer, M. Dülk, M. Bitter, M. Caraccia, E. Gamper, W. Vogt, E.Gini, H. Melchior, W. Hunziker, A. Buxens, H. N. Poulsen, and A.T. Clausen, 'Ultrafast all-optical demultiplexer based on Mach–Zehnder interferometer with integrated semiconductor optical amplifiers', Proc. 5th Optoelectronics Communications Conf. (OECC 2000), pp. 566–567 (2000).
[129] R. Schreieck, M.Kwakernaak, H. Jäckel, E. Gamper, E. Gini, W. Vogt, and H. Melchior, 'Ultrafast Switching Dynamics of Mach-Zehnder Interferometer Switches', IEEE Photon. Technol. Lett., Vol. 13, No. 6, pp.603-605 (2001).
[130] K. Uchiyama and T Morioka, 'All-optical time-division demultiplexing experiment with simultaneous output of all constituent channels from 10OGbit/s OTDM signal', Electronics Letters, Vol. 37, No. 10, pp. 642-643 (2001).
[131] G. Toptchiyski, S. Randel, K. Petermann, C. Schubert, J. Berger, H. G. Weber, „Comparison of switching windows of an all-optical 160Gbit/s demultiplexer with base data rates of 10Gbit/s and 40Gbit/s', Technical Digest of Optical Fiber Communication Conference 2001, OSA Technical Digest, Anaheim, USA, paper MB5 (2001).
[132] M. Gunkel, F. Küppers, J. Berger, U. Feiste, R. Ludwig, C. Schubert, C. Schmidt, H.G. Weber, 'Unrepeatered 40Gbit/ RZ transmission over 252km SMF using Raman amplification', Electronics Letters, Vol. 37, No. 10, pp. 646-648 (2001).

[133] H. Shi and J. Lin, 'Theoretical analysis on polarization deviation and switch window optimization in nonlinear optical loop mirror demultiplexer', Journal of Lightwave Technology, Vol. 17, No. 12, pp. 2572-2576 (1999).

[134] Y. Ueno, S. Nakamura, and K. Tajima, 'All-optical divided-clock extractor using an ultrafast all-optical symmetric-Mach-Zehnder-type semiconductor switch embedded in an optical loop', Jpn. J. Appl. Phys. Vol. 39, part 2, No. 8A, pp. L803-805 (2000).

[135] J. H. Lee, J. Y. Wang, C. C. Yang, and Y. W. Kiang, 'All-Optical Switching Behaviors in an All-Semiconductor Nonlinear Loop Device', Journal of Optical Society of America B, Vol. 18, No. 9, pp. 1334-1341 (2001).

[136] Y. Peida, Z. Yongpeng, 'All-Optical OTDM Add/Drop Multiplexing using Semiconductor Optical Amplifier based Mach-Zehnder Interferometer with improved Extinction Ratio', JOC - Journal of Optical Communications, Vol. 22, Issue 4, pp. 122-126 (2001).

[137] H. Takara, I. Shake, S. Kawanishi, Y. Yamabayashi, K. Magari, Y. Tohmori, K. Takiguchi, I. Ogawa, A. Himeno, 'Integrated optical time division multiplexer based on planar lightwave circuit', Electronics Letters, Vol. 35, No. 15, pp. 1263-1264 (2001).

[138] V. Kaman, A. J. Keating, S. Z. Zhang, J. E. Bowers, 'Simultaneous OTDM Demultiplexing and Detection using an Electroabsorption Modulator', IEEE Photonics Technology Letters, Vol. 12, No. 6, pp. 711-713 (2000).

[139] M. Heid, S. Spälter, G. Mohs, A. Färbert, W. Vogt, H. Melchior, '160-Gbit/s demultiplexing based on a monolithically integrated Mach-Zehnder interferometer', Proc. of 27th Europ. Conf. Opt. Commun. (ECOC'01), PD.B.1.8, Amsterdam, Netherlands, (2001)

[140] St. Fischer, M. Bitter, M. Caraccia, M. Dülk, E. Gamper, W. Vogt, E.Gini, H. Melchior, 'All-optical sampling with a monolithically integrated Mach-Zehnder interferometer gate', Optics Letters, Vol. 26, No. 9, pp. 626-628 (2001).

[141] E. Voges, K. Petermann, 'Optische Kommunikationstechnik: Handbuch für Wissenschaft und Industrie', Springer (2002).

[142] J.T. Verdeyen, 'Laser Electronics', Prentice-Hall Internatioanl Inc. (1989).

[143] H.Ghafouri-Shiraz, 'Fundamentals of Laser Diode Amplifiers', Wiley (1995).

[144] M.A. Summerfield, 'Telecommunications Applications of Four-Wave Mixing in Semiconductor Optical Amplifiers', PhD thesis, The University of Melbourne, Australia (1995).

9 Appendix

9.1 Sagnac Interferometer

Nonlinear interferometric structures for all-optical demultiplexing were primarily assembled as nonlinear Sagnac interferometer (SI) [15] [79]by using only an optical fiber loop or discrete semiconductor optical amplifier components incorporated within an optical fiber loop.

Nonlinear Optical Loop Mirror

The nonlinear optical loop mirror (NOLM) is a type of SI (Figure 9.1). The NOLM bases on the nonlinear propagation in a fiber, which is formed like a loop by connecting the output ports of a conventional coupler. The NOLM was proposed as an ultrafast switching device by Doran and Wood [76]. First experiments with the NOLM switch were performed in 1989 [77]. The idea of using a Kerr-like medium in a ring interferometer was firstly proposed by Otsuka in 1983 [78].
The NOLM operates with the nonlinear phase shift induced by self phase modulation (SPM). It consists of a coupler with an unequal coupling ratio to keep the nonlinear propagation effect unequal for both counter-propagating signals.

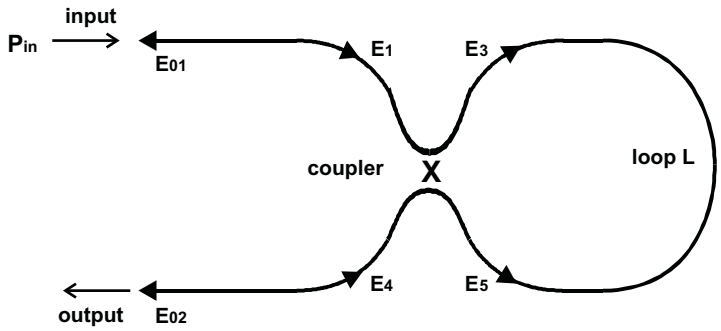

Figure 9.1 The nonlinear optical loop mirror configuration after [76].

A single optical input (P_{in}) is split into two counter-propagating fields, which return in coincidence to recombine at the coupler after passing the precisely same length of optical path. Here, the power-coupling ratio of the coupler can

be described as k : 1-k. Since the phase velocity is depending on the intensity, k is unequal to 0.5 and the nonlinear propagation effect is different for the two paths. The phase shift between two counter-propagating signals E_3 and E_4 for a loop length L under the influence of SPM can be given by the following equation [76]:

$$\Delta\varphi = \frac{2\pi L}{\lambda} n_2 \left(\left|E_3\right|^2 - \left|E_4\right|^2 \right) = \frac{2\pi L}{\lambda} n_2 (1-2k) \frac{P_{in}}{A_{eff}}, \qquad (9.1)$$

where n_2 is the nonlinear Kerr coefficient, A_{eff} the effective core area of the fiber. With every increase of the power by $l/[2(1-2k)n_2L]$ the output switches from the low power value to 100 % value [76]. The best switching ratio occurs for k closest to 0.5 [76]. However, in this case the switching energy increases correspondingly [79].
All-optical demultiplexing using the NOLM switch has been demonstrated by different research groups [80], [81], [82]. First error-free all-optical demultiplexing 100 to 6.3 Gbit/s has been demonstrated using a 6 km long fiber loop [83].
The NOLM switch based on the Kerr effect has a simple construction. This Sagnac interferometer does not require interferometric alignments and so is a stable device [76]. Ultrafast processing is possible, because the response time of the nonlinearity in silica is in the femtosecond range. However, the intensity dependent nonlinear refractive index n_2 for silica is extremely small (~ $3\ 10^{-20}$ m^2/W [76]), which means high optical power and long fiber lengths are required. For the required phase change of π, typically a power-length product of 1 Wkm is needed. By increasing the fiber length the switching power reduces, but in that case walk off between the signal and control pulses occurs, due to chromatic and/or polarization dispersions. This increases the interaction duration time, resulting in a decrease of switching speed.

Nonlinear Amplifying Loop Mirror

The nonlinear amplifying loop mirror (NALM) type of Sagnac interferometer was proposed by Fermann [84], to avoid the disadvantage of NOLM due to the large power-length product, which is needed to achieve the required phase change of π.
The NALM consists of an asymmetrically positioned fiber amplifier at one end of the fiber loop and a 3 dB coupler (Figure 9.2). In the coupler the input signal P_{in} is split in two counter propagating parts, where the power coupling ratio is k : 1-k.

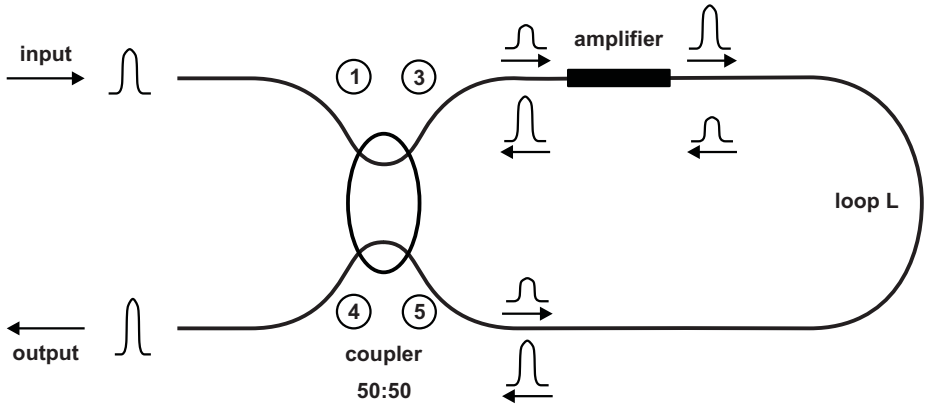

Figure 9.2 The nonlinear amplifying loop mirror configuration after [84].

The phase shift between these two counter-propagating signals can be given for a loop length L by [84]

$$\Delta\varphi = \frac{2\pi L}{\lambda} n_2 \left[(1-k)g - k\right] \frac{P_{in}}{A_{eff}}, \qquad (9.2)$$

where g is the linear amplifier gain and A_{eff} the effective core area of the fiber amplifier.
The NALM is an improvement of the conventional NOLM due to the insertion of the asymmetrically located optical fiber amplifier. Furthermore, here a conventional 3 dB coupler can be used [84]. The power-length product is smaller (0.161 Wkm [79])compared to the typical NOLM (k = 0.6, g = 1 [84]), leading to a decrease of the needed input power in a NALM (k = 0.5, g = 10) for the same fiber loop length by more than 13 dB. However, the long fibers (few kilometers) are still a disadvantage of the nonlinear amplifying loop mirror.

Loop Mirror Configuration with a Nonreciprocal Element

The usage of the combination of amplifier and attenuator, with larger Kerr coefficient positioned asymmetrically in a Sagnac interferometer, instead of the long fiber loops was proposed by O'Neill [32].
With the inclusion of the nonreciprocal amplifier/attenuator combination in the loop mirror (Figure 9.3), the counter clockwise propagating light is attenuated before being amplified and the clockwise propagating light experiences the reverse. The two signals passing the semiconductor laser amplifier (SLA) at different times generate a different average of internal intensities and therefore different carrier densities and refractive indices. This causes a

gain- and phase-change experienced by the two counter propagating signals within the gain medium to be different [85].

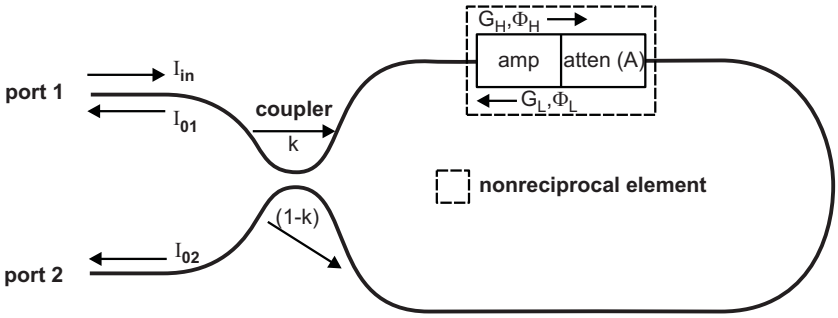

Figure 9.3 Loop mirror configuration with a nonreciprocal element after [32].

Experimentally this is done by using a traveling wave amplifier with a fiber/amplifier coupling loss difference of 3.6 dB at the amplifier input for the counter propagating pulses positioned in a 17 meters long fiber loop [32]. This removes the need to include a discrete attenuator.

9.2 Transfer Function of Mach-Zehnder Interferometer

In the Figure 9.4 the basic MZI structure is depicted. A_1 and A_2 are the input lightwaves for the basic structure. B_1, B_2 and D_1, D_2 are the output lightwaves after the couplers with coupling coefficient k_1, k_4 respectively. C_1 and C_2 represents the lightwaves at the outputs of the SOA_1 and SOA_2.

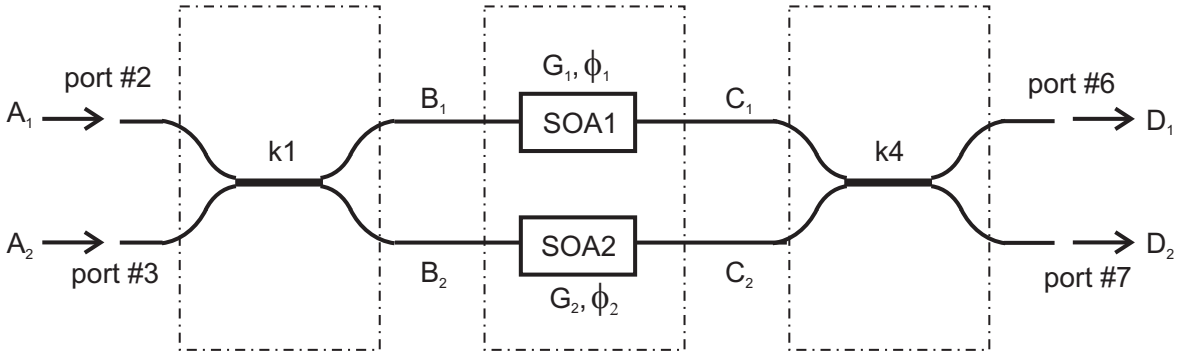

Figure 9.4 Basic structure of MZI for transfer function.

Since the relative phase shift between the interferometer arms is of interest, the coupler k_1 can be defined in matrix form as follows:

$$\begin{pmatrix} B_1 \\ B_2 \end{pmatrix} = \begin{pmatrix} \cos K_1 & i \sin K_1 \\ i \sin K_1 & \cos K_1 \end{pmatrix} \begin{pmatrix} A_1 \\ A_2 \end{pmatrix} \qquad (9.3)$$

with K_1 as a normalized coupling coefficient. Based on this equation an ideal 3 dB coupler is defined:

$$\begin{pmatrix} B_1 \\ B_2 \end{pmatrix} = \begin{pmatrix} \frac{\sqrt{2}}{2} & i\frac{\sqrt{2}}{2} \\ i\frac{\sqrt{2}}{2} & \frac{\sqrt{2}}{2} \end{pmatrix} \begin{pmatrix} A_1 \\ A_2 \end{pmatrix} \qquad (9.4)$$

An optical signal experiences in a SOA an amplification of $\sqrt{G}$ and a phase shift of Φ. By assuming the SOAs within MZI structure as a 4-port element the following transfer function can written:

$$\begin{pmatrix} C_1 \\ C_2 \end{pmatrix} = \begin{pmatrix} \sqrt{G_1}\, e^{i\Phi_1} & 0 \\ 0 & \sqrt{G_2}\, e^{i\Phi_2} \end{pmatrix} \begin{pmatrix} B_1 \\ B_2 \end{pmatrix} \qquad (9.5)$$

A_1 and A_2 are the input fields of the MZI, G_1, Φ_1 and G_2, Φ_2 are response of the SOA_1 and SOA_2, D_1 and D_2 are the output fields of the MZI, respectively (Figure 9.4). The transfer function of the basic MZI structure can be written in matrix form as follows [87]:

$$\begin{pmatrix} D_1 \\ D_2 \end{pmatrix} = (H) \begin{pmatrix} A_1 \\ A_2 \end{pmatrix} = \begin{pmatrix} H_{11} & H_{12} \\ H_{21} & H_{22} \end{pmatrix} \begin{pmatrix} A_1 \\ A_2 \end{pmatrix} \qquad (9.6)$$

with

$$\begin{aligned} H_{11} &= \cos K_1 \cos K_4 \sqrt{G_1} e^{i\Phi_1} - \sin K_1 \sin K_4 \sqrt{G_2} e^{i\Phi_2} \\ H_{12} &= i(\sin K_1 \cos K_4 \sqrt{G_1} e^{i\Phi_1} + \cos K_1 \sin K_4 \sqrt{G_2} e^{i\Phi_2}) \\ H_{21} &= i(\cos K_1 \sin K_4 \sqrt{G_1} e^{i\Phi_1} + \sin K_1 \cos K_4 \sqrt{G_2} e^{i\Phi_2}) \\ H_{22} &= -\sin K_1 \sin K_4 \sqrt{G_1} e^{i\Phi_1} + \cos K_1 \cos K_4 \sqrt{G_2} e^{i\Phi_2} \end{aligned} \qquad (9.7)$$

In terms of optical powers (P_{D1}, P_{D2}, P_{A1}, P_{A2}) and ideal 3 dB coupler the following transfer functions can be used:

$$H_{D_1} = \frac{P_{D_1}}{P_{A_1}} = \left| \left[\frac{D_1}{A_1} \right]_{A_2=0} \right|^2 = \frac{1}{4} G_1 + \frac{1}{4} G_2 - \frac{1}{2} \sqrt{G_1 G_2} \cos\Delta\Phi \qquad (9.8)$$

$$H_{D_2} = \frac{P_{D_2}}{P_{A_1}} = \left| \left[\frac{D_2}{A_1} \right]_{A_2=0} \right|^2 = \frac{1}{4} G_1 + \frac{1}{4} G_2 + \frac{1}{2} \sqrt{G_1 G_2} \cos\Delta\Phi \qquad (9.9)$$

$$\Delta\Phi = \Phi_1 - \Phi_2 \qquad (9.10)$$

9.3 Fabrication of Monolithically Integrated MZI

Within the scope of this thesis, monolithically integrated Mach-Zehnder interferometers have been fabricated using the two-inch InP substrates. The amplifier layer structure is first grown on 100-oriented sulphur doped InP substrates by using metal organic vapor phase epitaxy (MOVPE). This wafer is wet chemically etched to remove the oxide monolayers, which are created on its surface due to the exposure to laboratory atmosphere. Immediately, after this step the wafer is loaded into plasma enhanced chemical vapor phase (PECVD) system. A thin layer of 300 nm silicon nitride (SiN_x) is deposited using PECVD for selective epitaxy. Islands of photoresist pads are created using the standard photolithography process in order to define the regions for active sections. After a reactive ion etching (RIE) process of SiN_x in the passive sections the photoresist is removed. As a result of this step, SiNx-pads are created on top of the active regions. Wet chemical etching of contact and cladding layers in the passive sections was carried out with a SiN_x mask. This is followed by a dry etching step to etch the 200 nm thick InGaAsP (λ=1.55 µm) active layer and approximately 85 nm of n-InP(Si) cladding layer. After removing the damage due to the ion bombardment during dry etching with wet chemically etching the passive waveguide layers are selectively grown by MOVPE to achieve a butt-join to the active sections(Figure 9.5).

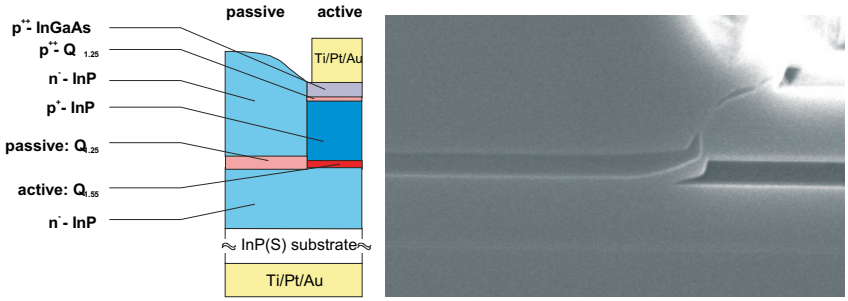

Figure 9.5 SEM-photograph of cleaved plane through butt coupling area.

The Mach-Zehnder interferometer patterns with 2 µm wide passive and 1.2 µm wide amplifier structures are then defined by photolithography. A combination of RIE and wet chemical etching processes are used for defining

the lateral dimension of SOAs, circular bends, and multi-mode interference couplers. Here, a critical wet chemical etching step has to be employed for achieving a lateral 0.5µm undercut in the SOA region required for overgrowth of blocking layers and for defining the width of the active waveguide. In the third epitaxial step the blocking layers are selectively grown around the amplifier mesas. After removing the SiN_x mask wet chemically Zn^{++} ions were indiffused into the top contact layer to increase the doping level. After an image reversal photolithography step and subsequent removal of the top oxide monolayers wet chemically the metal-contact layers are sputter deposited on the top of p-InGaAs(Zn) contact layer. Electrical isolation between SOAs is achieved by wet chemically etching of the top cladding layers grown during the final epitaxial step.

PN-Blocking: Bulk InGaAsP quaternary layers buried within InP cladding layers with band gap wavelengths of 1.55µm and 1.25µm are used as a core of the active and passive waveguides, respectively. For the integration of the active/passive sections a butt-coupling scheme is applied (Figure 9.6).
An etched mesa buried hetero structure (EMBH) with p-n-blocking layers is used for the fabrication of the SOAs. The lower part of the blocking layers also acts as a cladding layer in the passive waveguide section. In order to reduce the optical losses here arising from free-carrier absorption the p-doping level of this layer has to be kept as low as possible ($p \approx 10^{17}$ cm^{-3}).

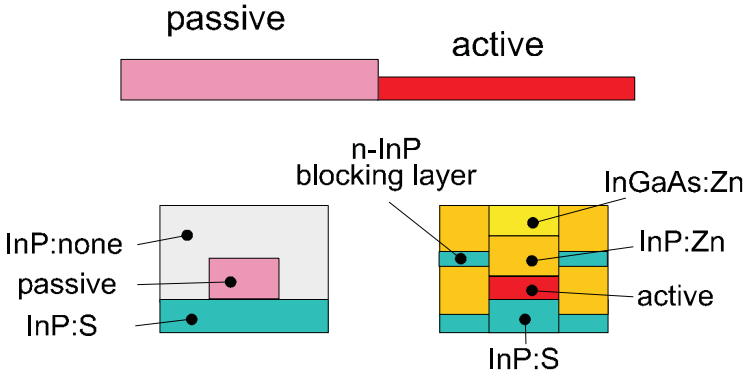

Figure 9.6 Monolithic integration scheme with active and passive waveguide cross-sections.

After defining the active and passive sections selective epitaxy is performed using a SiN_x mask to grow the p-n-blocking and cladding layers and the contact layers. All epitaxial layers (4 steps) are usually grown by low pressure ($2x10^3$Pa) MOVPE at 670°C.

Fe-Blocking: An important technological issue in fabricating integrated SOAs is the reduction of parasitic leakage currents. High currents not only increase the current required to achieve a certain gain but also give rise to additional heating which limits the maximum achievable gain. The series resistances of the amplifier path also have to be kept as low as possible in order to limit the thermal dissipation. As in an integrated MZI chip as designed in this thesis the SOA is embedded in the same layer structure as the passive waveguides, the influence of the layer characteristics on both, waveguides and amplifiers, has to be taken into account, if the layer structure is changed in any way.
A second method to confine the current to the active layer of the amplifier besides p-n-blocking is the growth of blocking layers with a sufficiently high resistant. Furthermore these layers guarantee low optical excess losses of overgrown passive waveguides due to reduced free carrier absorption. These highly resistive layers can be achieved by using Fe doping (si, semi-insulation).
Disadvantage of the growth of Fe-doped layers is the high diffusion constant of Fe in InP at the usual growth temperatures. In the case of the amplifier active regions the Fe atoms act as non-radiative recombination centers quenching very effectively the stimulated emission. Here growth at low temperatures (< 550°C) may be a way out. While in a conventional MOVPE up to now no satisfactory results could be obtained, Fe-doped layers grown in a MOMBE equipment at growth temperatures down to 450°C show high resistant, smooth surfaces, no diffusion of iron into adjacent layers.

Results: Due to the improved design and integration technology of the monolithically MZIs we achieved the following highlighted results:

- The waveguide tapers in combination with butt-fiber arrays provide less losses and larger tolerances in terms of fiber/chip coupling.
- Excess waveguide bend losses are reduced to a value smaller than 0.1 dB per bend, at detection limit.
- By using the angled butt-joint interface the internal reflections are avoided at active/passive interface.
- SOAs as FP-laser provide an emission greater than 7 mW.
- The ASE power at the output ports of the complete MZI amounts greater than 0 dBm.
- For an optical data signal the estimated transmission losses on a monolithically integrated MZI device from A to B (Figure 9.7) are as follows: 4.5 dB at each fiber/chip coupling, 0.8 dB over all waveguide

bends, 3.5 dB at each MMI coupler, 0.5 dB at each active/passive interface, 1 dB/mm over waveguides.

- Error-free all-optical demultiplexing 160 to 10 Gbit/s is performed for any arbitrary chosen

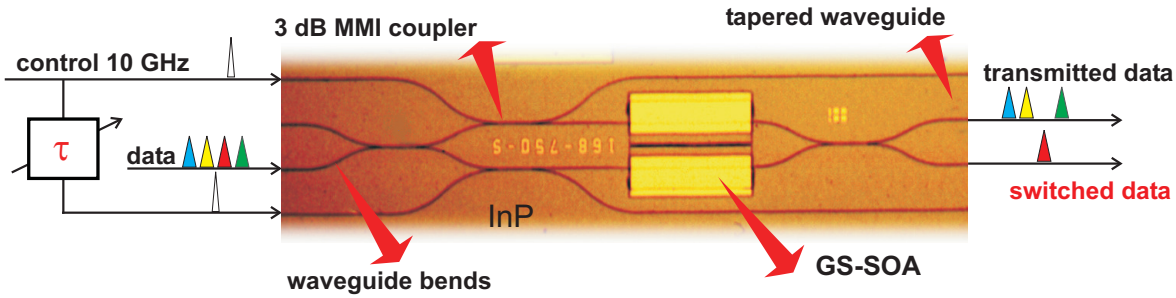

Figure 9.7 Estimated losses for a data path from A to B.

Conclusions: In the scope of this thesis, an all-optical demultiplexer by monolithic integration of semiconductor optical amplifier within both asymmetric and symmetric Mach-Zehnder interferometers have been realized. Such devices have been successfully used for all-optical demultiplexing at 40 Gbit/s (asymmetric MZI) and at 160 Gbit/s (symmetric GS-MZI), respectively. By suitable modifications of the existing design such monolithically integrated MZIs are been readily improved to achieve superior contrast ratios, reduced overall losses, and operation at much higher bit-rates. Hereto, investigations mostly focused on the symmetric MZI scheme, regarding its ultra high-speed capacity and its adjustable switching window. In terms of integration technology epitaxial overgrowth, series resistance, active/passive interface and fiber/chip coupling have been investigated, respectively. Furthermore, a new packaging scheme has been developed in co-operation with the packaging group of HHI, which enables the coupling of up to four ports at one facet.

Moreover, a new switching concept, the gain shifted switching scheme, has been developed, providing higher extinction ratio, small pattern effects, better linearity, compatibility with all-optical circuits and low polarization sensitivity.

9.4 Packaging of Monolithically Integrated MZI

The large mode field mismatch is the reason for the very low fiber chip coupling efficiency of around 10% (-10 dB) with butt ended standard monomode fibers [88]. We used lenses made at the end of the fiber by grinding the tip into a conical shape (~ 140°). With these tapered fibers a coupling efficiency of up to 50% (-3 dB) can be expected. In the case of multiple fiber tapers arranged in an array of V-grooves in a silicon base plate additional tolerances due to manufacturing of the arrays must be taken in account. The center-to-center spacing variation (± 0.5 µm) in one row for four fibers will cause an additional optical coupling loss of 1 dB for the whole array connection. The overall loss will be therefore approximately 4 dB.

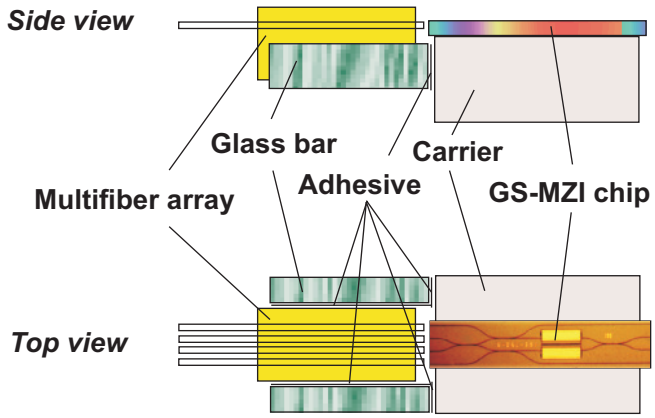

Figure 9.8 Fixation setup.

The coupling setup is sketched in the Figure 9.8. The GS-MZI is placed in the center of a miniature optical bench on a sub carrier, which is fixed by a screw. The optical fiber taper array is mounted in front of the PIC and all optical ports are adjusted to maximum coupling efficiency. To ensure the correct optical function of the fiber lenses, a distance of 10 - 15 µm from chip facet to the PIC must be kept. At both sides of the fiber taper array glass beams (5×2×1.5 mm) are placed sliding on the adhesive and held by adhesion. They are fixed to the PIC sub mount, which also acts as heat sink. After UV-curing the shrinking forces of the glue act symmetrically on the array and only a minor lateral displacement occurs. In longitudinal direction the shrinking has only small effect on the coupling efficiency because the coupling is much less sensitive to the longitudinal separation than to a transverse offset.

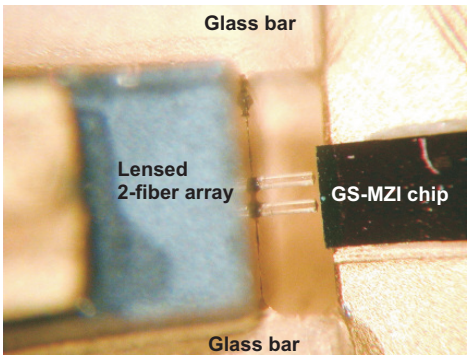

Figure 9.9 Fixed fiber array.

A photograph of the fixed fiber taper array is shown in the Figure 9.9. The PIC is located on the right hand side with the two fiber tapers in front of its output facet at a distance of 20 µm.

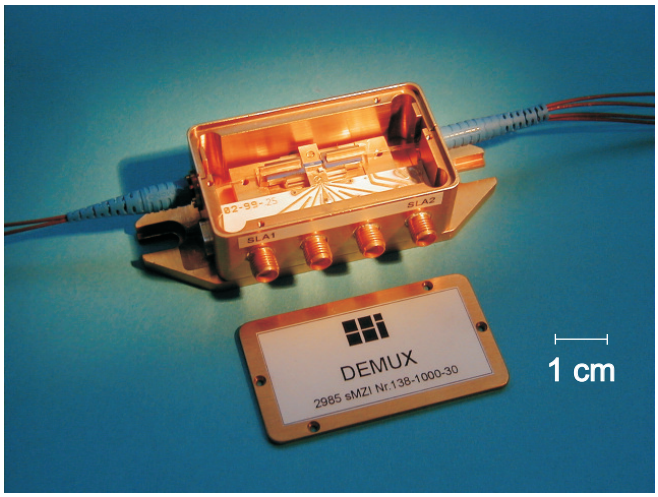

Figure 9.10 GS-MZI module.

The fibers are arranged at a pitch of 250 µm. The Figure 9.10 shows a photograph of the GS-MZI module, with a pair of optical fiber arrays and with the chip located on a carrier on top of a miniature optical bench. The assembly is mounted in a case with an electrical plug for the Peltier coolers and SMA connectors. The GS-MZI was fixed to a heat sink by using a stress-free mounting technique. The thermal expansion coefficient of the InP substrate is $\alpha_{InP}=4.5\times10^{-6}/°C$ and that of the heat sink (brass) is $\alpha_{br}=15.8\times10^{-6}/°C$. With the length of chip and heat sink of 5 mm and a temperature difference of $\Delta T=2°C$ between them we obtain a difference in length variation of only $\Delta L_{br} - \Delta L_{InP} = 0.11$ µm. Nevertheless the mounting of chip and heat sink needs a low Young's modulus adhesive. This is a special heat conducting glue, which also connects the PIC to electrical ground. A thermal sensor (NTC) for monitoring the chip temperature was embedded on the chip carrier nearby the PIC.

The bench is located on top of two Peltier coolers with 4.4 W (at 20°C) heat pump capacity for the thermal stabilization of the PIC. The case made of brass was designed to work as a heat sink for the device. For environmental temperatures higher than 40°C the module has to be fixed on an additional heat spreader. The Peltier currents and the temperature sensor connections are fed via a multiple connector to the device. The SOA bias currents are connected via SMA connectors and a thick film circuit. The PIC carrier is fixed by a screw so that it can be removed from the module quickly and exchanged for other chip dimensions. The tapered fiber array is a commercially available with a fiber tip radius of less than 10 µm. After finishing the electromechanical packaging, the chip and the fiber arrays were adjusted.

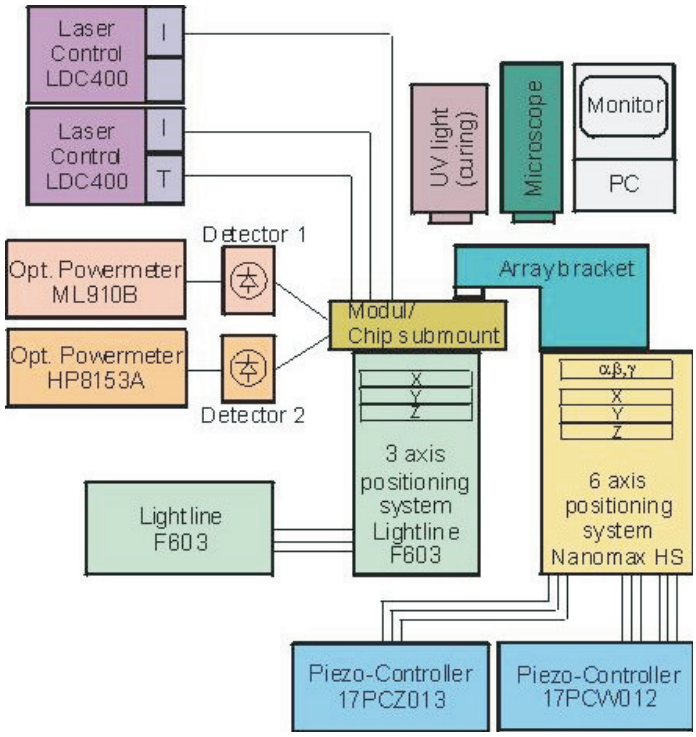

Figure 9.11 Coupling setup.

For chip-fiber coupling the module with the chip sub mount was fixed (Figure 9.11) onto a three axes stage (x, y, z). The fiber array was also fixed on a stage with three linear and three angular adjustments. The prealignment was made by manual adjusting the fiber array in a line with the waveguides of the GS-MZI using a microscope. Two IR detectors were used for optimal quantitative output survey of the alignment process. Finally the glass beams were placed at the sides of the array and fixed with an UV-curable adhesive according to the principle mentioned above. After hardening, the opposite chip interface was aligned and connected in the same way as described before.

We designed and fabricated GS-MZI modules for double-sided fiber-chip coupling. The fixation of the fiber array chip coupling was performed by a new setup with low overall connection loss. The modules have been tested in a reliability stress program. The package shows good temperature stability and is well suited for production of modules with waveguided PICs that have multiple optical ports. We showed experimentally the first ultrafast all-optical demultiplexing performance of a GS-MZI module for 80 Gbit/s and 160 Gbit/s PRBS data streams, respectively. We have demonstrated the usability of the packaged monolithically integrated gain shifted Mach-Zehnder interferometer as an ultrafast all-optical demultiplexer.

9.5 List of MZI Devices

MZI#1	2014_y11 [87]; gain maximum 1550 nm
MZI#2	3161_141; gain maximum 1550 nm
MZI#4	2725_99_1250_300; gain maximum 1500 nm
MZI#5	2985-140-750-45; gain maximum 1550 nm
MZI#6	3104-102-1000-30; gain maximum 1530 nm
MZI#7	3104-54-1000-0; gain maximum 1530 nm
MZI#10	3161 141-100-45; gain maximum 1500 nm
MZI#15	3851uLU1wsp03; gain maximum 1550 nm

10 List of Figures

11 List of Tables

12 List of Abbreviations and Symbols

3R	re-amplification, re-timing, re-shaping
AM	amplitude modulation
AR	anti reflection
ASE	amplified spontaneous emission
ATT	attenuator
BER	bit error-rate
BH	buried hetero
C	control signal
cw	continuous wave
D	data signal
DEMUX	demultiplexer
DSF	dispersion shifted single mode fiber
DUT	device under test
EAM	electro-absorption modulator
ECL	external cavity laser
EDFA	erbium doped fiber amplifier
FWHM	full width at half of maximum
FWM	four wave mixing
GS	gain shifted or band gap shifted
GT	gain transparent
ISO	isolator
MLL	mode locked laser
MLLD	mode locked laser diode
MMI	multi-mode interference
MOD	modulator
MOVPE	metalorganic vapor phase epitaxy
MQW	multi quantum well
MUX	multiplexer
MZI	Mach-Zehnder interferometer
NALM	Nonlinear amplifying loop mirror
NOLM	Nonlinear optical loop mirror
O/E	optical/electrical
OSA	optical spectrum analyzer
OTDM	optical time division multiplexing
pc	polarization controller

PIC	photonic integrated circuit
PM	phase modulation
PMF	polarization maintaining fiber
PRBS	pseudo-random bit sequence
QCSE	quantum confined Stark effect
RW	ridge waveguide
SA	saturable absorber
SDH	synchronous digital hierarchy
SI	Sagnac interferometer
SLA	semiconductor laser amplifier
SLALOM	Semiconductor laser amplifier in a loop mirror
SONET	synchronous optical network
SPM	self-phase modulation
TDMA LAN	time division multiple access local area network
TE	transverse electrical
TM	transverse magnetical
TOAD	Terahertz optical asymmetric demultiplexer
TW-LDA	traveling wave laser diode amplifiers
UNI	ultrafast nonlinear interferometer
WDM	wavelength division multiplexing
XGM	cross gain modulation
XPM	cross phase modulation

λ	wavelength
π	number
α	linewidth enhancement factor
$\Delta\varphi$	relative phase shift
λ_0	free space wavelength
$\Delta G_{TE/TM}$	gain difference between TE and TM
ΔL	relative length
Γ_{TE}	confinement factor for TE
Γ_{TM}	confinement factor for TM
2a	loss coefficient
A_{eff}	effective core area
d	thickness
d_{AR}	thickness of AR-coating
E	energy
G	linear gain
G_{FP}	Fabry Perot gain
G_S	single pass gain
g_{TE}	material gain for TE

G_{TE}	gain for TE
g_{TM}	material gain for TM
G_{TM}	gain got TE
I	current
K	bar coupling coefficient of the optical coupler
k_1, k_2, k_3, k_4	MMI coupler 1, 2, 3, 4
L	length, cavity
L_π	beat length of MMI
L_{MMI}	length of MMI
m	integer
N	natural number
n_0, n_1, n_2, n_3	refractive index
n_2	nonlinear Kerr coefficent
n_{AR}	refractive index of AR-coating
n_{eff}	effective refractive index
p	integer
P_{ASE}	ASE power
P_{in}	optical input power
P_{IN}	optical input power
P_{Loss}	optical losses
P_{Mode}	launched optical power
P_{OUT}	optical output power
q	integer
R_1, R_2	power reflection factor
R_{av}	average reflectance
R_{Bend}	bending radius
V	voltage
w	width
w_{MMI}	width of MMI
B	propagation constant
$\Delta\lambda_r$	distance between mode maximum
θ	angle
θ_{out}	output angle
λ_{cw}	wavelength of cw signal
λ_m	wavelengths of modes
ω_d	frequency of data signal
ω_{FWM}	frequency of four wave mixing product
ω_p	frequency of pump signal

13 Publications and Talks

T. Tekin, M. Schlak, Ch. Schmidt, C. Schubert, 'The Influence of Gain and Phase Dynamics in the Integrated GS-SOA on the Switching Performance of the Monolithically Integrated GS-MZI', accepted Integrated Photonics Research (IPR), IWC4, San Francisco, California, 2004.
T. Tekin, C. Bornholdt, J. Slovak, M. Schlak, B. Sartorius, J. Kreissl, S. Bauer, C. Bobbert, W. Brinker, B. Maul, Ch. Schmidt, H. Ehlers, 'Semiconductor Based True All-Optical Synchronous Modulator for 3R Regeneration', Proc. of 29th Europ. Conf. Opt. Commun. (ECOC2003), vol. 3, pp. 794-795, Rimini, Italy, (2003).
T. Tekin, C. Schubert, J. Berger, M. Schlak, B. Maul, W. Brinker, R. Molt, H. Ehlers, '160 Gbit/s error-free all-optical demultiplexing using monolithically integrated band gap shifted Mach-Zehnder interferometer', in ICO XIX: Optics for the Quality of Life, A. Consortini and G.C. Righini, Editors, Proc. SPIE 4829, pp. 605-606 (2002).
T. Tekin, C. Schubert, J. Berger, M. Schlak, B. Maul, W. Brinker, R. Molt, H. Ehlers, M. Gravert, H.-P. Nolting, '160 Gbit/s error-free all-optical demultiplexing using monolithically integrated band gap shifted Mach-Zehnder interferometer (GS-MZI)', Integrated Photonics Research (IPR), IWC4, Vancouver, Canada, (2002).
T. Tekin, M. Schlak, W. Brinker, J. Berger, C. Schubert, B. Maul, R. Molt, 'Ultrafast all-optical demultiplexing performance of monolithically integrated band gap shifted Mach-Zehnder interferometer', Proc. of 27th Europ. Conf. Opt. Commun. (ECOC'01), vol. 4, pp. 504-505, Amsterdam, Netherlands, (2001).
T. Tekin, H. Ehlers, M. Schlak, J. Berger, C. Schubert, B. Maul, R. Ziegler, 'All-optical demultiplexing performance of monolithically integrated GS-MZI module', 1. Int. Workshop on Optical MEMS and Integrated Optics, Universität Dortmund, Germany, (2001).
T. Tekin, M. Schlak, W. Brinker, J. Berger, C. Schubert, B. Maul, R. Molt, 'All-optical demultiplexing using monolithically integrated Mach-zehnder interferometer based on band gap shifted semiconductor optical amplifier', Proc. of 10th Europ. Conf. on Integrated Optics, Postdeadline FrPD01, Paderborn, Germany, (2001).
T. Tekin, M. Schlak, W. Brinker, B. Maul, R. Molt, 'Monolithically integrated MZI comprising band gap shifted SOAs: a new switching scheme for

generic all-optical signal processing', Proc. of 26th Europ. Conf. Opt. Commun. (ECOC'2000), vol. 3, pp. 123-124, Munich, Germany, (2000).
T. Tekin, M. Schlak, W. Brinker, B. Maul, R. Molt, 'Band Gap Shifted SOA Based Monolithically Integrated MZI: New Switching Scheme for Ultrahigh Speed All-optical Signal Processing', European Semiconductor Laser Workshop, Berlin, Germany, (2000).
T. Tekin, M. Schlak, W. Brinker, B. Maul, R. Molt, 'Monolithically integrated MZI comprising band gap shifted SOAs: a new switching scheme for generic all-optical signal processing', COST 266/267 Workshop 'Optical Signal Processing in Photonic Networks', Berlin, Germany (2000).
T. Tekin, 'Herstellung und Charakterisierung von monolithisch integrierten MZI-Wellenlängenkonvertern' Diplom-Thesis Technische Universität Berlin Fachbereich Elektrotechnik, Berlin, Germany, (1997).

14 Patents

Optical Differentiator
T. Tekin, B. Sartorius, M. Schlak, A. Shen, J.-G. Provost, F. Devaux. (FR2797331) (EP1145446) (WO0110045)

Optical converter of ASK NRZ format signal to RZ format signal
T. Tekin, M. Schlak, A. Shen, F. Devaux.
(FR2809497) (EP1158352) (US2002018612)

15 Acknowledgements

This work was performed at Fraunhofer Institute for Telecommunications Heinrich-Hertz-Institut in the group of Dipl.-Phys. M. Schlak.
I thank my project leader Dipl.-Phys. M. Schlak and project members Dipl.-Phys. W. Brinker, Mr. B. Maul, Dipl.-Ing. Ch. Schmidt for their valuable support, helpful discussions and excellent teamwork which have enabled the realization of this thesis.
I thank my advisor Prof. Dr. K. Petermann, for granting me the opportunity to work on the topic of this thesis, for his valuable discussions and for inviting me regularly to present my intermediate results in 'Optical Fiber Communication Seminar' held in his department.
I thank Prof. Dr. H.-G. Weber, for his willingness to supervise this thesis, for his valuable support and for allowing perform the system experiments in OTDM transmission test bed.
I thank Dr. H.-P. Nolting the head of 'Optical Signal Processing Department' for supporting my thesis in his department.
This work will not have been possible without the help and knowledge of my colleagues at Heinrich-Hertz-Institut and their willingness and openness for discussions, especially Dr. C. Schubert, Dr. C.M. Weinert, Dr. B. Sartorius, Dipl.-Phys. R. Molt, Dipl.-Ing. D. Franke, Dipl.-Ing. W. Fürst, Dipl.-Ing. R. Löffler, Dipl.-Ing. H. Ehlers, Dipl.-Ing. M. Gravert, Dipl.-Ing. H.-J. Ehrke, Dr. R. Ludwig, Dipl.-Ing. L. Küller, Dr. U. Feiste, Dr. S. Diez, Dr. J. Berger, Dr. C. Schmidt-Langhorst, Dr. E. Hilliger, Dipl.-Ing. C. Bornholdt, Dipl.-Ing. J. Slovak, Dipl.-Ing. A. Suna, Mr. C. Voigt, Mr. G. Devendra, Dipl.-Ing. V. Marembert, Dr. H. Heidrich, Dr. R. Kaiser, Dipl.-Phys. K. Janiak, Dipl.-Ing. M. Hamacher, Dipl.-Ing. P. Albrecht, Ms. I. Tiedke, Dipl.-Ing. R. Steingrüber, Ms. A. Sigmund, Dipl.-Ing. R. Ziegler, Dipl.-Ing. G. Sahin, Ms. G. Wache, Ms. G. Schmidt and Ms. A. Kroll.
I thank my colleagues at Alcatel Dr. F. Devaux, Dr. M. Renaud, Dr. C. Janz, Dr. A. Shen, Dr. O. Leclerc, Dr. P. Brindel, Dr. B. Lavigne, Dr. D. Chiaroni, Dr. J.Y. Emery, Dr. B. Dagens for fruitful discussions.
I would like to take this opportunity to thank my mother and brother who always believed in me and give tremendous motivation.
This work would not have been fulfilled without the patient, support and motivation of my beloved wife Ayca and our daughter Ada.

16 Curriculum Vitae

Name: Tolga Tekin
Date of birth: 15.05.1968
Place of birth: Istanbul, Türkiye
Email: Tolga.Tekin@alumni.TU-Berlin.de

Education:

Technische Universität Berlin, Germany
Diplom-Ingenieur (Dipl.-Ing.) in Electrical Engineering, November 1997.

Istanbul Teknik Üniversitesi, Türkiye
B.Sc. in Electronics and Communications Engineering, 1992.

Istanbul Erkek Lisesi, Türkiye
Gymnasium, 1986.

Fatih Gazi Ilkokulu, Istanbul, Türkiye
Primer school, 1979.

Experience:

Research Scientist, Deputy Project Manager
Fraunhofer Institut für Nachrichtentechnik, Heinrich-Hertz-Institut (HHI)
Optical Signal Processing Dept.
(November 1997 - present).

Research Assistant
Fraunhofer Institute für Nachrichtentechnik, Heinrich-Hertz-Institut (HHI)
Optical Signal Processing Dept.
(March 1995 - October 1997).